Normalization of Roughness Noise on the Near-Field Wall Pressure Spectrum

William Nathan Alexander

William J. Devenport
Stewart Glegg
Roger L. Simpson

June 5, 2009
Blacksburg, Virginia

Normalization of Roughness Noise on the Near-Field Wall Pressure Spectrum

William Nathan Alexander

ABSTRACT

Roughness noise can be a significant contributor of sound in low Mach number, high Reynolds number flows. Only a small amount of experimental research has been conducted to analyze roughness noise because of its often low energy levels that are hard to isolate even in a laboratory setting. This study details efforts to scale the roughness noise while independently varying roughness size and edge velocity. Measurements were taken in the Virginia Tech Anechoic Wall Jet Facility for stochastic rough surfaces varying from hydrodynamically smooth to fully rough as well as deterministic rough surfaces including 1mm and 3mm hemispheres and a 2D wavy wall. Inner and outer variable normalizations were applied to recorded far field data in an attempt to find specific driving variables of the roughness noise. Also, a newly formulated derivation that attempts to scale the far field sound from a single point wall pressure measurement was used to collapse the far field noise. From the results, the inner and outer variable scalings were unable to collapse the noise generated by all velocities and roughness sizes. The changing spectral shapes of noise generated by rough surfaces with significantly varying wavenumber spectra make it impossible to scale the produced noise using the proposed inner and outer variable scalings. They use only one a single scaling value for the entire frequency range of each spectrum. The analyzed wall pressure normalization, which is inherently frequency dependent, produces a tight collapse within the uncertainty of the measurements for all rough surfaces studied except the larger hemispherical roughness which had individual elements that dominated the surrounding region of the wall pressure microphone. This indicates that the roughness generated noise is directly proportional to the wall pressure spectrum. The collapsed data displayed a slope of ω^2, the expected dipole efficiency factor. This is the clearest confirmation to date that the roughness noise source is of a dipole nature.

Acknowledgements

I would like to thank my family and wonderful girlfriend for their support of my educational pursuits. They were a constant source of strength during stressful times and put up with a lot of complaining. They all had a part in keeping me sane and even helped in proofreading, as painful as I know that was.

I owe a huge thanks to my advisor Dr. William Devenport for his guidance. I have learned a great deal as one of his students and I am honored to be able to continue my research under his sponsorship. He has a remarkable sense of optimism that keeps goals in sight and creates an outstanding research environment.

I would like to thank Dr. Roger Simpson and Dr. Stewart Glegg for providing insight and advice during my studies. It has been a pleasure to work with them, and I look forward to continuing our research together in the future.

I would also like to thank all of my coworkers in Lab 7, especially Dr. Aurelien Borgoltz, Matt Rasnick, Dr. Ben Smith, and Ryan Catlett. They have helped me through the entire course of my research. They assisted me with both measurements and writing, but most importantly, they have been a great group of friends.

Again, I say thank you to all,

Nathan Alexander

Contents

Nomenclature

Roman

c_∞	Speed of sound
C_f	Skin friction coefficient
h	Roughness height
h^+	Roughness Reynolds number
k_o	Acoustic wavenumber
k_w	Wavenumber of rough surface
l_e	Correlation length
Re_δ	Reynolds number based on boundary layer thickness
u_τ	Friction velocity
U	Velocity
U_e	Edge velocity, maximum boundary layer velocity
U_o	Nozzle exit velocity
$\boldsymbol{x}$	Vector observer position
x	Streamwise distance from nozzle exit
y	Normal distance from wall jet surface
z	Spanwise distance from centerline of plate

Greek

$\Gamma(\kappa_1, \kappa_3, k_o)$	Wavenumber filter function
δ	Boundary layer thickness
δ^*	Displacement thickness
θ	Momentum thickness
ν	Kinematic viscosity
ρ	Density
Σ	Planar area of surface roughness
$\Phi_{pp}(\boldsymbol{x}, \omega)$	Power spectral density of radiate far field noise
$\Phi_{PP}(\omega)$	Power spectral density of surface pressure
ω	Angular frequency

List of Figures

List of Tables

Chapter 1 Introduction

1.1 Motivation

Roughness noise is a relatively little understood phenomenon that is a consequence of the interaction of roughness elements with an incoming flow field. The exact source of the noise is debated and supported by theories including diffraction mechanisms and drag dipoles. Only a small amount of experimental research has been conducted to analyze roughness noise because of its often low energy levels that are hard to isolate even in a laboratory setting. The typical sound power levels associated with roughness noise are well below those that can be generated by standard edge noise or jet noise, but for craft with particularly small edge to surface area ratios, such as submarines, roughness noise could become a significant contributor to the overall generated noise. This report investigates the source and manner in which roughness noise is transmitted into the far field using the Virginia Tech Anechoic Wall Jet Facility. This facility was built in 2005 specifically for the study of roughness noise and its acoustic and aerodynamic characteristics have been well documented in many recent publications (Grissom *et al.* 2006, Grissom *et al.* 2007).

1.2 Experimental Review

There have been few experiments to measure and define the source of roughness noise. For the experiments that have been conducted, several different methods were used yielding various conclusions. A review of these experiments will help define the developed theories and provide insight regarding current roughness noise research. One of the first experiments to measure roughness noise was conducted by Skudrzyk & Haddle (1960). They tested a spinning cylinder with a smooth surface and 180 grit and 60 grit sandpaper roughness in an acoustic water tank and measured radiated pressure fluctuations using two hydrophones flush mounted on the inside walls of the tank, one 2.5 inches in diameter and the other 5 inches in diameter. A rotating cylinder was used because of its large boundary layer thickness, somewhat like an infinite plate flow, resulting in a quieter flow at high frequency where roughness noise typically would appear. They found that roughness heights smaller than the laminar sublayer of the boundary layer produced no noise. They concluded this was due to the absence of any interaction between the hydrodynamically smooth surface and the boundary layer flow above it. They also discovered that the smaller roughness, 180 grit, produced more noise at higher frequency than the larger roughness, 60 grit, at low speed. When the free stream velocity was adjusted radiated power levels varied as velocity raised to the power 6, 10.3, and 12 for the smooth, 180 grit, and 60 grit cases, respectively. It is known from Curle (1955) and Lighthill (1952) that the sound power level will vary as velocity to the 8th for acoustic quadrupole sources and velocity to the 6th for dipoles.

Chanaud (1969) continued with rough surface sound measurements in 1969 using a roughened spinning disk in an acoustically treated environment. He found that the sound produced by flow over a rough surface emanated from the roughness element locations and that the sources produced primarily dipole characteristics. The roughness noise was most prominent for frequencies above 3150Hz. Chanaud did have some problems associated with his experimental configuration. The spinning disk produced flow over its periphery creating a pressure dipole between the two faces of the disk resulting in edge noise.

Cole (1980) used the David W. Taylor Naval Ship Research and Development Center's Anechoic Flow Facility to measure radiated sound and wall pressures from smooth and rough wall configurations. This experiment was one of the first to take place in a more conventional fully turbulent boundary layer. The resultant far field roughness noise was 2-3dB higher than the smooth wall data for 80 and 40 grit 1.68x1.98m rough patches at 24-46.5m/s. Cole applied both dipole and quadrupole scaling laws derived from Lighthill (1952) and Curle (1955) to his far field data and found that either assumption produced the same level of collapse suggesting that the noise source could be an admixture of the two source types. Cole could provide no definitive answer to the degree either source type played a role.

In 1983, Hersh used a pipe flow with varying roughness heights along the inside walls to study roughness noise at exit speeds ranging from 0-120 m/s. For part of his experiment, a single condenser microphone was placed 1.3m downstream of the pipe exit on the pipe's centerline. He found that the smooth pipe configuration produced noise consistent with quadrupole dominant jet noise that varies as velocity to the 8th and that the roughened pipe produced a dipole source noise with a 6th power velocity variation . Hersh found that as the roughness size was increased the sound intensity also increased and that the peak sound generation occurred at lower frequencies. During his study, Hersh took care to show that a lip dipole produced at the pipe exit would produce noise levels below that created by the jet noise and that his roughness noise levels were well above this. Hersh tried to scale his data with some success as a dipole using friction velocity and roughness height as his parameters (Hersh, 1983).

Employing Hersh's data for comparison, Howe (1984) published an article that attributes increases in far field sound produced by rough wall flows to a scattering effect of turbulence Reynolds stresses interacting with the surface irregularities. One result of his theory is shown in Equation 1.1.

$$\Phi_{pp}(\omega) = \frac{A k_o^2 \cos^2\theta \, P_R(k,\omega)}{|x|^2} \qquad \text{Eq. 1.1}$$

$\Phi(\omega)$ is the radiated far field noise, A is the roughness area, k_o is the acoustic wavenumber, θ is the observer angle, $\mathbf{x}$ is the observer position and $P_R(\mathbf{k},\omega)$ is the diffracted contribution of the rough wall pressure spectrum. Howe used a theoretical model of flow over a surface of hemispherical bosses that assumed there were no significant Reynolds stress fluctuations below the tops of the roughness elements. This allowed him to ignore interstitial wake flows around roughness elements but limited his theory to roughness heights that did not exceed the "buffer zone". He found that roughness noise increases with the 6th power of velocity and that his estimated spectral shapes are consistent with Hersh's data. Howe could not compare absolute levels in this study due to unknown variables in Hersh's experiment affecting the refraction of sound. Howe's theory also introduces a surface roughness density term in the definition of $P_R(\mathbf{k},\omega)$ that defines the spectral peak of the roughness noise. Howe predicts $P_R(\mathbf{k},\omega)$ is $O\{\sigma^2(kR)^2\}$ compared to the smooth wall pressure spectrum where σ is the roughness density, k is the magnitude of the surface wavenumber vector, and R is the radius of the hemispherical elements equivalent to a roughness height.

Howe updated his theory to include viscous wall stress effects in the wall pressure spectrum. His new theory estimated turbulent pressure diffraction by hydrodynamically smooth surfaces (Howe 1986). By including the viscous effects, Howe found that his theory only predicted a 2-3dB increase in noise levels from his previous theory presented in Howe (1984). In 1988, Howe presented an updated version of his diffraction theory incorporating Chase's (1987) smooth wall pressure model. Howe models the rough wall pressure spectrum by separating the spectra into a combination of Chase's model and an additional term due to the rough wall scattering mechanism. This model shows significant increases in wall pressure

levels in the acoustic region for rough walls as compared to the smooth wall spectra. Howe again compared his new model to Hersh's data adjusting for the difference in absolute levels. The spectral shape of Howe's prediction deviated from Hersh's measurement by up to 4dB (Howe 1988). Howe's advancements in estimating far field roughness noise outlined the importance of understanding rough wall pressure spectra.

Farabee & Geib (1991) used a linear array of six microphones flush mounted downstream of a variable rough or smooth section of plate to dissect the individual components of the wall pressure spectrum. The linear array created a wavenumber filter that allowed them to isolate the convective, subconvective, and sonic elements of the wall pressure spectra. They acquired data downstream of a smooth plate and 2m long rough patches that were hydrodynamically smooth, transitionally rough, or fully rough at speeds ranging from 9.1m/s to 48.8m/s. They found that the rough surfaces produced increases in convective pressures that coincide with increases in turbulence Reynolds stresses and that the increases in the acoustic region were much greater than the magnitude of the increases in the convective region. The increases in the acoustic region were found to scale best as a dipole using a mixed set of inner and outer variables for the magnitude including friction velocity, displacement thickness, and edge velocity. Outer variables such as displacement thickness and edge velocity were used to scale the frequency.

Liu *et al*. (2007) attempted to verify Howe's (1998) empirical model while comparing several different numerically integrated rough wall pressure spectra. They used smooth wall spectral theories including Corcos (1964), Efimtsov (1982), Smol'yakov & Tkachenko (1991), and Chase (1980, 1987) with enhanced skin friction velocities and boundary layer thicknesses to adjust for the presence of roughness. Liu *et al*. (2007) measured radiated sound from two 0.64x0.64m flat plates roughened with 3mm or 4mm hemispherical beads in an acoustically treated open jet wind tunnel using the cross spectra from four condenser microphones in a 0.16m square formation and a 48 microphone phased array. Results show that using the Smol'yakov & Tkachenko (1991) wave-number-frequency spectrum model to predict the roughness noise provided the closest fit to the measured far field roughness noise at high frequencies. However, all of the models overpredicted the magnitude of the spectral peak and decayed too slowly with frequency. The location of the spectral peak was well predicted by all of the methods which displayed only minor peak variations. The phased array results indicate that the majority of sound was produced at the leading edge of the roughness fetch where the roughness elements were closest to the turbulent structures of the relatively thin boundary layer. Using their numerically integrated spectrum, they determined that roughness height has a more significant impact on the far field OASPL, overall sound pressure level, then the roughness density term in Howe's (1998) theory.

Liu *et al*. (2008) continued their earlier phased array measurements of roughness noise and developed a method of data comparison for their measured source field, which through the beamforming algorithms assumes monopole sources, with a theoretically calculated field of dipole sources. The predictive model developed by Liu *et al*. (2007) was used to estimate the sound levels. The resultant theoretical and measured source maps showed significant similarity verifying the dipole nature of the sources. Still, the streamwise decay of the simulation was underestimated and the source amplitude was overpredicted by ~3dB at 2kHz.

Glegg *et al*. (2007) theoretically analyzed the sound produced by the scattering effect of wall pressure fluctuations for roughness heights no larger than the viscous sublayer and shear stress fluctuations due to larger roughness that penetrate into the log region. He concludes that Howe (1984) was correct in assuming that the noise generated by scattering dominated any noise generated by the shear

stress dipoles for roughness elements that extend into the log region. Glegg introduced a new scaling law that uses the correlation length scale of the roughness to scale the peak spectral frequency and the roughness height squared to scale the amplitude of the roughness noise. This differs from previous scaling because it employs inner and outer boundary layer variables along with two roughness characteristics.

Based on previous studies failures and successes, the Virginia Tech Anechoic Wall Jet Facility was designed and built in 2005 for the specific purpose of measuring roughness noise. The wall jet, used in the present work and described in detail in Chapter 2, provides a suitable environment for aeroacoustic measurements because microphones can be placed outside of the flow and edge noises can be reduced by making the wall sufficiently large. Several studies have been conducted in this facility including Grissom *et al.* (2006), Grissom *et al.* (2007), and Grissom (2007). Grissom (2007) made measurements in the Virginia Tech Anechoic Wall Jet Facility for 11 different rough surfaces with heights ranging from 0.068 to 0.118mm and velocities at the start of the roughness ranging from 7-22m/s. He applied scaling laws suggested by Howe (1988), Cole (1980), Glegg *et al.* (2007), and Farabee and Geib (1991) that included dipole and quadrupole scalings incorporating inner and outer variables. Each scaling produced limited success. The dipole models performed best at high frequencies with similar results regardless of the variable set used, while the quadrupole models scaled the data best when using outer variables. Grissom also recorded significant increases in far field sound for hydrodynamically smooth surfaces which is further evidence of a scattering mechanism as proposed by Howe (1984). Grissom (2007) performed directivity measurements with a single microphone placed upstream of a roughness fetch. The microphone was traversed along a circular path in the vertical plane with relative source-microphone angles varying from 45° to 85° off of horizontal. These measurements showed an 8dB reduction at the steepest angle suggesting the source might radiate most effectively in the streamwise direction but no measurements were taken perpendicular to the flow direction to examine the presence of a spanwise aligned dipole. Far field spectral levels increased with roughness size and velocity, consistent with previous studies, but the wave number spectra of the roughness surface was also found to define the shape of the resultant radiated sound field. Measurements were also taken over a near-sinusoidal surface with a 0.118mm ridge height aligned perpendicular to the flow. This rough surface's spatial wavenumbers are located in a relatively narrow band compared to the more often used stochastic roughness. The far field sound produced was more peaked than the previously studied stochastic surfaces. Grissom (2007) concluded the scattered sound was significantly impacted by the shape of the surface.

Smith (2008) continued measurements in the Virginia Tech Anechoic Wall Jet Facility for smooth and rough wall flows documenting both the boundary layer characteristics and wall pressure. He examined the boundary layer of rough surfaces varying from hydrodynamically smooth to fully rough and found increases in displacement and momentum thickness with increasing roughness size. He also found that the largest increases in wall pressure spectra due to the enhanced surface roughness occurred in the overlap region and not at the highest measured frequencies. Spectra below 400Hz converged suggesting that these pressure fluctuations in lower frequencies were dominated by turbulent structures far from the wall. Smith (2008) examined both inner and outer variable scalings for the turbulent wall pressure spectra and that of Blake (1970) and Aupperle & Lambert (1970). No scalings were found that could collapse the wall pressure spectra for all studied rough surfaces.

Yang and Wang (2008) presented LES simulations of one and two hemispherical roughness elements of $h^+=hu_\tau/v=95$ in a turbulent flow. The far field acoustics were determined from the Curle(1955)-Powell(1960) integral solution for an acoustically compact element. It was determined from their simulation of the single roughness element that a spanwise aligned drag dipole existed that

dominated the sound produced by any streamwise dipole. They attempted to isolate the unsteady drag and diffraction mechanisms by lifting the no-slip boundary condition eliminating the drag dipole, but they could only conclude that the drag dipole seemed to produce the majority of the low frequency content at a non-dimensional frequency (*fδ/U*$_o$) less than 3.2. With the addition of the second hemisphere placed in the wake of the leading element, both the streamwise and spanwise dipole intensities increased having a larger effect on the streamwise source. The spanwise dipole seemed to increase over the entire frequency range while the streamwise dipole produced a spectral peak at at *fδ/U*$_o$~ 5 an order of magnitude greater than the single element spectra.

Glegg & Devenport (2009) present one of the most current perspectives on roughness noise generation and was largely conceived after the bulk of the measurements in this study, inspired by its results. Considering earlier measurements that displayed a surface shape dependence more complex than a just roughness height, Glegg & Devenport's (2009) new "*Unified Theory*" expands the theory of diffraction so that the radiated noise is a function of a convolution integral of the surface pressure wavenumber spectrum and the wavenumber of the surface slope. There theory is shown in Equation 1.2.

$$\Phi_{pp}(\boldsymbol{x}, \omega) \approx \frac{4\pi^2 (k_o h)^2 \Sigma \Phi_{PP}(\omega)}{|\boldsymbol{x}|^2} \int \Psi_{PP}(\kappa_1, \kappa_3, \omega) \Gamma(\kappa_1, \kappa_3, k_o) d\kappa_1 d\kappa_3 \qquad \text{Eq. 1.2}$$

$\Phi_{pp}(\boldsymbol{x}, \omega)$ is the radiated far field noise, k_o is the acoustic wavenumber, h is the roughness height, $\Phi_{PP}(\omega)$ is the single point wall pressure spectrum, Γ is a wavenumber filter function, and Ψ_{PP} is the surface pressure spectra as a function of surface wavenumber divided by the point wall pressure spectra. Glegg & Devenport (2009) describe the roughness scattering effect as a wavenumber filter for the surface pressure spectrum and executes his theory for Howe's hemispherical surface model, a wavy wall, and a discontinuous rough surface. The hemispherical model yields the exact results of Howe (1998). The wavy wall results show that it could be possible to explore low wavenumber regions of the wall pressure wavenumber spectrum by scattering the desired frequency with a sinusoidal surface. This method could produce results that are unobtainable by conventional methods. For the discontinuous surface, the calculated filter function became wavenumber white meaning the scattered spectrum is not dependent upon the wavenumber spectra of the surface. Since most naturally occurring surfaces are discontinuous, this is a convenient result. The radiated sound is only a function of the surface pressure spectrum, the observer location, acoustic wave number, and roughness height. Table 1.1 gives a brief overview of the discussed roughness noise experiments and theories presenting the history and state of the current research.

Author & Year	Experimental Description	Examined/Proposed Scalings
Skudrzyk & Haddle (1960)	Spinning cylinder with roughness in hydroacoustic water tank	-
Chanaud (1969)	Spinning disk with roughness	-
Cole (1980)	David W. Taylor Naval Ship Research and Development Center's Anechoic Flow Facility rough wall far field and wall pressure measurements, examined dipole and quadrupole theories	$\dfrac{\Phi_{pp}(\omega)}{(\rho/c_\infty)^2 U^5 \delta*} \sim f\left(\dfrac{\omega \delta*}{U}\right)$ $\dfrac{\Phi_{pp}(\omega)}{(\rho/c_\infty{}^2)^2 U^7 \delta*} \sim f\left(\dfrac{\omega \delta*}{U}\right)$
Hersh (1983)	Roughened pipe flow	-
Howe (1988)	Theoretical, diffraction theory using Chase's (1987) smooth wall pressure spectra model	$\dfrac{\Phi_{pp}(\omega)}{(\rho/c_\infty)^2 u_\tau^5 h} \sim f\left(\dfrac{\omega h}{u_\tau}\right)$
Farabee & Geib (1991)	David W. Taylor Naval Ship Research and Development Center's Anechoic Flow Facility rough wall pressure spectra measurements	$\dfrac{\Phi_{pp}(\omega)}{(\rho/c_\infty)^2 u_\tau^4 U \delta*} \sim f\left(\dfrac{\omega \delta*}{U}\right)$
Liu *et al.* (2007)	Far field measurements from hemispherical roughness implementing Howe's (1988) theory	-
Glegg *et al.* (2007)	Theoretical, introduced roughness correlation length into normalization	$\dfrac{\Phi_{pp}(\omega)}{(\rho/c_\infty)^2 u_\tau^4 U(h^2/l_e)} \sim f\left(\dfrac{\omega l_e}{U}\right)$
Grissom (2007)	Analysis of far field noise from rough surfaces examining character of roughness noise and multiple normalization suggestions	-
Liu *et al.* (2008)	Phased array measurements of hemispherical roughness with updated beam forming algorithm	-
Yang & Wang (2008)	LES simulations of hemispherical roughness elements using Curle (1955)-Powell (1960) integral solution to find far field acoustics	-
Glegg & Devenport (2009)	Theoretical, radiated noise is a function of wall pressure and surface wavenumber	$\dfrac{\Phi_{pp}(\omega)}{(k_o h)^2 \Sigma \Phi_{PP}(\omega) \int \Psi_{PP} \Gamma d\kappa_1 d\kappa_3}$

Table 1.1 Experimental studies and description

1.3 Objectives

Recent progress in roughness noise theory has spurred more in depth and focused analysis of the topic. This study details roughness noise measurements taken in the Virginia Tech Anechoic Wall Jet Facility as well as facility improvements enhancing the acoustic function of the tunnel. Wall pressure measurements were performed for 11 different stochastic rough surfaces as well as a 1mm and 3mm hemispherical surfaces and a 2D near-sinusoidal rib surface with simultaneous measurements of the radiated far field spectra. These measurements coincide with test cases from previous studies including Grissom (2007) and Smith (2008). This study is a continuation of the previously published research of Smith *et al.* (2008) which details initial results of the present work. The objectives of this paper are the following:

- Analysis of far field sound and wall pressure spectra for stochastic roughness with roughness heights varying from hydrodynamically smooth to fully rough
- Analysis of far field sound and wall pressure spectra for deterministic surfaces including hemispherical and 2D rib surfaces
- Application of theories proposed by Cole (1980), Howe (1988), Glegg *et al*. (2007), and Farabee & Geib (1991) comparing with the results of Grissom (2007) and characterizing the status of roughness noise theories prior to Glegg & Devenport (2009)
- Bring together the far field sound study of Grissom (2007) and the wall pressure study of Smith (2008) along with new data to examine the relationship between the near and far field pressure fluctuations
- Application of Glegg & Devenport's (2009) "*Unified Theory*" for far field noise generated by stochastic and deterministic surfaces

Chapter 2 Apparatus and Instrumentation

2.1 Virginia Tech Wall Jet Tunnel

All data presented were taken in the Virginia Tech Anechoic Wall Jet Facility shown in Figure 2.1, used previously by Grissom (2007) and Smith (2008).
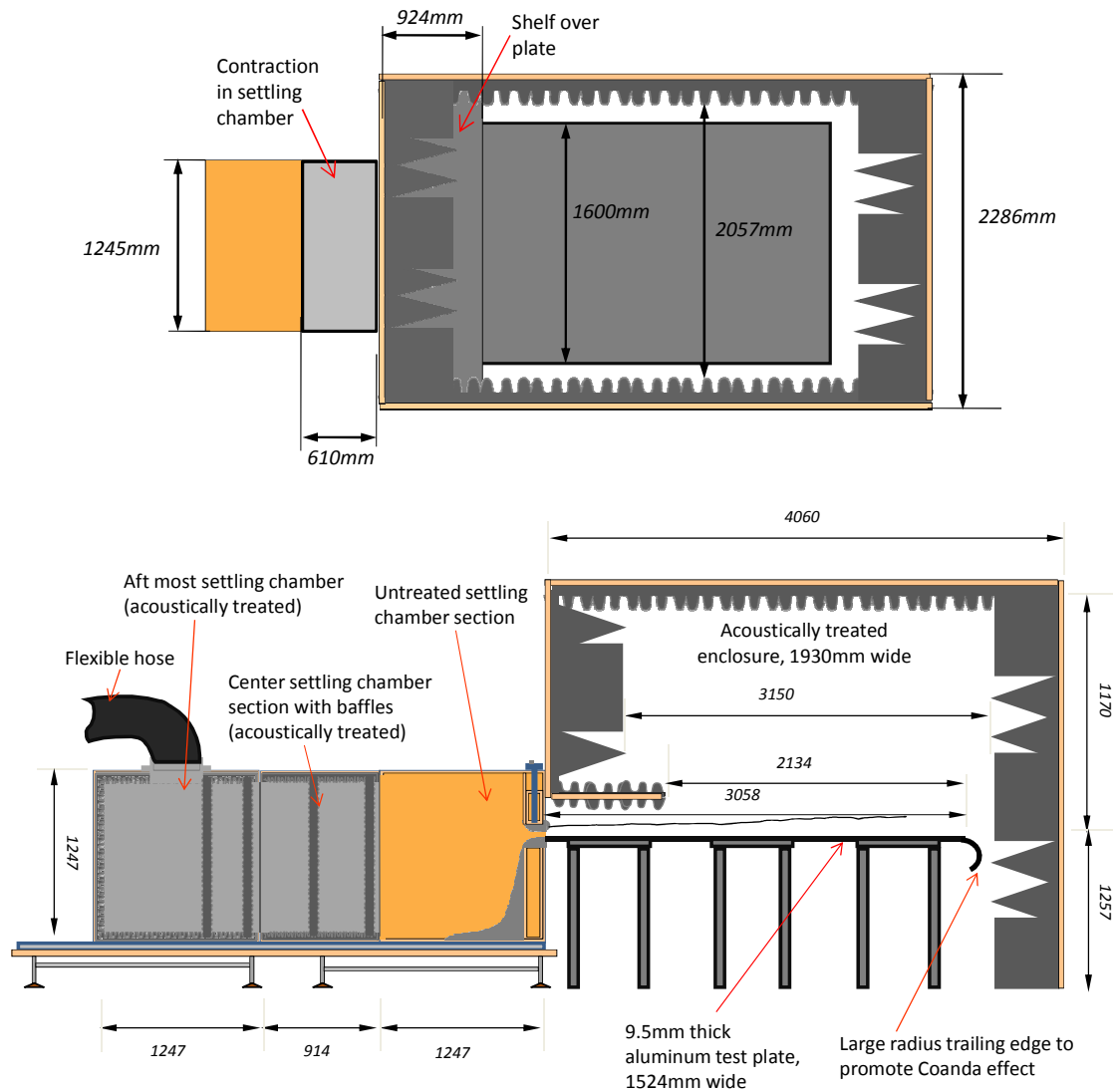
Figure 2.1 Virginia Tech Anechoic Wall Jet Facility

This tunnel produces a 1206mm wide two dimensional wall jet over a 3058mm long aluminum plate. The plate is 1600mm wide so that the wall jet is contained well within the spanwise edges of the plate. The tunnel is powered by a Cincinnati Fan variable speed centrifugal fan model HP-8D20 which is separated from the settling chamber by a SSA-8 steel discharge silencer and flexible rubber hose. The rubber hose exhausts into a settling chamber with a series of acoustically treated baffles that block direct radiation of sound from the blower through the nozzle. The flow is then accelerated through a variable height nozzle

over a flat plate and dissipates into the lab atmosphere. The height of the nozzle is controlled by two large hand-turned screws allowing the top section of the nozzle to traverse vertically. The nozzle height is then measured by placing gauge blocks of the desired height in the nozzle plane at the nozzles outer corners and lowering the upper section until contact. The upper lip of the nozzle is milled from PVC and has a slight height deviation along its span. This deviation has a u-shape profile across the span making the centerline of the nozzle the lowest section by approximately 1.2mm. The method used to set the nozzle height was accurate within 0.5mm resulting in a 1257mm downstream uncertainty up to 2% of the maximum local velocity.

The nozzle height control limited the design of the contraction in the settling chamber. The upper section of the contraction is a combination of two smooth 90° turns leading to the nozzle exit. It had to be left free to traverse vertically depending on the desired nozzle height so the curves are fixed and unaffected by the nozzle position. Figure 2.2 shows a close up of the nozzle section. There is a 154mm radius 90° turn from the settling chamber towards the nozzle. The flow makes another 90° turn toward the nozzle exit over an elliptically shaped lip. The upper nozzle shape is a combination of a quarter ellipse with a 3:1 aspect ratio on the inside of the throat spliced with a 38.1mm radius circular profile on the outside to manage edge noise. Because the lower lip of the nozzle was stationary, the lower contraction in the settling chamber is a single smooth curve designed using Equation 2.1 by Fang *et al.* (2001).

$$y = (h_1 - h_2)\left[1 - \frac{1}{X_m^2}\left(\frac{x}{L}\right)^3\right] + h_2 \qquad \text{Eq. 2.1}$$

h_1 is the final contraction height and h_2 is the initial height measured from a reference plane, x is the distance from the nozzle exit, L is the full length of the contraction and X_m is the distance to the matched point. The design values used for this tunnels contraction were h_1=681mm, h_2=0, X_m=254mm, and L=610mm.

The entire aluminum plate is contained in an acoustically treated enclosure that has a shelf 330mm off of the plate surface. This shelf blocks microphones placed in the acoustic far field from any direct radiated jet noise from the nozzle. The shelf can be seen in Figure 2.2 extending out over the plate.
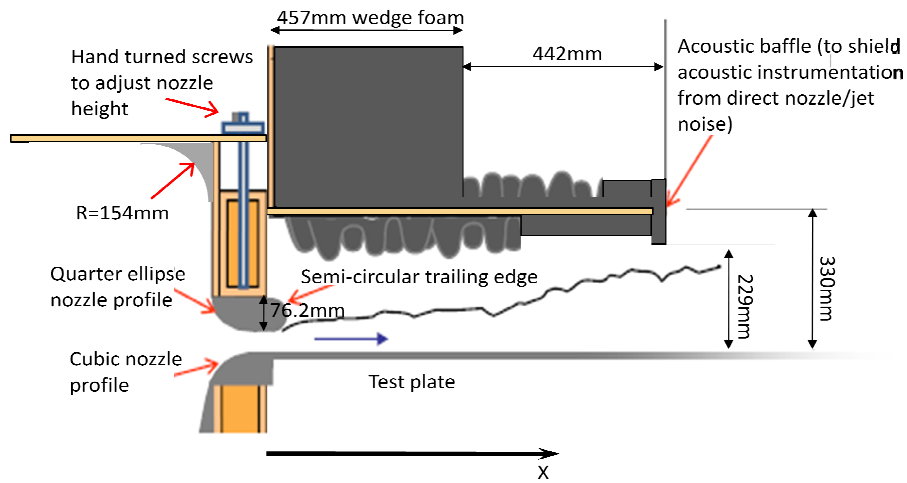
Figure 2.2 Nozzle Section

The shelf is made of 25.4mm MDF covered in 89mm egg crate foam giving the shelf on overall thickness of 203mm. It covers the entire width of the chamber overlapping 924mm of the plate streamwise. The microphones placed above this shelf are well outside of the mixing layer of the wall jet. The resultant microphone measurements are of the radiated noise only and not the turbulent flow pressure fluctuations.

25.4mm thick MDF was used to construct the walls of the settling chamber, blower housing, nozzle, and acoustic plate enclosure. The settling chamber walls and acoustic enclosure's walls are reinforced with square steel tubing along all sides except the floor of the acoustic chamber which is left open creating an open box shape leaving its walls some ability to flex. The high pressure of the settling chamber and open box shape of the acoustic chamber have presented some problems due to the strength and rigidity of the MDF. The nozzle had been observed to buckle outward up to 12.7mm during operation inadvertently increasing the height of the nozzle by nearly 1mm and requiring that the fan be operated at a higher RPM to produce the same nozzle velocity. This change in nozzle height could have also increased the flow speed downstream due to the increased momentum of the thicker flow. This could have produced some of the inconsistencies in data from previous studies but measures were taken to eliminate this problem in all current data. Fan speeds were checked to ensure that all data presented were taken at the same nozzle conditions and the nozzle was reinforced to keep it from deforming.

The flexibility of the chamber's walls created some uncertainty when placing the chamber over the plate. The entire acoustic enclosure is on wheels making it removable for easier access to the plate's surface for aerodynamic measurements. Its position is made repeatable by marks drawn on the floor of the lab outlining the wheel arrangement, but because the walls bend, the uncertainty of the relative distance from plate to wall is ±50mm.

The acoustic treatment in the chamber is made of 89mm egg crate foam and 457mm wedges on the leading and trailing walls which dissipate acoustic energy at frequencies above approximately 1900Hz and 188Hz, respectively. The low noise environment of the chamber allows for strong signal to noise ratios of roughness noise.

Experiments by Grissom (2007) have shown that the aluminum plate is long and wide enough that no edge effects contaminate the far field noise and that the background noise of the tunnel is dominated by the jet noise of the wall jet flow. Figure 2.3 shows the increase in overall SPL for flow over

the smooth plate for varying speeds. When compared to the SPL velocity scaling for a dipole, U^6, and a quadrupole source, U^8, the data falls in line with the quadrupole indicating that the background noise is dominated by the turbulent flow from the wall jet.
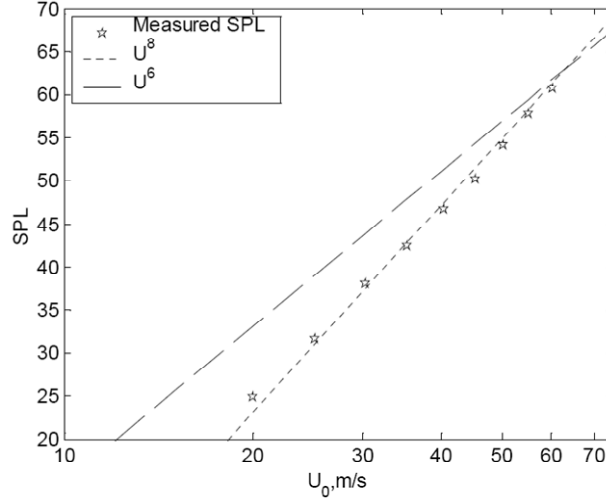
Figure 2.3 Integrated SPL of background noise variation with nozzle speed (Grissom, 2007, used with permission)

The aerodynamic characteristics of the flow have been examined by Smith (2008) for 12.7 and 25.4mm nozzle heights with nozzle speeds ranging up to 60m/s and 40m/s, respectively. Smith (2008) has found that the flow remains two dimensional for the center 810mm of the leading 1867mm of the plate. All measurements completed in this study were taken from positions well within this two dimensional region or with roughness fetches embedded within this region. Aerodynamic measurements completed by Smith (2008) also show that the wall jet flow behaves as a standard wall jet and vertical mean-velocity profiles can be scaled on U_e, the peak mean velocity, and $y_{1/2}$, the height above the peak velocity location at which the mean velocity is at half its maximum value. The streamwise development of the flow can be characterized with the scalings of Narasimha *et al.* (1973) and Wygnanski *et al.* (1992) for U_e and δ_{90}, the height at which the peak mean-velocity is 90% of its maximum value, with the constants for this tunnel being n=-0.512 and A_U=4.97 for Equation 2.2 and m=0.914 and A_Y=0.0259 for Equation 2.3.

$$\frac{U_e}{U_o} = A_U Re_j^{n+1} Re_{x-x_o}^n \qquad \text{Eq. 2.2}$$

$$\frac{\delta_{90}}{h} = A_Y Re_j^{m-2} Re_{x-x_o}^m \qquad \text{Eq. 2.3}$$

Re_j is the jet Reynolds number from the nozzle, $U_o b/\nu$, and Re_{x-x0} is the Reynolds number based on streamwise location, $U_o(x - x_o)/\nu$, where x_o is zero and x is measured from the nozzle exit plane. Other profile characteristics can be approximated by the linear fits to δ_{90} in Equation 2.4.

$$\delta_{90} \approx 0.252\delta \qquad \text{Eq. 2.4}$$
$$\delta^* \approx 0.0746\delta$$
$$\theta \approx 0.0549\delta$$
$$y_{1/2} \approx 7.11\delta$$

δ is the boundary layer thickness, δ* is the displacement thickness, and θ is the momentum thickness. Smith (2008) produced different results when scaling his aerodynamic data, but a careful study concluded that his fits have been skewed by the inclusion of data 38.1mm from the nozzle exit. The mean velocity profiles from this position are very square and do not accurately represent a fully developed wall jet nor are the profile characteristics well defined by the profile shape.

All microphones and rough surfaces were positioned relative to a fixed coordinate system shown in Figure 2.4. The x-value is the streamwise progression, z is spanwise, and y is vertical. The origin of the axis is at the spanwise center of the nozzle exit in the plane of the plate where the plate meets the lip of the nozzle.
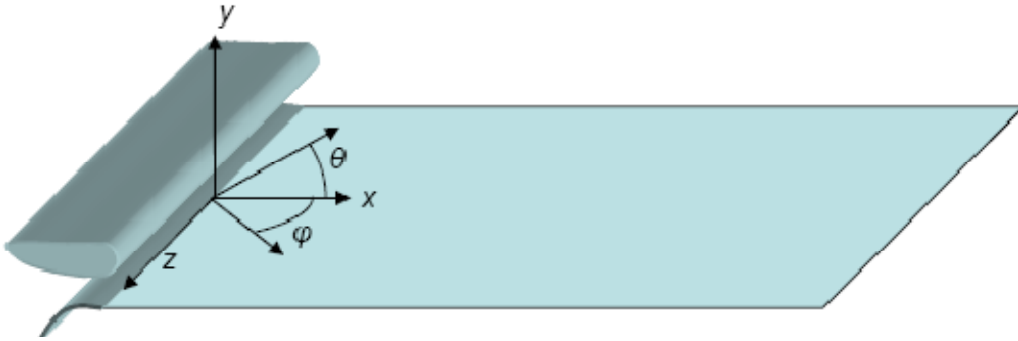
Figure 2.4 Coordinate system

2.2 Wall Pressure Instrumentation Configurations (A)-(B)

Surface pressure fluctuations were recorded with Sennheiser KE-4-211-2 electret condenser microphones which have a 10mV/Pa nominal sensitivity. The Sennheisers have a flat frequency response up to 10kHz within 1dBm. The pinhole size of the microphones was modified from the factory 1mm diameter hole to 1/4mm to resolve higher frequency pressure fluctuations. Smaller pinholes allow more accurate measurements of shorter length scale convected eddies which pass over the microphones at higher frequencies. The 1/4mm pinholes have the capability to resolve eddies producing frequencies below approximately 23kHz within 3dB of the true values. This is calculated using the microphone's maximum encountered local edge velocity when mounted in the plate, 22m/s at x=1302mm, and assumes a convective velocity that is 60% of the edge velocity. This is a reasonable assumption for convective velocity according to Blake (1970) using a 20m/s edge velocity with δ*=1.114mm. Under the same assumption, the 1mm pinhole would have only been able to accurately measure frequencies below 5.8kHz.

Two series of surface pressure measurements were recorded employing slightly different methods. Discussions of the initial surface pressure measurements will be compared with recent measurements which use an improved method of microphone placement and design. Therefore, both microphone configurations will be described. The initial pinhole measurement technique was studied in depth and used by Smith (2008) and Smith *et al.* (2008) using the author's help for calibration measurements. The later technique was developed and studied solely by the author. For the early measurements, which will be denoted as Microphone Configuration (A), pinhole caps for the Sennheisers were created by Smith (2008). They were 0.13mm thick Mylar disks with 1/4mm holes affixed to the tops

of the Sennheisers' casing directly over the 1mm factory holes. These had a tendency to detach during measurements and their recorded wall pressure spectra had some questionable characteristics. The improved method, which will be referred to as Microphone Configuration (B), used 0.26mm thick brass shim stock with 1/4mm holes instead of the Mylar caps. The outer edge of the brass caps were sealed to ensure that no flow could enter between the cap and Sennheiser top. A diagram of the microphone pinhole cap design is shown in Figure 2.5.
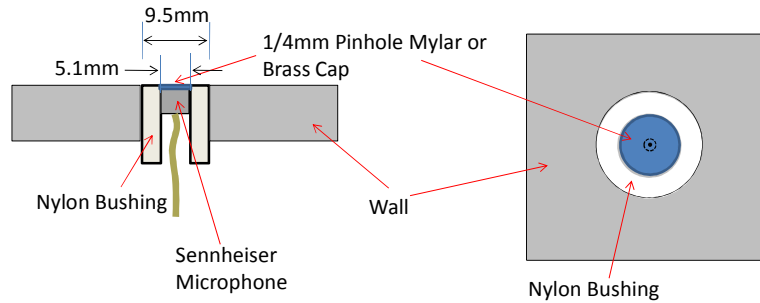
Figure 2.5 Wall pressure microphone design diagram (side and top views)

Calibrations for all of the wall pressure microphones were completed in the anechoic chamber of the wall jet. The calibration set-up is shown in Figure 2.6. The aluminum plate was covered with 25.4mm melamine foam and a speaker was placed on top of the chamber's shelf pointing downstream where the microphones were placed 1956mm from the speaker face. Both the speaker and microphone were placed approximately 460mm above the plate and at a location 230mm off the spanwise centerline of the plate. The microphones were mounted on a slender rod extending out from a vertical stand to limit any near field interference. A University Sound model ID60C8 speaker driven by an Agilent VXI data acquisition system was used to provide white noise for the calibration.
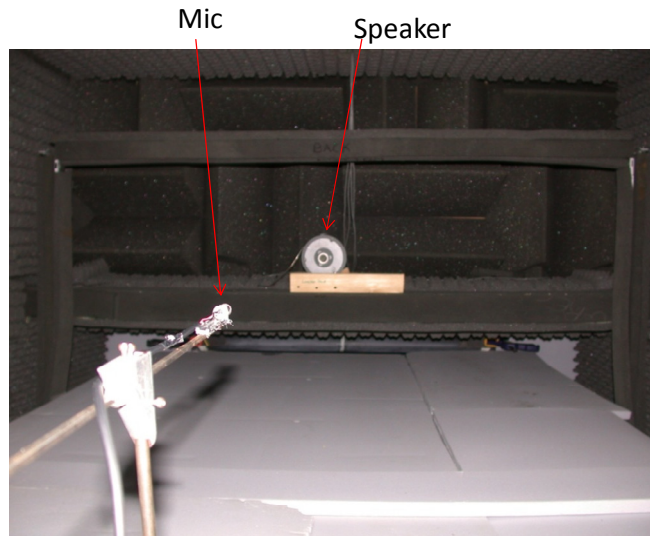
Figure 2.6 Wall pressure microphone calibration set-up

The output speaker signal was first calibrated using a $1/8^{th}$ inch B&K type 4138 microphone with a flat frequency response ±1dB out to 25.6kHz. The speaker calibration was determined by dividing the

13

cross spectrum of the B&K measured signal and the speaker's input signal with the autospectrum of the input to the speaker and the $1/8^{th}$ inch B&K's sensitivity. After the speaker calibration was complete, the Sennheisers' calibrations could be determined. The calibrations were calculated by dividing the cross spectrum of the measured speaker output and the speaker's input signal by the autospectrum of the input signal and the speaker calibration. This calculation is shown in Equations 2.5 and 2.6 where $S_{1/8th}$, S_{Senn}, and S_{Speak} are the measured voltage signals from the microphones and speaker input and $(1/8th\ Sensitivity)$ is the $1/8^{th}$ inch B&K's sensitivity measured in V/Pa. The resultant simplification of Equation 2.6 shows that M_{Cal}, the Sennheiser calibration, is equal to the response of the Sennheiser divided by that of the calibrated $1/8^{th}$ inch B&K.

$$\text{Speaker}_{Cal} = \frac{S_{1/8th}\ \bar{S}_{Speak}}{\left|S_{Speak}\right|^2 (1/8th Sensitivity)} \qquad \text{Eq. 2.5}$$

$$M_{Cal} = \frac{S_{Senn}\ \bar{S}_{Speak}}{\left|S_{Speak}\right|^2 (\text{Speaker}_{Cal})} = \frac{S_{Senn}}{S_{1/8th}/(1/8th Sensitivity)} \qquad \text{Eq. 2.6}$$

Calibrations were smoothed using the same technique as Smith (2008) to filter out signal noise and reduce the uncertainty of the calibration. For frequencies below 800Hz, the calibration was taken to be the average value of that range. Between 800Hz and 2kHz, the spectra was averaged on $1/24^{th}$ octave bands. Above 2kHz, the values were averaged over $1/12^{th}$ octave bands. Figure 2.7 shows a comparison of smoothed calibrations for a factory 1mm pinhole and brass 1/2mm and 1/4mm pinhole modifications. The smaller pinhole sizes reduce the sensitivity of the microphones at high frequency. Although the 1/4mm pinhole had significant sensitivity loss above 7kHz, it was still sufficient for the current study.
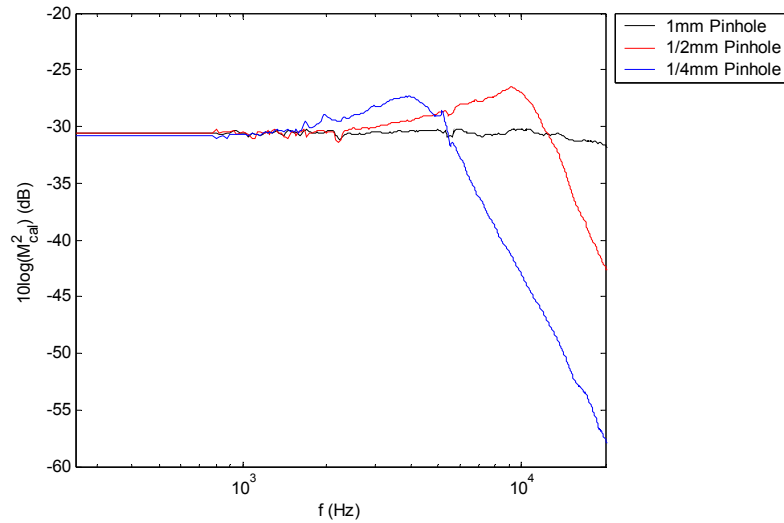
Figure 2.7 Calibration of a Sennheiser with three different pinhole sizes

To measure the wall pressure spectra, the calibrated Sennheisers were positioned through holes drilled in the surface of the plate and roughness. The microphones were inserted into nylon bushings before installation on the plate surface enhancing their outer diameter from 5.1 to 9.5mm. The microphones were then positioned vertically between the mid height and the tops of the roughness by displacing the Sennheiser the desired vertical distance relative to the outer bushing. Smith (2008) states

that the surface pressure was independent of vertical placement for locations above the bottoms of the roughness grains, but there were also repeatability issues in his measurements that show variations in his data sets up to 2dB. Figure 2.8 shows the vertical position results and the noted repeatability problem as recorded by Smith (2008) and corresponds to the method of Microphone Configuration (A). The plots on the left were created by placing a 203x279mm patch of 40grit sandpaper, with unknown orientation, on the surface of the plate starting at x=1257mm with a surface pressure microphone embedded in the rough surface 45mm from the leading edge. The patch was never moved while the height of the microphone was adjusted. When the microphones were placed below the roughness substrate, the spectral levels and shape were altered particularly in the high frequency range where the spectra dropped off much faster. There is only a 0.75dB maximum difference between the 0.5h and 0.0h positions. The plot on the right was produced by holding the streamwise and vertical position of the microphone constant at x=1302mm and 0.85h below the roughness tops. A 203x203mm patch of 40grit sandpaper surrounded the microphone and was removed and replaced once with the microphone positioned into the same cut out and another time with microphone moved into a new hole of the same diameter. For this fixed vertical position, the measurement shows an uncertainty range of 2dB. Smith (2008) suggests using a ±1dB uncertainty due to microphone location on top of the inherit uncertainty of the repeatability of the calibration. This may be an underestimate because it only accounts for the uncertainty in the vertical positioning of the microphone and not the error between similar consecutive measurements. The uncertainty, excluding the calibration uncertainty, could be closer to ±2dB.
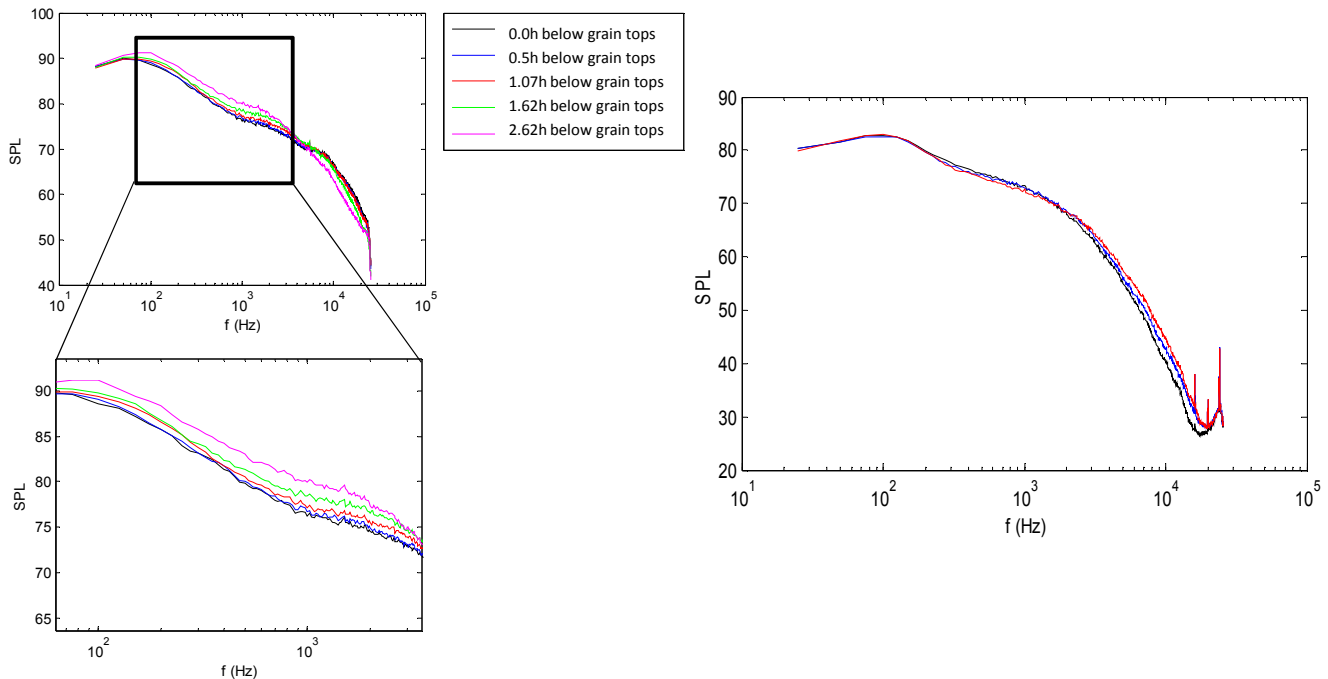
Figure 2.8 Repeatability of surface pressure measurements for a 40grit patch: with variation in microphone vertical placement (left), and with vertical placement held constant at 0.85k below the roughness tops (right) using Microphone Configuration (A) (modified Smith, 2008, used with permission)

For the surface pressure measurements with Mylar capped Sennheisers, Microphone Configuration (A), the microphones were positioned through a hole in the roughness larger than the diameter of the microphone, 7.3mm and 5.1mm, respectively. This created a ring-shaped cavity the depth

of the roughness substrate surrounding each microphone. For Microphone Configuration (B), the holes in the sandpaper were the same diameter as the Sennheiser microphone so that there was no cavity. For the smooth plate measurements in both studies, the microphones were flush mounted within the plane of the plate. For Microphone Configuration (A), there were five surface pressure microphones placed starting at x=1302mm on the centerline of the plate and spaced every 50.8mm until x=1505mm. For Microphone Configuration (B), there were three microphones at x=1353mm, 1403mm, and 1505mm. The two configurations are shown in Figure 2.9.
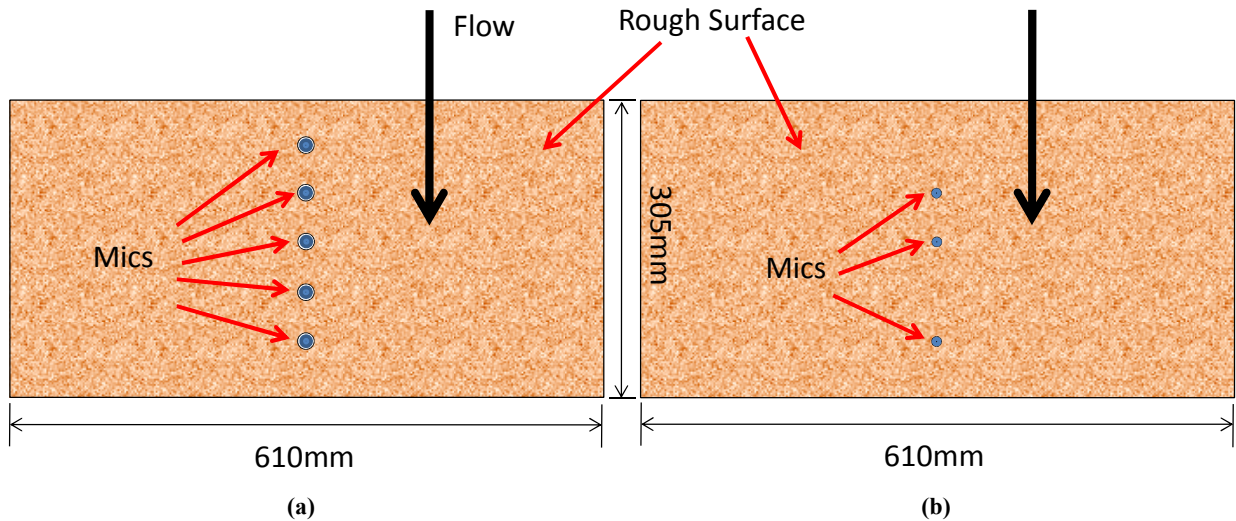
Figure 2.9 Wall pressure microphone locations for (a) Microphone Configuration (A) (b) and Microphone Configuration (B) viewed from the top

In both measurement series, the Sennheisers were used in conjunction with 5V DC power supplies and amplifiers made in house by Mish (2003). These amplifiers had a gain of approximately 2.5 boosting the nominal sensitivity of the Sennheisers to 25mV/Pa. Data were taken using an Agilent E1432 16-bit digitizer and all spectra are an average of 1000 records of 2048 samples recorded at 51200Hz. The signals were low passed filtered at 20kHz to prevent aliasing.

2.3 Far Field Instrumentation

2.3.1 Far Field Microphone Configuration (A)

Parallel to the improvements of surface pressure measurement methods denoted as Microphone Configurations (A) and (B), which enhanced the quality of recorded spectra, far field measurement techniques also were advanced to improve quality. A detailed description of the initial and subsequent methods will be given that corresponds with the same Microphone Configurations (A) and (B), respectively. Microphone Configuration (A) was the same method as employed by Grissom (2007). For Microphone Configuration (A), all of the far field data were taken with four ½" B&K 4190 free-field microphones powered by a B&K Nexus 2690 A0S4 amplifier. These microphones have a flat frequency response out to 20kHz and their measured signals were band filtered between 250Hz and 20kHz focusing on the frequency range where roughness noise is perceptible by the measurement system and preventing signal aliasing at higher frequencies. For all far field measurements, the signals of the four microphones

were averaged to produce the presented far field data. Table 2.1 lists the far field microphone locations in the anechoic chamber relative to the coordinate system described in Figure 2.4.

	x, mm	y, mm	z, mm
Mic 1	1016	533	-25
Mic 2	1016	476	-38
Mic 3	1016	476	-13
Mic 4	1016	559	152

Table 2.1 Far field microphone locations for Microphone Configuration (A)

Microphones 1, 2, and 3 were positioned in a triangle formation and Microphone 4 was located 7" laterally from the center of the triangle. These microphones were horizontally level pointing directly at the back wall of the chamber. All microphones' faces were positioned 1016mm streamwise from the nozzle so that each microphone was positioned an equal distance to the start of the roughness patch.

The microphones were held in place using a combination of steel dowels, a short tripod stand, and rotating set screw type mounts. A photograph of the microphones is shown in Figure 2.10.
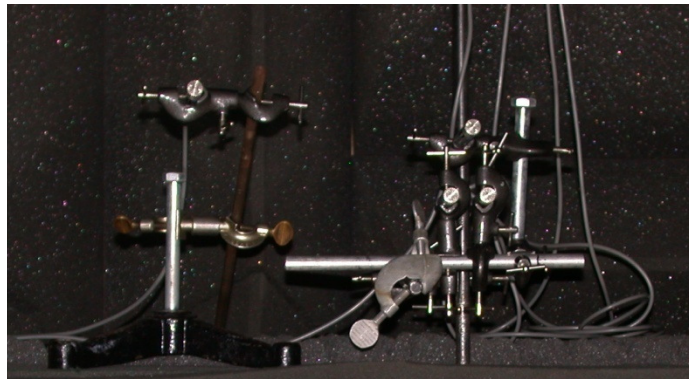
Figure 2.10 Microphone mounts for Microphone Configuration (A)

These mounts are approximately 111mm in length and are of considerable size compared to the microphones themselves. There was no specific repeated method of stand and mount placement but there were some recurring patterns due to the limitations of the stands. For instance, mounts were often positioned within 51mm of the microphone face because of the short length of the microphones, 89mm. The steel dowels were as large as 13mm in diameter and were normally positioned approximately 58mm away from the microphones. The microphone stands and positioning will be a topic of further discussion in Section 2.4.

Data from the far field microphones were acquired simultaneously with the presented surface pressure data but were not synchronized. Far field and near field data were taken during the same experiments but not at the exact same moment. The far field data were recorded using an Agilent E1432 16-bit digitizer separate from the wall pressure measurements. All spectra are computed as the average of 1000 records of 2048 samples recorded at 51200Hz.

2.3.2 Far Field Microphone Configuration (B)

One far field microphone aimed at the center of the roughness fetch was used to record far field noise for Microphone Configuration (B). The signal was band filtered from 250Hz-20kHz the same as Microphone Configuration (A). The single microphone's position is listed in Table 2.2.

x, mm	y, mm	z, mm	θ
1029	473	0	-38.8°

Table 2.2 Single far field microphone location for Microphone Configuration (B)

Unlike Microphone Configuration (A), the far field measurements in Microphone Configuration (B) were synchronized with the surface pressure measurements so that they were taken at the exact same moment. The far field data were recorded using an Agilent E1432 16-bit digitizer. All spectra are computed as the average of 1000 records of 2048 samples recorded at 51200Hz.

2.4 Response Function of the Anechoic Chamber and Microphone Support System

The response function was determined using a point source emitting white noise from the surface of the plate and measuring the far field acoustics at desired response locations. The results were compared to the measured far field from a reference position taken simultaneously. Half-inch B&K 4190 free-field microphones were used for the far field measurements. The point source was generated using a Koss SparkPlug SP3 ear bud headphone projecting through a 3.6mm diameter hole in the plate located at x=1353mm. The headphone was transmitting white noise generated by an Agilent E1432 16-bit digitizer. Figure 2.11 shows the calibration measurement set-up and a diagram of the speaker arrangement. Three far field microphones were positioned in the triangle configuration relating to the initial roughness noise measurements of Microphone Configuration (A) as listed in Table 2.1. The reference microphone was positioned on the end of a long wooden dowel rod and angled to point directly at the source location at a position roughly 100mm above the plate. Its radial distance from the source was modified from 180 to 430mm by adjusting the position of the dowel. All microphone positions were measured using a FARO Fusion Arm for accuracy.
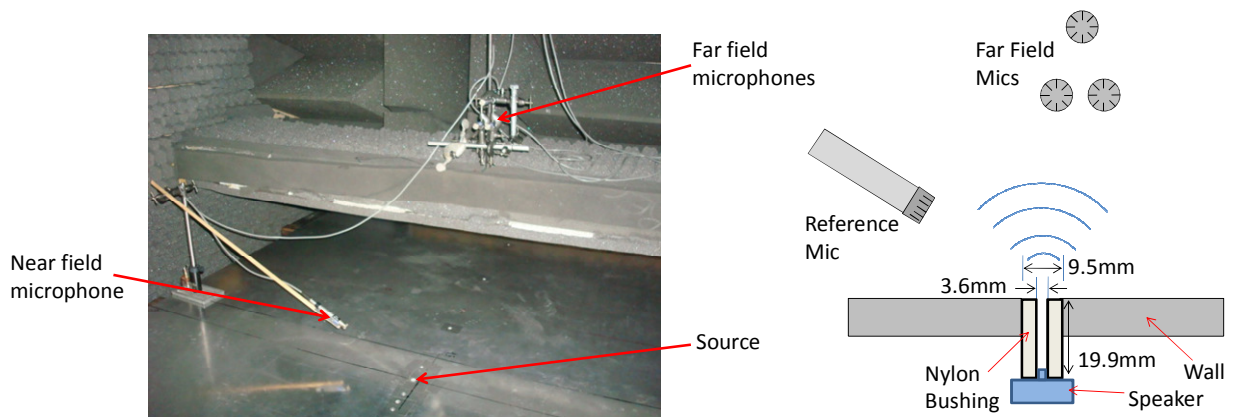

Figure 2.11 Chamber calibration set-up picture and diagram (not to scale)

First, the position of the reference microphone was varied to confirm that the microphone was not affected by its local position. The source was shown to behave as a monopole by taking measurements of increasing distance from the source and scaling the recorded pressure on the radial distance. A monopole's intensity should function as the inverse of the radial distance of the observer. Figure 2.12 shows this scaling of spectra. The tight collapse of Figure 2.12 (b) shows that the sound was behaving as a monopole and that the reference microphone was not disturbed by any chamber effects.
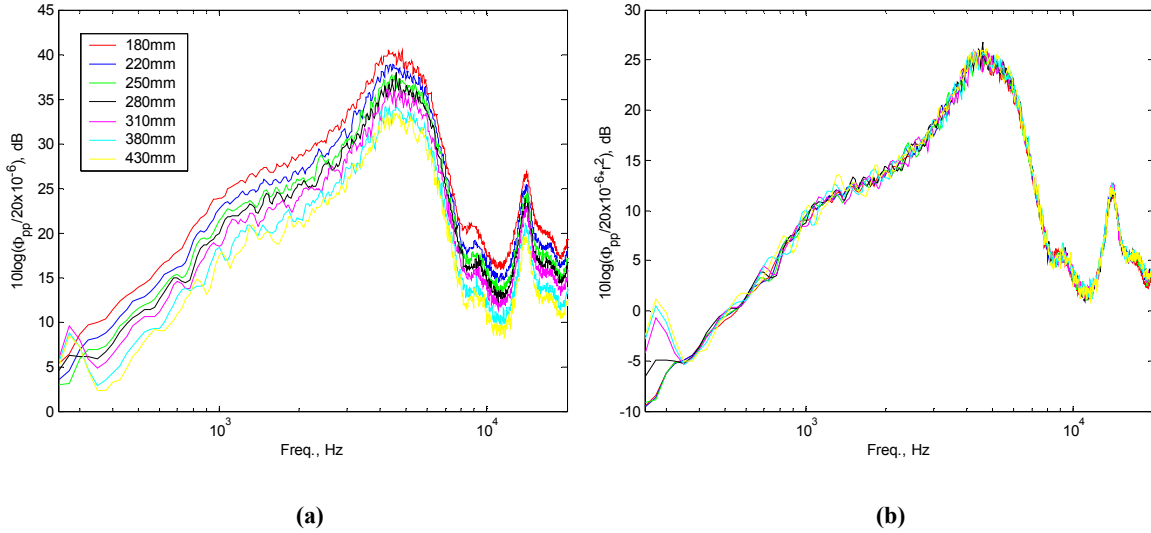

(a)   (b)

Figure 2.12 (a) Raw near field spectra (b) and scaling of spectra on observer distance squared

A phase check was completed by plotting the measured distance from the source to the reference microphone versus the inferred distance from the phase offset between the reference microphone and desired far field measurement. This inferred distance is a measure of the difference between the two microphones' radial distance to the source. The inferred distance was calculated using Equation 2.7 and 2.8.

$$\tau = \frac{\partial \Phi}{\partial \omega} \qquad \qquad \text{Eq. 2.7}$$

$$distance = \tau c_o \qquad \qquad \text{Eq. 2.8}$$

$\frac{\partial \Phi}{\partial \omega}$ is the slope of the phase per angular frequency between the reference microphone and far field microphone, τ is the time delay of an acoustic wave reaching both microphones as a function of angular frequency, and c_o is the speed of sound. $\frac{\partial \Phi}{\partial \omega}$ is calculated using the central difference method over the entire considered frequency range giving results per frequency. The calculated time delays and distances from each frequency were averaged to obtain a final single value.

Figure 2.13 shows the results of this calculation for all three microphones in the triangle formation. The plot should have a slope of -1 because as the reference microphone to source distance changes the inferred distance should change by the same amount of the opposite sign. The nearest five reference to source locations have a slope very near -1, but the furthest two increasingly deviate from the expected result indicating that the phase at these positions is being affected by the increase in distance from the source.
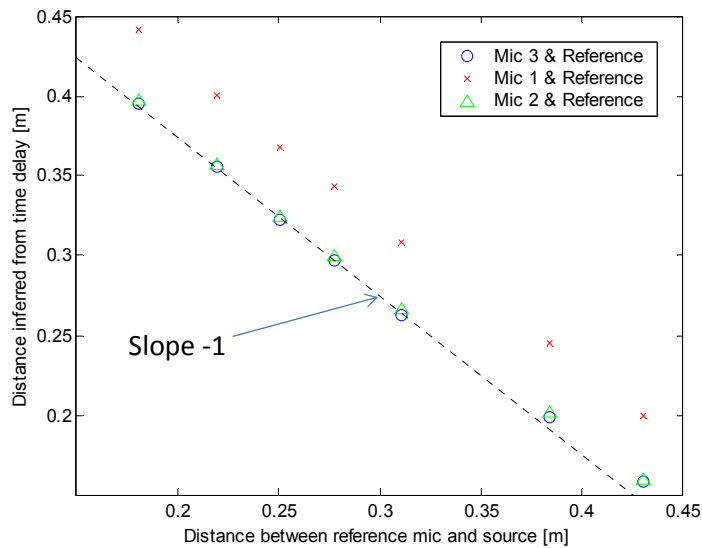
Figure 2.13 Phase check of cross spectra between reference mic and far field

For the rest of the study, measurements were taken within the closest five reference-source distances ranging from approximately 170mm to 320mm so as not to introduce any phase error.

Next, data with coherence below 0.95 between the reference and desired microphone were ignored so that uncorrelated sound sources did not interfere with the analysis. Figure 2.14 shows the coherence for Microphone 1 of the triangle for several different reference microphone distances. The data shows that the coherence was significant above approximately 500Hz to 20kHz. Therefore, the data below approximately 500Hz were ignored in later calculations of acoustic response function. The other two microphones exhibited similar coherence with the reference microphone response.
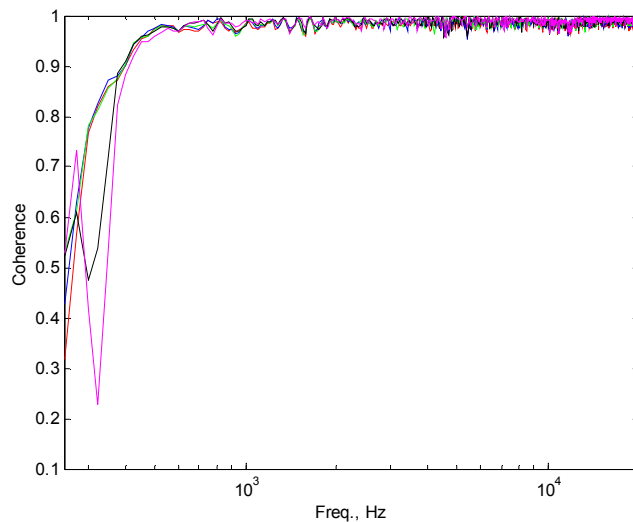
Figure 2.14 Coherence of the Microphone 1 position

The resulting data were used to calculate an acoustic response function by taking the magnitude of the cross-spectra divided by the autospectrum of the reference response resulting in essentially the far field signal divided by the reference response. The mean of the response was subtracted so that the plots are centered about zero. Figure 2.15 shows the acoustic response function for all three microphones for multiple reference microphone positions. The spectra are marked by large oscillations and an overall decay with increasing frequency.

(a)   **(b)**   **(c)**

Figure 2.15 Acoustic response function for (a) Microphone 1 (b) Microphone 2 (c) and Microphone 3 with varying reference microphone to source distances

All three microphones display a similar response. The oscillations occur at equivalent frequencies and have similar decibel ranges. The consistencies of the response function with variations in reference microphone distance also indicate that the reference microphone had no contribution to these large oscillations.

2.5 Microphone Stand and Traverse Design

The high frequency decay illustrated in Figure 2.15 could be attributed to the angle of the microphone face to the wave fronts of the monopole source, ~34°. To capture the frequency response of the chamber correctly, the microphones face should be parallel to the wave fronts. As the angle deviates from parallel, the microphone response to the acoustic pressure waves becomes an average of the portion of the sine wave across the face of the microphone at each frequency. As the frequency increases, the average becomes a larger portion of the wave and at a frequency of infinity should tend to zero. To verify the decay was due to the angle, the same triangle formation, with their relative distances to each other held constant, was angled 34° downward with the centroid of the triangle aimed directly at the source. Figure 2.16 shows the results of the modified formation.

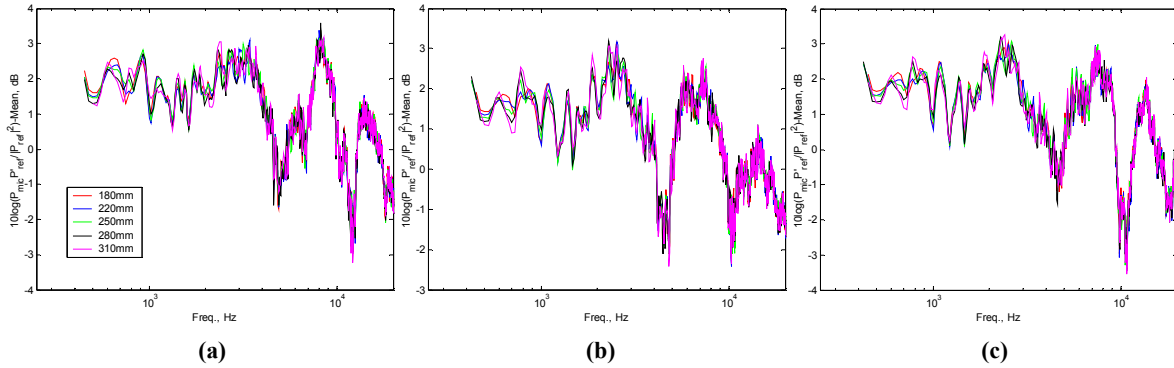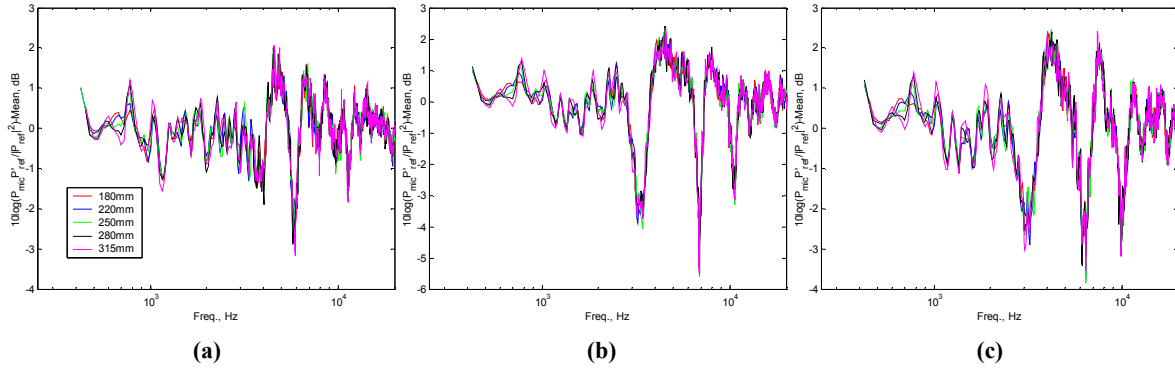**Figure 2.16 Response function of microphones aimed at source for (a) Microphone 1 (b) Microphone 2 (c) and Microphone 3 with varying reference microphone to source distances**

The decay is gone in all three microphones, but the oscillations remain. Several attempts were made to suppress the oscillations, including covering the egg crate foam with much larger wedge foam to increase the chamber's frequency range of acoustic absorption and rounding the chamber's square shelf frame to prevent edge scattering, none of which worked.

Note that in Figure 2.16 the oscillations in the Microphone 2 and 3 spectra have a larger range than the Microphone 1 position. These two microphones were at the bottom of the triangle and had a more similar chamber position than Microphone 1 located 57mm above them, but there was also a difference in the way Microphones 2 and 3 were held by the set screw mounts. For Microphones 2 and 3, the mounts were much closer to the faces of the microphones, ~25mm. The mount was much further from the face of Microphone 1, ~50mm, which had a more object-free near field. The set-screw mounts were positioned within one wavelength of Microphones 2 and 3 for frequencies below 13.5kHz contrasting 6.8kHz for Microphone 1, exactly where the majority of the oscillations occur for all of the respective microphones. Due to their size, close positioning to the microphones, and acoustically reflective surfaces, the microphone mounts were identified as a possible source of the large oscillations.

To test the effect of the mounts, measurements were taken with all of the original stands removed and only one microphone held by a specially designed mount covered in 25.4mm acoustic foam in the far field. The newly designed microphone mount is shown in Figure 2.17.
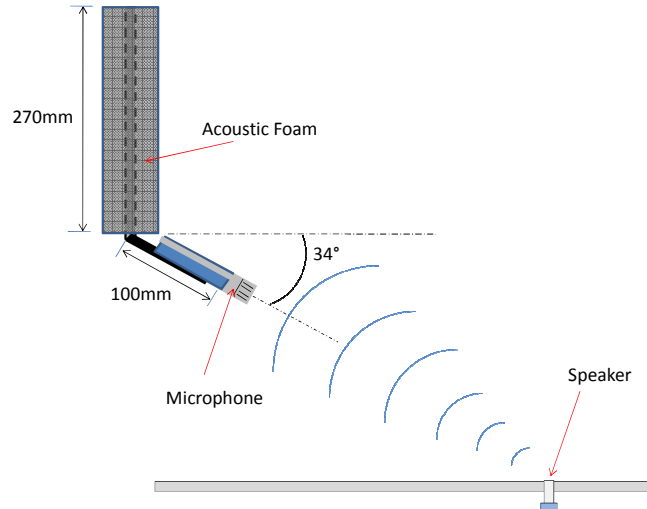
Figure 2.17 Microphone mount design and response measurement set-up (not to scale)

The microphone was placed at the same angle and position as Microphone 1 in the modified triangle formation. The resulting response function from this new formation is shown in Figure 2.18. The range was significantly reduced to within a reasonable uncertainty of the measurement, ±1dB, for frequencies above 2.5kHz, and below this, the amplitude never extends beyond 1.75dB. The decrease in amplitude of the response function suggests the majority of the uncertainty was coming from the microphone mounts themselves and not the chamber.
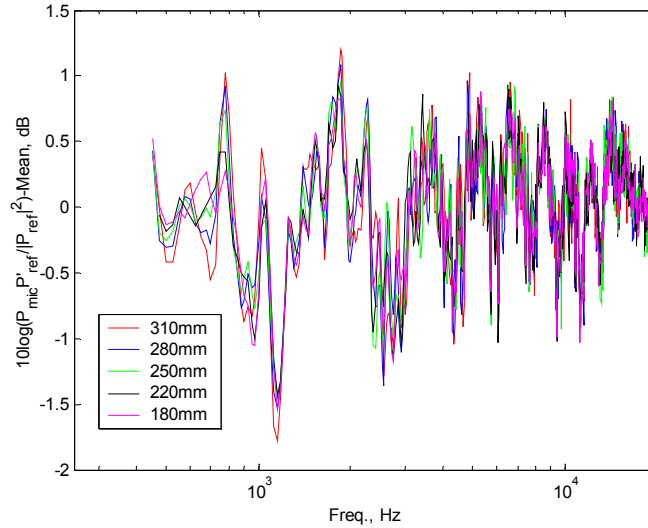
Figure 2.18 Response function for acoustically treated microphone stand varying reference microphone to source distances

To more accurately quantify the effect of the frequency decay from Figure 2.15, measurements were taken with the acoustically treated microphone mount placed at the original Microphone 1 position in the horizontally level triangle with no other far field microphones present. The result shown in Figure 2.19 displays the same decay observed in Figure 2.15, but the amplitude correction is more visually apparent because the oscillations due to the microphone mounts have been removed.
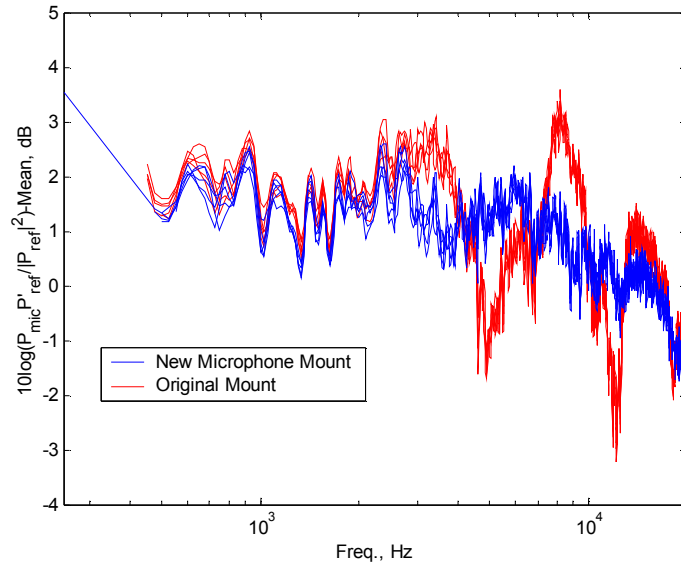
Figure 2.19 Decay effect compared to original response function

Figure 2.19 shows the high frequency, short wavelength, pressure averaging across the face of the microphone can account for a 3dB decay difference between the mean of the low frequency and the final value at 20kHz.

The acoustically reflective mounts were used in all Microphone Configuration (A) measurements and in previous studies before this response effect was discovered. Therefore, there is an uncertainty that can be estimated as ±2dB for the entire measured frequency range. All Microphone Configuration (B) measurements were taken with a new acoustically treated microphone traverse shown in Figure 2.20 that minimizes the mount and angle effects discussed above. The far field measurements taken with Microphone Configuration (B) have an uncertainty less than ±1dB.

Plate Traverse   Shelf Traverse

Shelf Traverse now attached to Plate Traverse

Acoustically treated
microphone mount
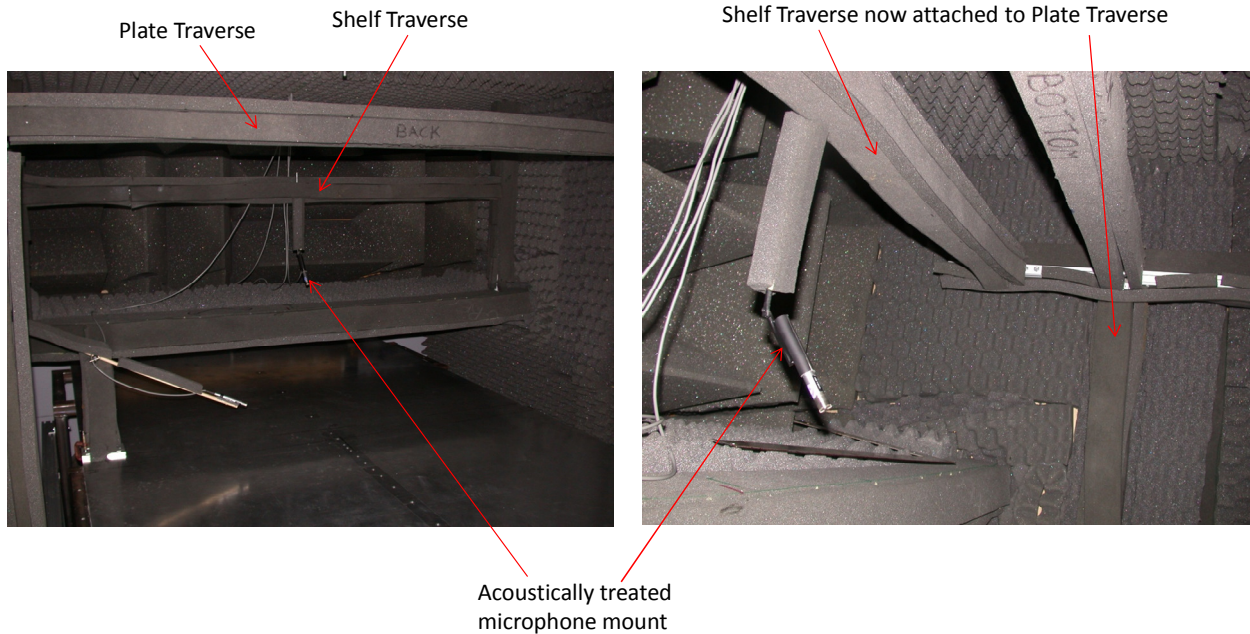
Figure 2.20 Acoustically treated microphone traverse: separated into a shelf and plate traverse (left), combined into one plate mounted traverse (right)

The redesigned microphone traverse can be configured two ways to maximize the area over which microphones can be positioned in the chamber. It can be separated forming a traverse mounted to the shelf and another attached to the legs of the plate, allowing simultaneous measurements from both ends of the chamber. The traverse can also be arranged so that the plate traverse has an arm suspended over the shelf. Hence, microphones do not have to be attached to the shelf isolating them from any unintended chamber vibrations. The traverse was covered in 25.4mm acoustic foam and microphones were positioned roughly 250mm away from the cross bars with acoustically treated microphone mounts. Figure 2.21 shows the chamber response for the new microphone traverse.
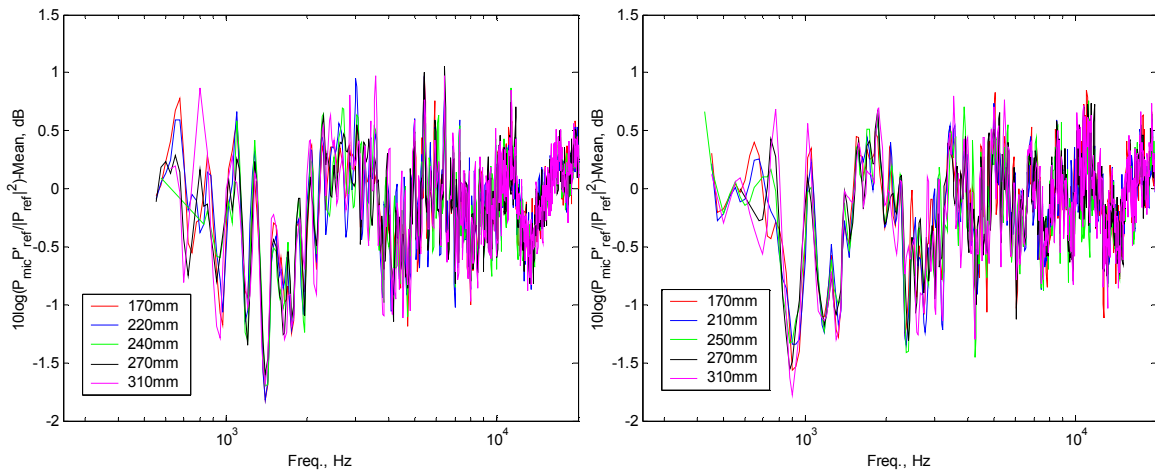
Figure 2.21 Chamber response function for new microphone traverse: with plate and shelf traverse separate (left), with plate and shelf traverse attached (right)

25

The traverse does not significantly affect the chamber response. The acoustic response function is still contained within ±1dB. Therefore, this system was used for all subsequent measurements designated as Microphone Configuration (B). There will be a noted distinction in following sections between Microphone Configuration (A), which is affected by the microphone mounts and positioning, and Microphone Configuration (B), which has been taken with the new traverse.

2.6 Roughness

Several stochastic rough surfaces were tested as well as deterministic roughness consisting of hemispherical bosses and a near-sinusoidal surface. All rough surfaces are listed in Table 2.3. The stochastic surfaces were composed of aluminum oxide Gator Grit sandpaper and Norton brand floor sanding sheets with grit sizes ranging from 220 to 20 grit. The sandpaper types will be distinguished in later sections by the labels in parentheses. Nominal manufacturer provided roughness heights are given in Table 2.3 as well as RMS roughness heights for the stochastic roughness measured by Microphotonics Inc. using white-light profilometry. Measurements of the stochastic surfaces were used to determine both the integral scale and sparseness values. The integral scale is defined as the integral of the correlation coefficient from zero displacement to the distance where the coefficient falls below 0.1. The sparseness is defined as the forward projected surface area of the roughness divided by the planar area of the roughness fetch.

Figure 2.22 shows the three dimensional results of a profilometry measurement of the 40 grit sandpaper. This image has a resolution of 15 microns. Due to the limited scan area of the profilometry measurements, the listed RMS roughness heights could be misrepresentative of the actual RMS height of the entire surface, but these measured heights seem to more accurately describe the stochastic surfaces as compared to the nominal roughness heights. The surface images are also useful in inferring surface gradients.

| Roughness Type	Nominal Height, (mm)	Measured RMS Height, (mm)	Grain Density per mm²	Sparseness, λ	Integral Scale, l_e (mm)	Sheet Backing Thickness, (mm)
20 Grit Norton Floor Sanding Sheets (20Belt)	0.95	0.207	0.23	5.27	1.253	1.27
36 Grit Norton Floor Sanding Sheets (36Belt)	0.53	0.187	1.5	2.69	0.568	1.13
40 Grit GatorGrit Sandpaper (40Grit)	0.425	0.156 to 0.133	1.4	2.13	0.547	0.76
60 Grit GatorGrit Sandpaper (60Grit)	0.265	0.106	2.6	1.08	0.266	0.58
60 Grit Norton Floor Sanding Sheets (60Belt)	0.265	0.0763	4.9	1.69	0.315	0.81
80 Grit GatorGrit Sandpaper (80Grit)	0.19	0.066	4.3	1.34	0.204	0.44
80 Grit Norton Floor Sanding Sheets (80Belt)	0.19	0.0713	6.2	1.60	0.222	0.66
100 Grit GatorGrit Sandpaper (100Grit)	0.14	0.0412	10.6	2.64	0.163	0.38
150 Grit GatorGrit Sandpaper (150Grit)	0.092	0.0287	24	2.19	0.100	0.33
180 Grit GatorGrit Sandpaper (180Grit)	0.082	0.0245	34	2.19	0.079	0.29
220 Grit GatorGrit Sandpaper (220Grit)	0.068	0.0173	43	3.90	0.103	0.29
1mm Hemispherical	1	-	0.0111	19.3	-	1.168
3mm Hemispherical	3	-	0.0037	19.3	-	1.600
LPI-20 2D Rib	0.28	-	-	4.54	-	2.17

Table 2.3 Roughness types
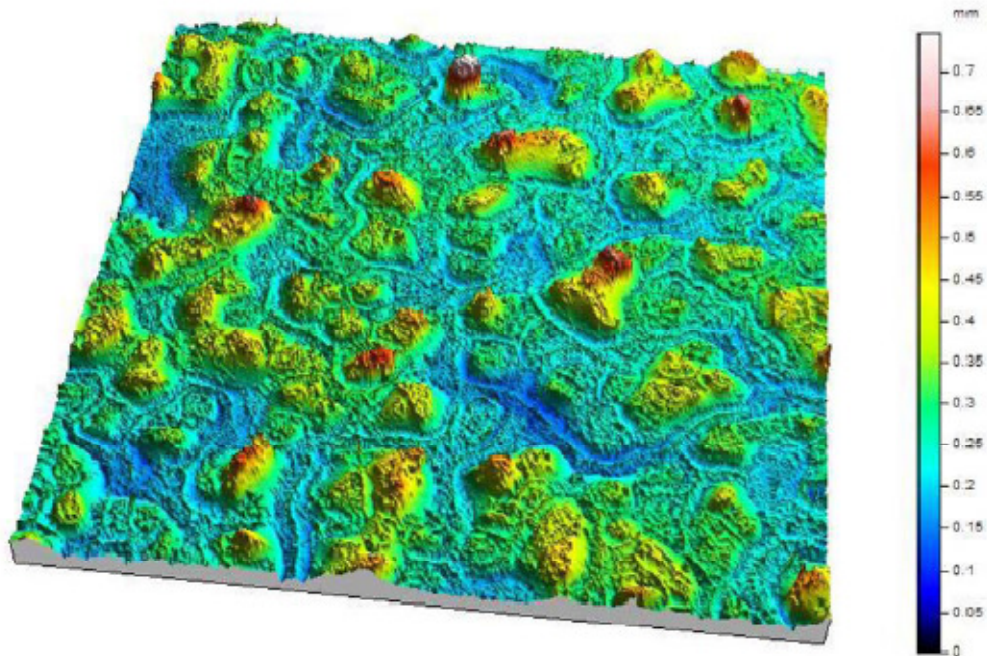
Figure 2.22 White-light profilometry measurement of 40 grit sandpaper

For all roughness measurements, 610mm by 305mm square sheets of the desired rough surface were adhered to the aluminum plate using double sided tape on the underside and foil tape of 0.1mm thickness around the perimeter of the fetch. All fetches were spanwise centered on the plate with the shorter dimension running streamwise starting at x= 1257mm from the nozzle.

The foil tape surrounding each sample created two successive two-dimensional steps: the first being the thickness of the foil tape, 0.13mm, and the second being the thickness of the sandpaper backing minus the foil tape thickness. The backing thicknesses ranged from 0.29mm for the 220 grit to 1.29mm for the 20Belt roughness. At this streamwise location with nozzle speeds ranging from 20 to 60m/s, the roughness was exposed to boundary layer velocities of 7.5 to 22m/s at the leading edge. Experiments by Grissom (2007) by way of installing the sandpaper with rough side down exposing only the smooth back side of the sandpaper showed the step discontinuity did not radiate measureable sound to the far field. A diagram of the step created by the foil tape and roughness perimeter is shown in Figure 2.23.
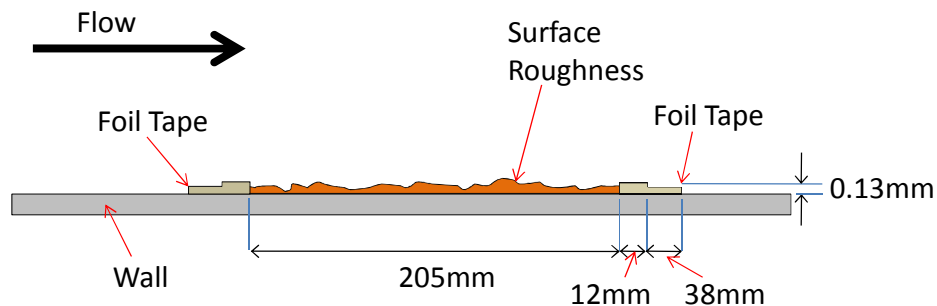
Figure 2.23 Step perimeter around roughness created by foil tape and edge of roughness

3mm and 1mm radius similarly scaled hemispherical rough surfaces were tested at the same in flow conditions as the stochastic roughness. The 3mm roughness was spaced 16.5mm spacing and the 1mm roughness was spaced 5.5mm. Because of the large spacing of the 3mm hemispherical bosses, the surface pressure microphones were mounted flush to the backing of the roughness so as not to effectively create an additional cylindrical element on the surface. The backing thickness of the deterministic rough surfaces was significantly larger than the stochastic surfaces because of the molding process. No study was done to ensure this had no effect. Therefore, data from these surfaces could be influenced by the step perimeter of the roughness causing the surface pressure and radiated far field noise to behave abnormally. Figure 2.24 shows a close-up view of the two hemispherical surfaces with a 7.3mm hole for the wall pressure microphone.

Figure 2.24 Hemispherical surfaces (right-1mm, left-3mm) with wall pressure microphone location shown

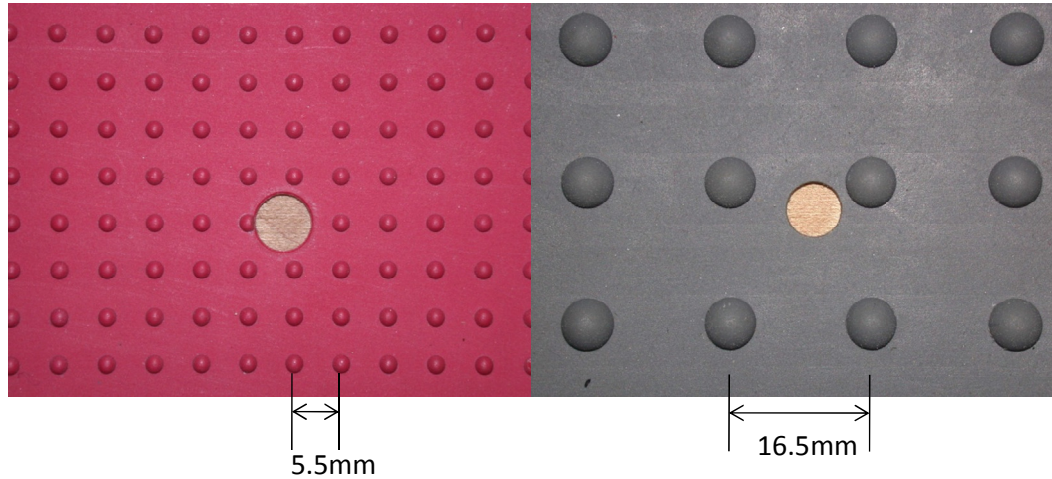The 2D rib roughness was tested with the ribs aligned perpendicular to the incoming flow. The roughness was made of LPI-20 lenticular lens that was chosen because of its profile shape which is similar to a sinusoidal wave. A cross-section of the roughness is shown in Figure 2.25.
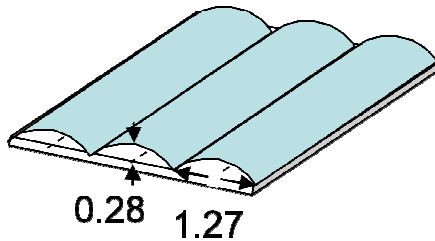
Figure 2.25 LPI-20 2D lenticular lens roughness

This roughness was used because of its near single-valued wavenumber in hopes that it would scatter only a narrow band of the wavenumber-frequency spectrum. Previous results by Grissom (2007) show that this surface produces a markedly different far field spectrum than that of the stochastic surfaces.

All roughness fetches were subject to the same smooth plate aerodynamic conditions at their leading edges located at x=1257mm. Using the relations shown in Equations 2.2, 2.3, and 2.4, Table 2.4 lists the aerodynamic properties at the leading edge of the rough fetches for the nominal nozzle exit velocities studied. For nozzle velocities from 20 to 60m/s, conditions at the roughness fetch varied from 7.51 to 21.94m/s with boundary layers 16.7 to 13.8mm thick, respectively.

U_o	δ, mm	δ*, mm	θ, mm	U_e
20	16.7	1.24	0.915	7.51
25	16	1.2	0.881	9.33
30	15.5	1.16	0.854	11.15
35	15.1	1.13	0.831	12.96
40	14.8	1.1	0.812	14.77
45	14.5	1.08	0.796	16.57
50	14.2	1.06	0.782	18.36
55	14	1.05	0.769	20.15
60	13.8	1.03	0.758	21.94

Table 2.4 Aerodynamic properties at leading edge of roughness, x=1257mm

Chapter 3 Analysis

3.1 Microphone Configuration (A)-Stochastic Surfaces

3.1.1 Far Field Noise

Using Microphone Configuration (A), measurable far field data were taken for 11 different stochastic rough surfaces that range from hydrodynamically smooth to fully rough conditions. These measurements were subject to the far field interference response problem discussed in Section 2.5. Only the results taken from the 40 grit roughness will be shown in this section to display this problem. Eight of the eleven rough surfaces were reanalyzed using Microphone Configuration (B) including the 40 grit surface. Data from the three surfaces that were not reanalyzed, 220 grit, 60Belt, and 80Belt, are shown in the Appendix at the end of the paper.

Figure 3.1 shows the far field noise from a 305x610mm patch of 40 grit sandpaper with its forward edge located at x=1257mm for 9 different jet exit speeds. The far field spectra are plotted in SPL using a $20x10^{-6}$Pa reference pressure. The roughness noise is compared to corresponding smooth plate measurements taken with no roughness present. The spectra are plotted using a 1Hz bandwidth.
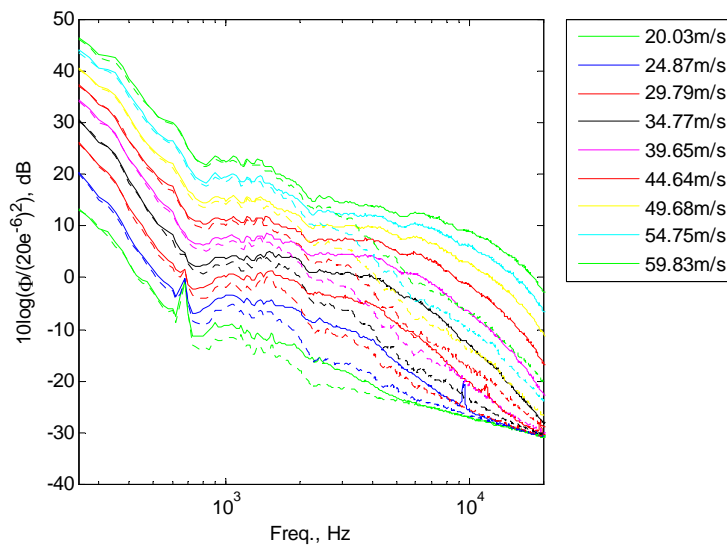

Figure 3.1 1Hz-Bandwidth far field sound from smooth surface (dashed) and from 40 grit sandpaper (solid) for varying speeds using Microphone Configuration (A)

At 60m/s, the roughness produced sound levels as much as 20dB above the background noise showing a clear increase due to the addition of roughness. For nozzle velocities 20 to 60m/s, a significant increase in noise was produced over the frequency range starting at 700Hz for the lowest speeds and extending to the measurement capability limit of 20kHz for the highest speeds.

Figure 3.2 shows the contribution of the roughness to the produced noise shown as the solid lines in Figure 3.1 calculated by subtracting the smooth wall spectra from the rough wall spectra. The data was filtered by plotting only differences of more than 1dB between the two spectra. The peak signal levels increase approximately 25dB in the nozzle velocity range considered and the peak frequency ranges from 1kHz to 5kHz. The spectra below 7kHz are subject to varying amounts of scalloping whose frequency and magnitude differ with nozzle velocity. There is a particularly large fluctuation at 5kHz for the higher

velocity measurements. The scalloping was present in all recorded far field spectra for varying roughness and produced uncertainties of ±2dB up to 6kHz and above this the uncertainty was below ±1dB. These oscillations were a source of concern that led to the development of the improved far field measurement system of Microphone Configuration (B).
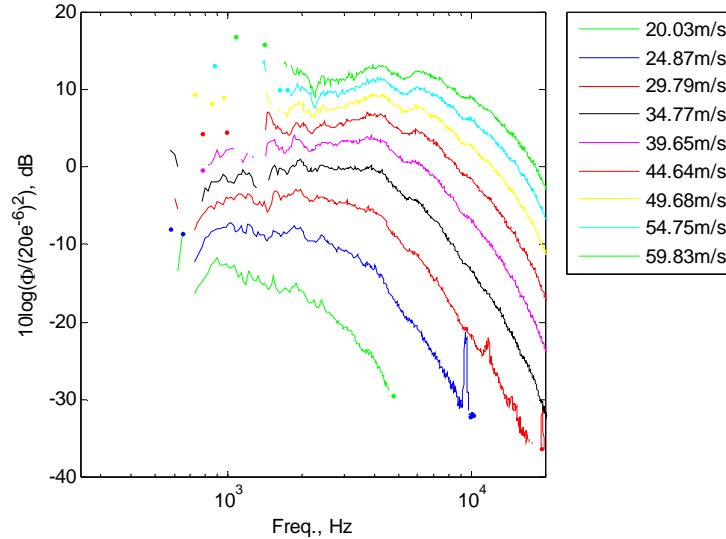

Figure 3.2 1Hz-Bandwidth 40 grit far field subtracted spectra using Microphone Configuration (A)

3.1.2 Wall Pressure

The recorded wall pressure of Microphone Configuration (A) also displayed suspicious characteristics. Just as in the previous section, results from the 40 grit fetch will be shown to present the suspect features of the recorded spectra that led to the improved Microphone Configuration (B). Figure 3.3(a) shows the recorded wall pressure spectra in the middle of a 305mm long patch of 40 grit roughness with leading edge at x=1257mm downstream of the nozzle exit for nozzle velocities 20 to 60m/s. The high frequency curl-up of each spectra is due to the measured signal reaching the noise floor of the microphone. When the calculated microphone calibration shown in Figure 2.5 is applied to the flat noise floor signal at each velocity, the resultant spectra show an increase in high frequency that is not a physical representation of the boundary layer flow. The spectra should curl-up onto the same line at high frequency, but the 30m/s curve of Figure 3.3(a) hits the noise floor at 10kHz before the expected frequency which is closer to 14kHz. The source of this discrepancy is unknown. Since this high frequency spectral rise is not a consequence of any flow process, the frequencies above the inflection point of the curl-up have been filtered and will not be shown on any successive wall pressure plot.

Figure 3.3(b) is a plot of this filtered wall pressure spectra for the 40 grit sandpaper. In Figure 3.3(b), the wall pressure spectra intensity and roll-off frequency increase with velocity as expected, but in the highest velocity measurements a lump appears around 7kHz-9kHz that is not present in the lower velocity measurements. The frequency of the lump does not seem to be significantly dependent upon velocity but grows in magnitude. The low frequency region of these measurements have a low uncertainty approximately ±1dB, but above the spectral peak of the calibration, frequencies greater than 5kHz, the uncertainty increases to ±2dB. This lump was present in the spectra for all 11 roughness cases. Therefore, the wall pressure measurement system was redesigned as well as the far field for Microphone Configuration (B).
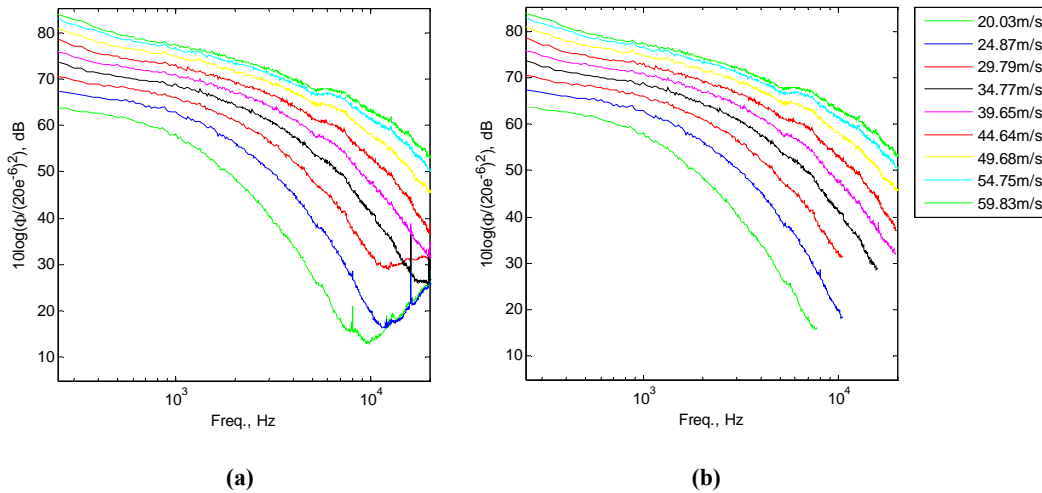
Figure 3.3 1Hz-Bandwidth wall pressure spectra for 40 grit roughness at varying nozzle velocities at x=1403mm, (a)unfiltered (b) filtered

3.2 Microphone Configuration (B)-Stochastic Surfaces

3.2.1 Far Field Noise

The results of Microphone Configuration (A) led to a reexamination of the methodology used in the data acquisition. Of particular concern was the scalloping present in far field spectra and the suspicious lumps around 7-9kHz in the near field spectra. It wasn't clear if these phenomena were caused by a physical process or if there was an error in the measurements. After analysis of the chamber response function and concerns over the use of Mylar pinholes on the surface pressure microphones, which had a tendency to detach during measurements, Microphone Configuration (B) was developed as an improved system. Using Microphone Configuration (B), only 8 of the stochastic rough surfaces listed in Table 3 of the Apparatus & Instrumentation section were studied: 20Belt, 36Belt, 40 grit, 60 grit, 80 grit, 100 grit, 150 grit, and 180 grit. The far field spectra were analyzed with the background noise subtracted, but instead of assuming the background noise was equal to the smooth plate spectra, as in Microphone Configuration (A), background spectra were taken with Mylar covering each rough surface. This preserved the step perimeter around each rough surface, but the roughness could produce no noise. This measurement was completed for each rough surface separately so that the corresponding background noise was paired with the noise from each roughness fetch. It was thought that this would help reduce scalloping in the subtracted far field spectra. Figure 3.4 shows the noise from the 20Belt Mylar covered roughness compared to the spectra recorded from the smooth plate and 20Belt surface. The Mylar covered roughness shows a consistent 2dB increase in noise above 4kHz. This is contrary to the results in Grissom *et al.* (2007), which indicated that no measurable sound is generated by the step perimeter. The discrepancy in findings could be due to the size of the step studied. In Grissom *et al.* (2007), 80 grit sandpaper was used to create the step. The 20Belt sandpaper has a step 1.27mm larger around its perimeter. Although the step noise is present, it is well below the contribution of the roughness noise and should not be considered a significant noise source. The new far field subtraction scheme should

effectively account for any noise due to these steps. The 20Belt, being the thickest stochastic roughness studied, produced the loudest observed step noise.
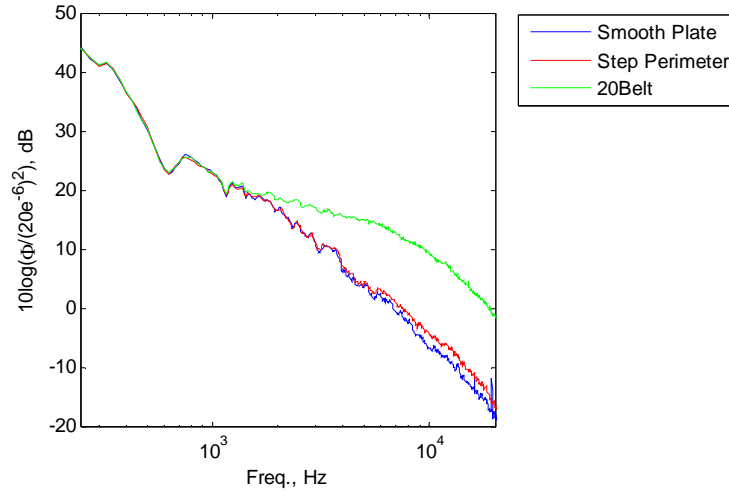

Figure 3.4 Far field noise from a smooth plate, the step perimeter around 20Belt sandpaper, and the 20Belt sandpaper surface at U_o=60m/s

The following analysis will be focused specifically on the 40 grit roughness with the results for the other seven rough surfaces plotted at the end of each section. The 40 grit roughness has a nominal roughness height of 0.425mm. The roughness Reynolds number, h^+, is approximately 14 to 39 as measured by Grissom (2007) over the considered edge velocity range 7.5 to 21.9m/s and is defined by Equation 3.1.

$$h^+ = hu_\tau/\nu \qquad\qquad \text{Eq. 3.1}$$

h is the roughness height, u_τ is the friction velocity, and ν is the kinematic velocity. The 40 grit roughness produced a sufficient signal to noise ratio over a large frequency range making it useful to define any trends. Figure 3.5 is a plot of the unsubtracted far field noise compared to the respective background noise for the 40 grit surface. At 60m/s the signal-to-noise ratio was as much as 18dB.
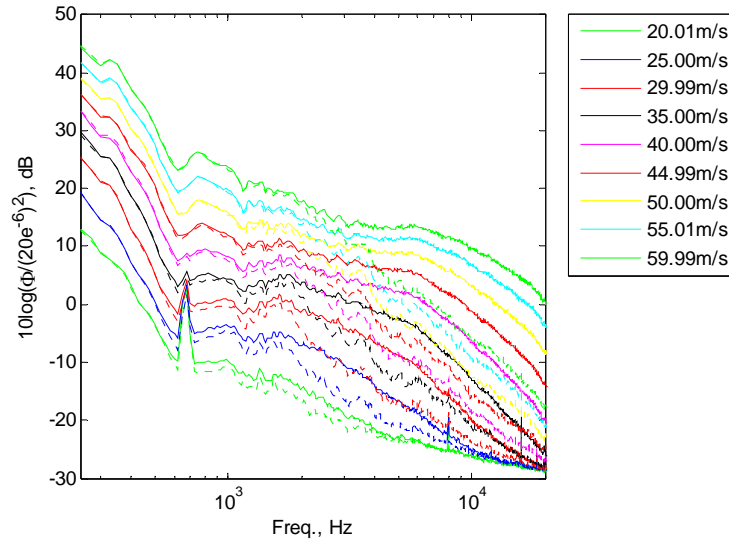
Figure 3.5 1Hz-Bandwidth far field sound from stepped surface (dashed) and from 40 grit sandpaper (dashed) for varying speeds using Microphone Configuration (B)

Figure 3.6 shows the subtracted data for the 40 grit roughness using Microphone Configuration (B). The spectral peak increases approximately 28dB over the considered velocity range and the peak frequencies increase from 1kHz to 6kHz. Subtracting the smooth wall spectra shows the same spectral shapes and pattern as observed by Grissom (2007). The frequency of the sound peak and signal strength both increase with velocity. The large fluctuations of Figure 3.2 are gone, but smaller oscillations remain, especially in lower frequencies. Only one far field microphone was used for the far field measurements of Microphone Configuration (B), and therefore, the results produce more oscillations on the fringe of the spectra due to the low signal-to-noise ratio and in lower frequencies due to the sampling scheme which averages relatively fewer of the larger wavelength pressure oscillations. The uncertainty in these subtracted measurements is ±1dB around 2kHz and decreases to ±0.25dB above 10kHz. The far field results of Microphone Configuration (A) show smoother signals at lower frequencies because the presented data is an average of four far field microphones, but the uncertainty is larger due to the spectral scalloping. Overall, the spectral shape is much better defined using Microphone Configuration (B).
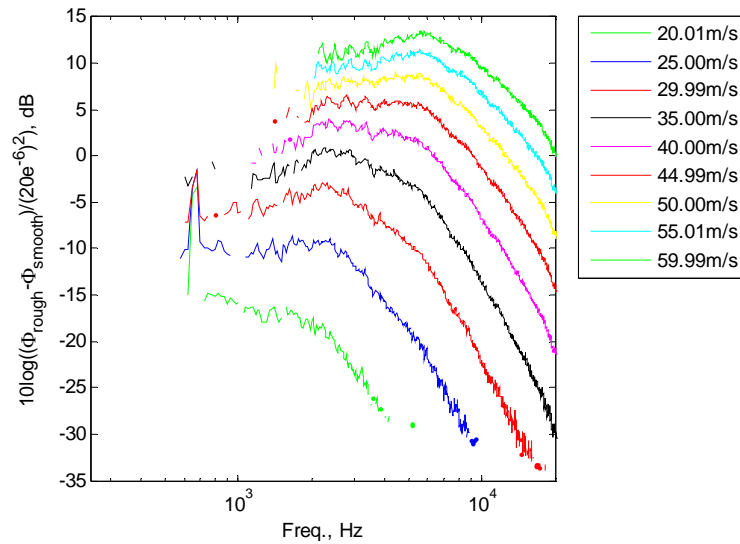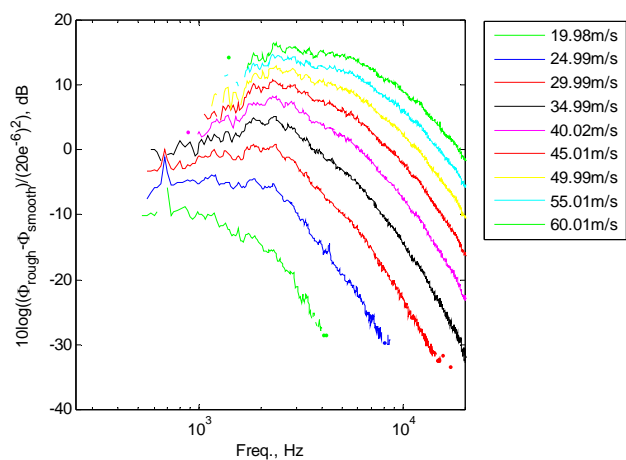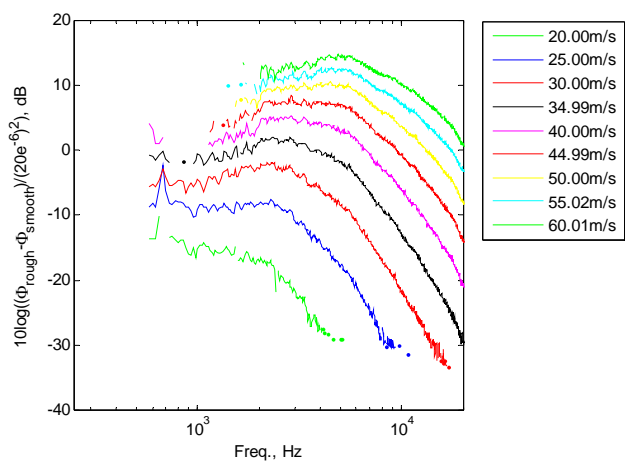
Figure 3.6 1Hz-Bandwidth 40 grit far field subtracted spectra using Microphone Configuration (B)

Figure 3.7 (a-g) shows the far field subtracted spectra of the 7 other stochastic surfaces for varying jet exit speeds. The same spectral pattern of increasing peak frequency and magnitude with velocity is shown for all rough surfaces and is more easily seen for larger roughness sizes which have greater signal-to-noise ratios. Although only at the highest frequencies, measurable far field data were taken for even the smallest roughness size, 180 grit. The noise becomes distinguishable from the background at a nozzle velocity of 49.99m/s producing a signal-to-noise ratio of 2dB. The roughness Reynolds number, h^+, at a nozzle velocity of 60m/s for this surface is approximately 5.5, on the border of hydrodynamically smooth and transitionally rough. For lower speeds this surface is hydrodynamically smooth. This indicates that the noise from this surface must be produced by scattering of the boundary layer wall pressure fluctuations since hydrodynamically smooth surfaces produce no aerodynamic interaction by definition.

(a)

(b)
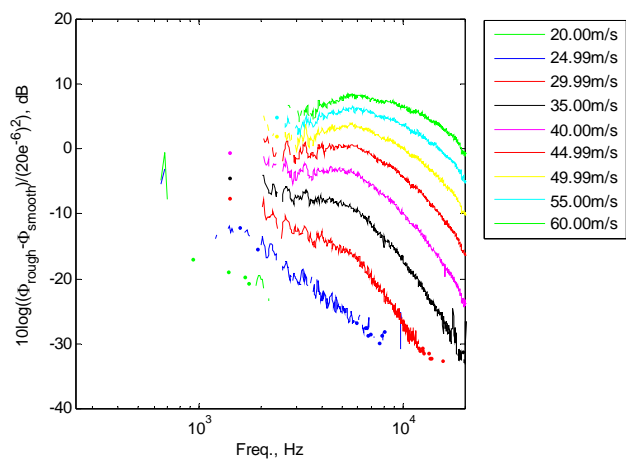
(c)

(d)

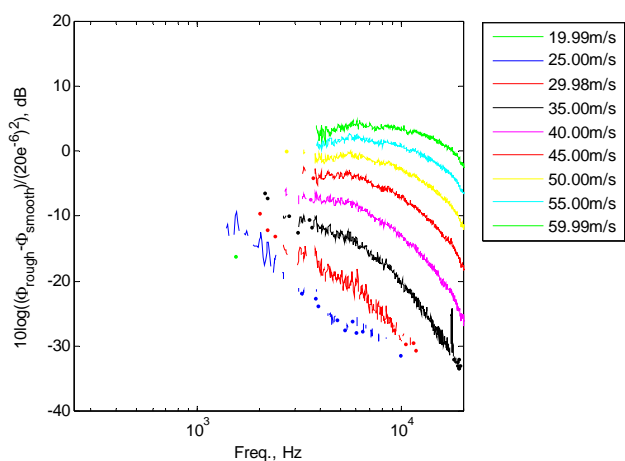**Figure 3.7 1Hz-Bandwidth subtracted far field for (a)20Belt, (b)36Belt, (c)60 grit, (d)80 grit, (e)100 grit, (f)150 grit, and (g)180 grit**
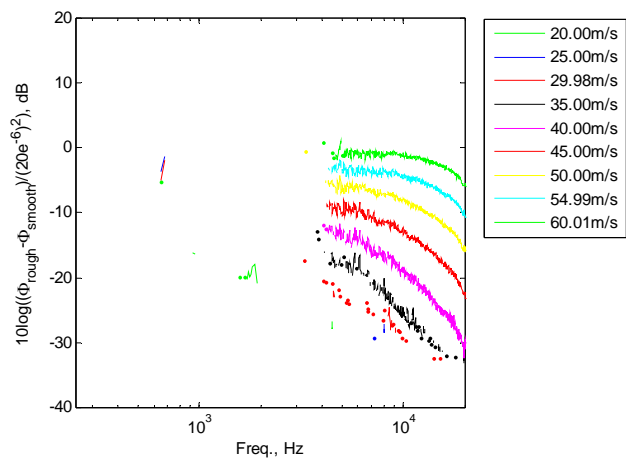
(e)

(f)

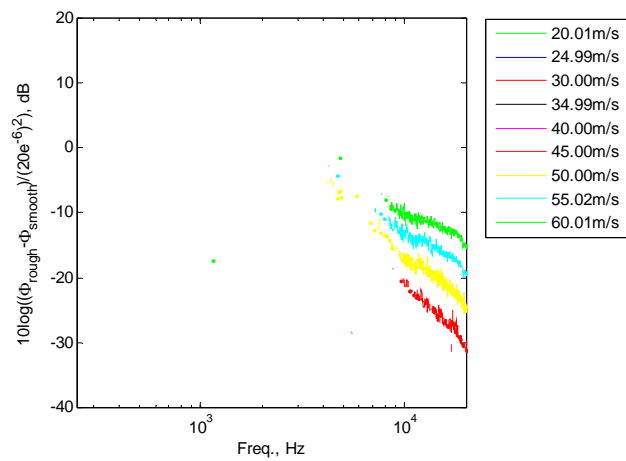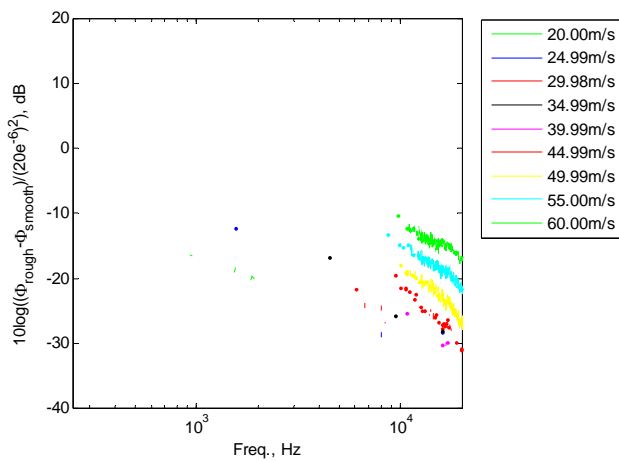
(g)

Figure 3.7 1Hz-Bandwidth subtracted far field for (a)20Belt, (b)36Belt, (c)60 grit, (d)80 grit, (e)100 grit, (f)150 grit, and (g)180 grit. (Cont'd)

3.2.2 Wall Pressure

The effect of the wall pressure microphone height was studied for a location at the center of a 40 grit roughness fetch 305x610mm at U_o=60m/s. Figure 3.8 shows the wall pressure spectra for varying microphone positions ranging from nearly 40% of the nominal grain height below the bottoms of the roughness to the roughness tops. The roughness height is denoted as *h* and the microphone position is measured from the base of the roughness grains. The low frequency up to 6kHz was unaffected by microphone heights above the roughness substrate. The two lowest heights, -0.08*h* and -0.37*h*, produced increased levels at these low frequencies. The -0.08*h* data increased up to 3dB over the other spectra. This could be due to the microphone top being very near the plane of the roughness substrate. For frequencies above 6kHz, the spectral levels generally increase with microphone height until the microphone is above the roughness substrate. The spectra of the 0.58*h* and 1.00*h* positions lay 1dB above the other spectra for positions above the roughness substrate. This is within the uncertainty range of the measurement when repositioning the microphones so no certain conclusions are drawn. From the results, it seems that the for the microphone height range 0.40*h* to 1.00*h*, there are no significant differences in spectra. This is consistent with the results of Smith (2008) that showed no difference in recorded spectra above the mid-height of the roughness. For consistency, the same microphone heights used in Microphone Configuration (A) were used to record the wall pressure using Microphone Configuration (B). This corresponds to the 0.58*h* curve in Figure 3.8 for the 40 grit roughness. The nominal microphone heights for the other rough surfaces were consistently above the mid-height of the rough surfaces. The measured standard deviation from the desired microphone height was approximately ±0.1mm taken from a sample of 18 wall pressure microphone installations. This is a significant error when compared to the nominal 180 grit roughness height, 0.082mm. Although, Figure 3.8 shows that for high frequencies where the majority of the roughness noise is observed for these smaller rough surfaces the spectral shape is unchanged by microphone height. Only the observed absolute levels seem to be affected.
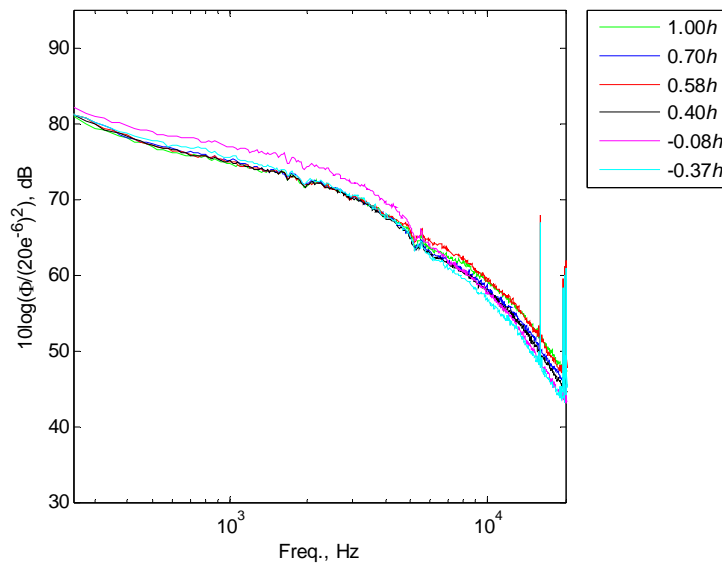

Figure 3.8 Varying wall pressure microphone height 152mm into a 40 grit fetch at U_{noxxle}=60m/s

The wall pressure was measured at three locations inside the 40 grit roughness fetch. Figure 3.9 is a plot of the wall pressure at these three positions for U_o=30m/s, 45m/s and 60m/s. The roughness fetch began at x=1257mm and the microphones were located at x=1353, 1403, and 1505mm. The spectra decay with streamwise position but the relative decay between positions changes with velocity. The spectra display a slight relative rise between 1353mm and 1505mm approximately 1dB in frequencies above the knee as the measurement velocity increases. There seems to be more high frequency energy at the front of the fetch that increases with velocity relative to downstream locations. There is little variance between the forward two measurements, which are only separated by 50mm compared to the following microphone located another 102mm further downstream of the central microphone.
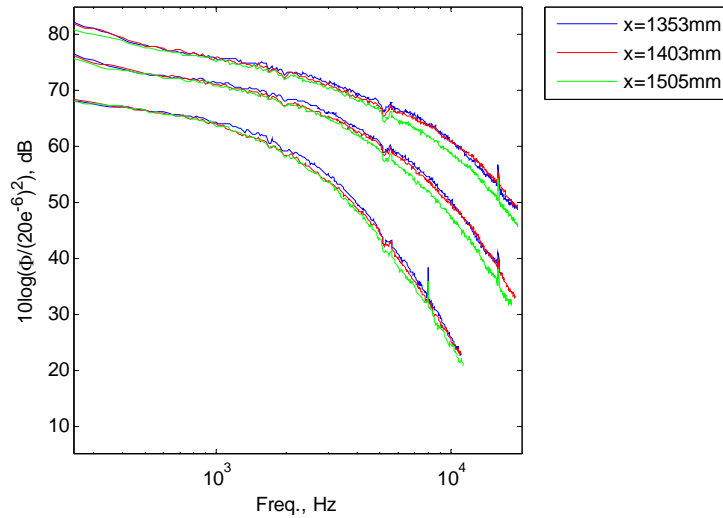

Figure 3.9 Wall Pressure for three different streamwise positions in 40 grit sandpaper at 30m/s, 45m/s, 60m/s

Figure 3.10 shows the wall pressure measured in the central position, x=1403mm, of a 40 grit fetch. The quality of the wall pressure measurements were greatly increased with Microphone Configuration (B). Compared to Figure 3.3(b), the spectra in Figure 3.10 are much smoother without the suspect lump at 7kHz-9kHz. The overall spectral levels and shapes remain the same. The wall pressure spectra generally behave as a conventional turbulent boundary layer as predicted by Blake (1986). The low frequency spectra decay at approximately ω^{-1} due to turbulence fluctuations in the logarithmic region of the boundary layer and the high frequency roll-off is roughly ω^{-5}. In the lowest velocity cases, the slope actually slightly exceeds the ω^{-5} in the high frequency regions. The higher velocity spectra may also exceed the ω^{-5} but the limit of the measurement is reached before the spectra progress far enough. This deviation could be partly due to the greater uncertainty of the calibration and measurements above 5kHz. The pinhole modification lessens the sensitivity at these higher frequencies and the calibration procedure is more sensitive to wavelength interference as the scale becomes smaller. The uncertainty of these wall pressure measurements are ±1dB up to 5kHz and ±2dB for higher frequencies. This does not include any adverse affects the pinhole modification has on the measured wall pressure spectrum.
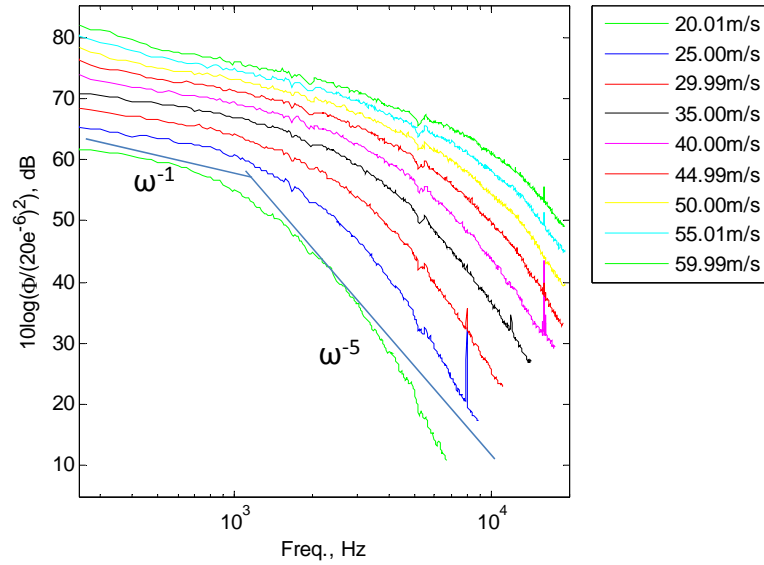
Figure 3.10 1Hz-Bandwidth wall pressure spectra for center of 40 grit fetch at varying nozzle speeds

Figure 3.11 shows a comparison of the smooth wall and 40 grit pressure spectra for 30, 45, and 60m/s nozzle velocities measured at the same downstream location, x=1403mm. The rough wall pressure fluctuations increase for all observed frequencies. The largest relative increases occur at frequencies just before the knee of the curves. The relative increases in pressure fluctuation intensities increases with speed. At 30m/s the spectrum increases by up to 4dB from the smooth plate measurement. At 60m/s the spectrum increases as much as 6dB.

Figure 3.11 40 grit wall pressure spectra compared to smooth plate wall pressure spectra

Wall pressure measurements were made at the x=1403mm position for the remaining 7 studied stochastic surfaces. Figure 3.12 shows a comparison of these measurements for varying roughness size at a nozzle exit velocity of 60m/s. The largest spectral increases occur before the knee of the curve at

41

frequencies 400Hz-8kHz. The intensity generally rises with roughness size. The only exception is for the 150 grit sandpaper whose spectrum cuts through the middle of the results showing levels more similar to the 40 grit roughness. From the 180 grit to 20Belt spectra, the intensities increase by as much as 7dB.
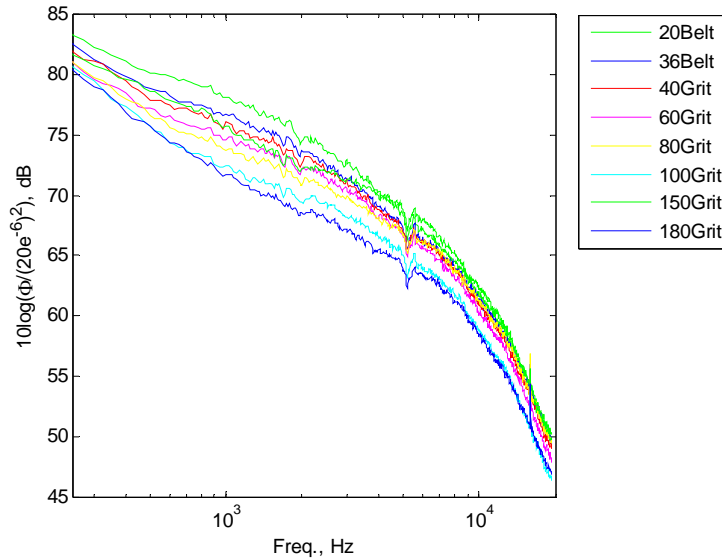
Figure 3.12 Wall pressure measurements for varying roughness size at a nozzle exit velocity of 60m/s
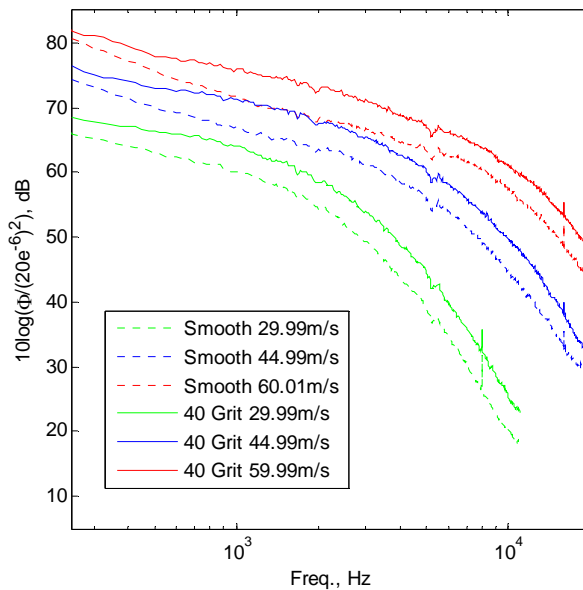
Figure 3.13 (a-g) show the remaining wall pressure results for the 7 stochastic rough surfaces with varying nozzle exit velocities. The spectra all have similar shapes and do not show any dramatic differences in absolute levels. There are only slight variations in spectral shape at higher velocities for varying roughness size. The smaller roughness heights produce a stronger defined bend where the intensity of the fluctuations begin to dissipate, around 8kHz for the 60m/s case. The larger roughness heights show a much more gradual shift in slope as the frequency increases. This could be an effect of increases in lower frequency pressure fluctuations generated by the larger element sizes. Raising the relative levels of the low frequency fluctuations would have a smoothing effect on the general shape of the spectra. Figure 3.12 displays exactly this effect. The 20Belt spectrum displays a larger relative increase in fluctuations below the knee which smooth the effect of the turn.
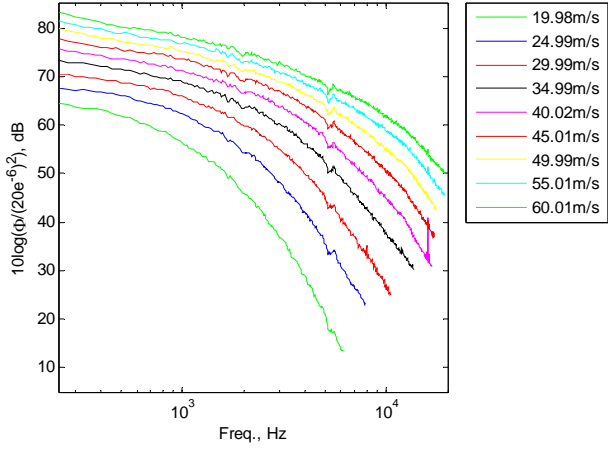
(a)
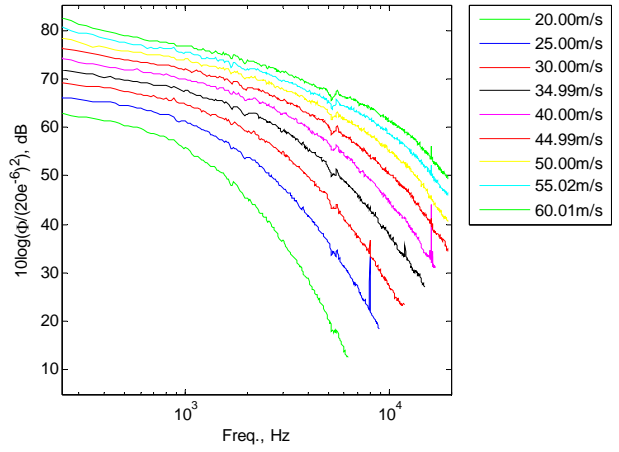
(b)
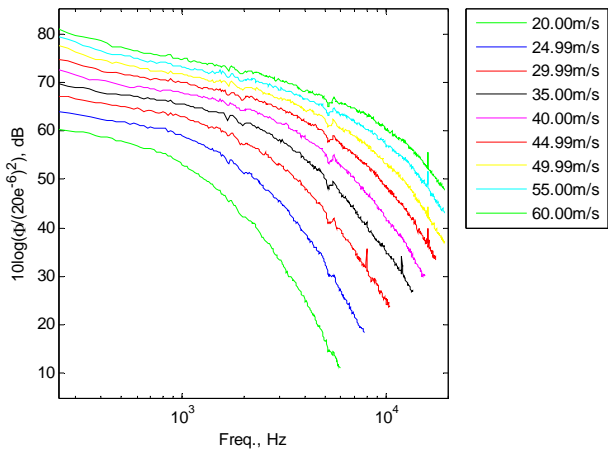
(c)
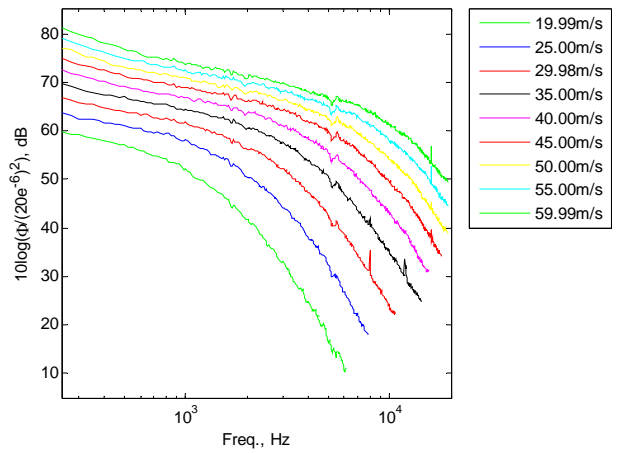
(d)

Figure 3.13 1Hz-Bandwidth wall pressure spectra for (a)20Belt, (b)36Belt, (c)60 grit, (d)80 grit, (e)100 grit, (f)150 grit, and (g)180 grit
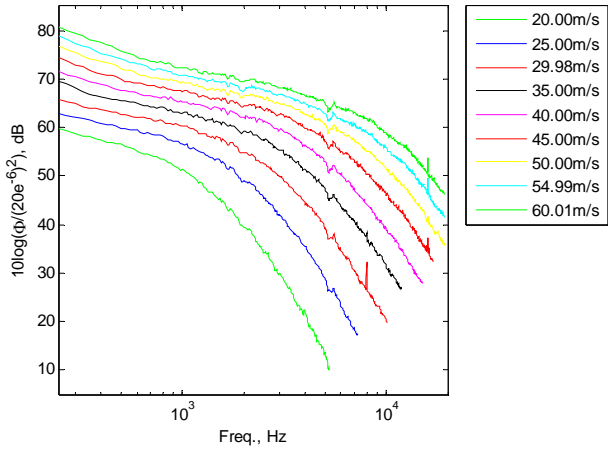
(e)
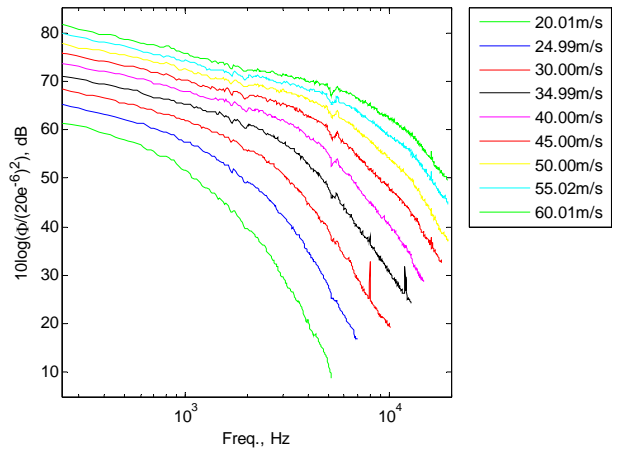
(f)
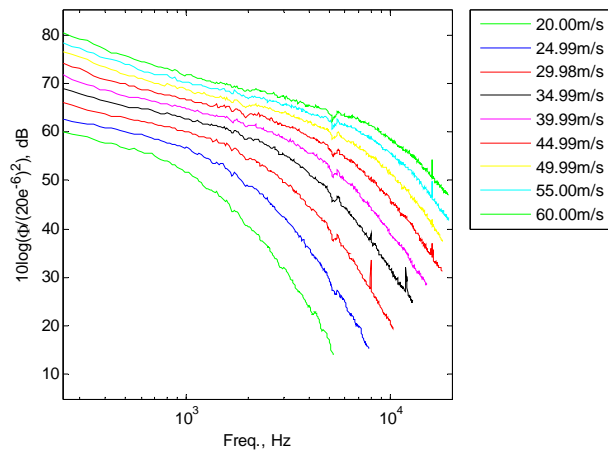
(g)

Figure 3.13 1Hz-Bandwidth wall pressure spectra for (a)20Belt, (b)36Belt, (c)60 grit, (d)80 grit, (e)100 grit, (f)150 grit, and (g)180 grit (Cont'd)

3.3 Velocity Normalization of Far Field Sound from Stochastic Surfaces

3.3.1 Inner and Outer Variable Normalizations

Using the data taken with the improved measurement techniques of Microphone Configuration (B), the normalizations suggested by Cole (1980), Howe (1988), Glegg *et al.* (2007), and Farabee & Geib (1991) were applied to radiated noise from the 40 grit fetch for varying velocities. These scalings are shown again in Table 3.1.

| Author (Year), Source Type	Suggested Scalings
Cole (1980), Dipole	$\dfrac{\Phi_{pp}(\omega)}{(\rho/c_\infty)^2 U^5 \delta *} \sim f\left(\dfrac{\omega\delta *}{U}\right)$
Cole (1980), Quadrupole	$\dfrac{\Phi_{pp}(\omega)}{(\rho/c_\infty{}^2)^2 U^7 \delta *} \sim f\left(\dfrac{\omega\delta *}{U}\right)$
Howe (1988), Dipole	$\dfrac{\Phi_{pp}(\omega)}{(\rho/c_\infty)^2 u_\tau^5 h} \sim f\left(\dfrac{\omega h}{u_\tau}\right)$
Farabee & Geib (1991), Dipole	$\dfrac{\Phi_{pp}(\omega)}{(\rho/c_\infty)^2 u_\tau^4 U\delta *} \sim f\left(\dfrac{\omega\delta *}{U}\right)$
Glegg *et al.* (2007), Dipole	$\dfrac{\Phi_{pp}(\omega)}{(\rho/c_\infty)^2 u_\tau^4 U(h^2/l_e)} \sim f\left(\dfrac{\omega l_e}{U}\right)$

Table 3.1 Proposed inner and outer variable scalings

The results of the 40 grit normalizations are shown in Figures 3.14 (a-e). Figures 3.14 (a) and (b) show Cole's (1980) dipole and quadrupole scaling, respectively. The boundary layer characteristics for this scaling were estimated from the relationships in Equations 2.2, 2.3 and 2.4 for smooth plate conditions at the leading edge of each fetch. With this assumption, the quadrupole scaling collapsed the data better than the dipole theory for the entire frequency range but performed exceptionally well above $\omega\delta*/U_e=2$ collapsing the data within 2dB. The dipole normalization begins to pinch together at frequencies below $\omega\delta*/U_e=1$, but without more data in that range, the extent of a collapse cannot be determined. The dipole theory normalizes the highest velocities more efficiently than the slowest three cases which fall below the normalized curve. Cole's quadrupole theory seems to have the opposite effect apparent in lower frequencies. The slowest velocities normalize to one curve while the three fastest velocities fall under the curve below $\omega\delta*/U_e=2$. For both theories, the estimated displacement thickness and edge velocity collapse the spectral peaks well.

The leading edge assumption does not explain the collapse or lack of collapse for Cole's (1980) scalings in Figure 3.14 (a-b). The roughness height was shown not to affect the edge velocity, U_e, in

Grissom *et al.* (2007) so the most significant error lies in the estimation of the displacement thickness. Focusing on the 30 and 60m/s cases of Figure 3.14 (a), there is an approximately 3dB difference between the two spectra's normalized peak values. Therefore, the current ratio of the assumed displacement thicknesses for the 30 and 60m/s cases would have to be halved for the magnitude of the spectral peaks to collapse. The leading edge estimations of displacement thickness are 1.15 and 1.02mm for the 30 and 60m/s cases, respectively. The measured displacement thicknesses from Grissom *et al.* (2007) for the 40 grit 30 and 60m/s cases are 2.55 and 2.89mm, respectively. The increased displacement thickness size would only collapse the data by an additional 1dB. Therefore, the leading edge estimations seem to be a fair approximation of the normalized levels.

Figure 3.14 (c) shows the subtracted data collapsed using Howe's (1988) dipole normalization. The measured RMS height is used as the normalizing lengthscale and the friction velocity was determined using the results of Bradshaw & Gee (1960) for skin friction of a turbulent wall jet over a smooth plate shown in Equation 3.2.

$$C_f = 0.0315 Re_\delta^{-0.182}$$ Eq. 3.2

The friction velocity was calculated from the skin friction coefficient using the relation in Equation 3.3 at a position x=1353mm.

$$u_\tau = U_e \sqrt{C_f/2}$$ Eq. 3.3

The result of Howe's normalization is similar to Cole's dipole method in Figure 3.14 (a). The spectra start to collapse at the lowest frequencies, but there is not enough data below a non-dimensional frequency of 3 to make a definitive statement. Overall, there is poor collapse for the entire frequency range with the data spread approximately 11dB in order of velocity from 20 to 60m/s. A similar high velocity collapse appears but not to the same extent as Cole's dipole results. For Howe's scaling only the three highest velocity curves fall on a similar line.

Again, the difference in normalized spectra cannot be attributed solely to the smooth plate assumption in Equation 3.2. To achieve a collapse of the spectral peaks the ratio of friction velocities, 60 by 30m/s case, would have to increase by 20% from the estimated smooth plate values. The estimated smooth plate friction velocities were 0.58 and 1.08m/s for 30 and 60m/s nozzle velocities, respectively. The measured friction velocities from Grissom *et al.* (2007) for 40 grit roughness at 30 and 60m/s were 0.70 and 1.44m/s. These values were obtained through a momentum balance approach. This difference collapses the data 2.2dB further. This is a significant difference but the two spectra would still range 1.8dB.

Figure 3.14 (d) and (e) show the Glegg *et al.* (2007) and Farabee & Geib (1991) dipole normalizations also employing smooth plate estimations as calculated for the Cole (1980) and Howe (1988) methods. Glegg introduces the roughness correlation length into his theory while Farabee & Geib (1991) use the displacement thickness for their scaling length similar to Cole (1980). Both theories produce limited success with results comparable to Howe's (1988) normalization collapsing the higher frequencies only within 10dB. Again, the highest velocities produce a better collapse, but the lowest speeds fall significantly below the curve for both normalizations.

Completing another analysis with measured data shows that the possible error associated with the smooth wall approximation is only a small contributor to the poor collapse of each theory. The friction velocity ratio of the 60 by 30m/s cases needs to increase by 26% from the smooth wall estimation to

collapse the 4dB difference in Figure 3.14(d). The ratio of the measured values of friction velocity at 30 and 60m/s for the 40 grit case increase by 10% and only account for 1.7dB of the spread.

The Farabee & Geib (1991) normalization shown in Figure 3.14(e) is affected by the smooth plate estimation of both the friction velocity and displacement thickness. Focusing on the 30 and 60m/s spectra, the spectral peaks are separated by approximately 4dB. To collapse this difference, the ratio $\frac{u_{\tau_{60}}^4 \delta_{60}^*}{u_{\tau_{30}}^4 \delta_{30}^*}$ must increase by a factor of 2.5 from the smooth plate estimation. The smooth plate values give a ratio of 11.0. Using the values from Grissom *et al.* (2007) as before, this ratio is 20.3, only 1.8 times the smooth plate estimation and collapses the data by a further 2.6dB. This still leaves a 1.4dB difference between the 30 and 60m/s normalized spectra, a significant improvement but not a total collapse.
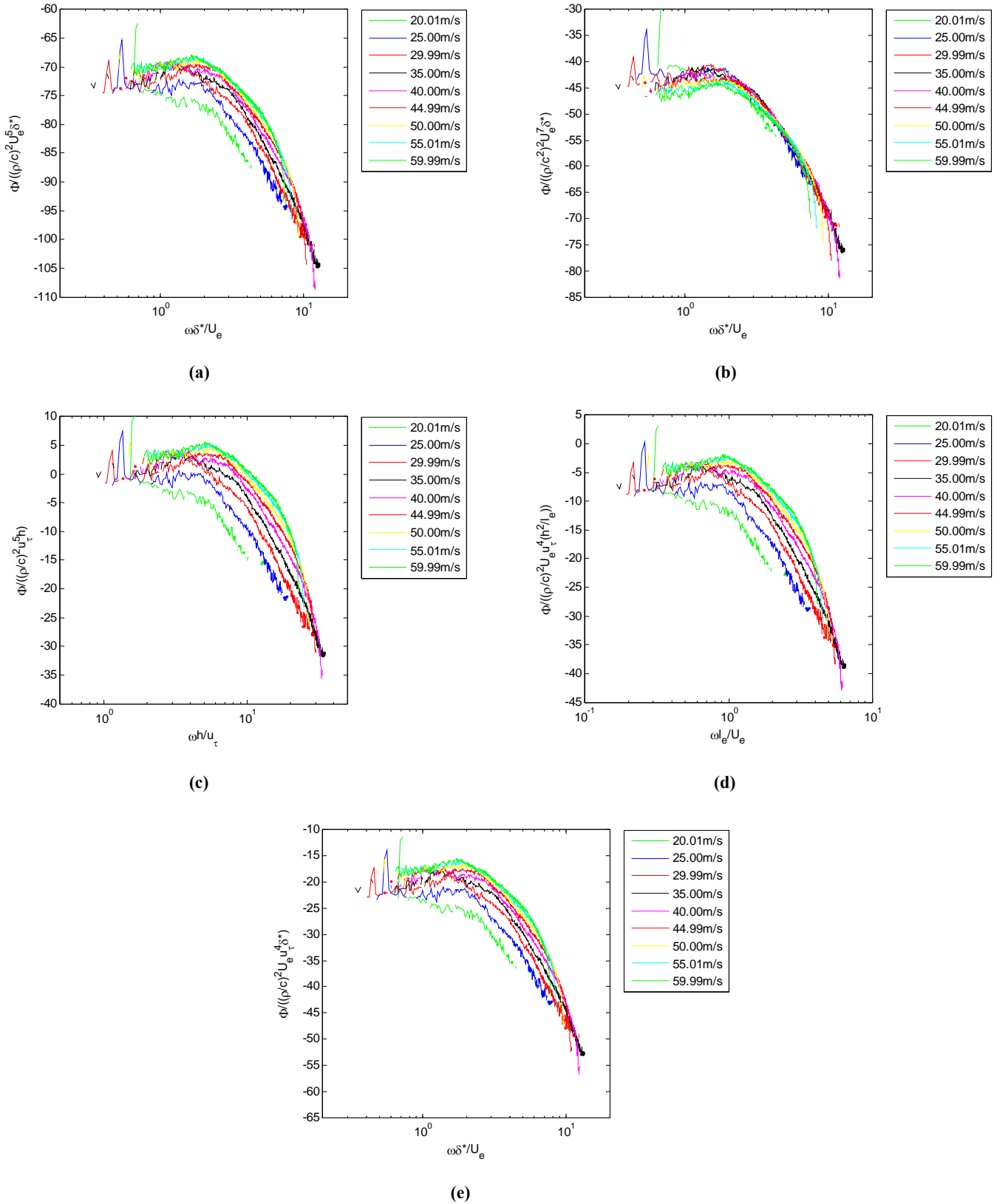
Figure 3.14 Normalized far field noise from 40 grit roughness using (a) Cole (1980) dipole (b) Cole (1980) quadrupole (c) Howe (1988) (d) Glegg *et al.* (2007) and (e) Farabee & Geib (1991) normalizations

The results of the Cole (1980), Howe (1988), Glegg *et al.* (2007), and Farabee & Geib (1991) scalings agree with the conclusions in Grissom (2007), which details the effectiveness of each normalization. None of the suggested scalings can collapse the entire frequency range for all of the studied velocities. The uncertainties in the measured u_τ and δ* values are 8% and ±0.25mm, respectively. The uncertainty in u_τ was obtained through a jitter analysis. These values create an uncertainty of less than ±0.1dB in the discussed collapse of the 30 and 60m/s cases for all considered scalings. Therefore, uncertainty in the measured quantities makes no significant difference in the results.

All of the dipole models have problems collapsing the lower velocity measurements and produce better results as the velocities increase. The relative success of the Cole (1980) quadrupole model is surprising but is in general a poor indicator of the physical process creating the roughness noise. The displacement thickness will not be able to scale noise from multiple elements properly, as will be shown later. Essentially, this model has only one operative scaling variable, velocity.

3.3.2 Normalization on Wall Pressure

The conclusions of Section 3.3.1 confirm the results of Grissom (2007) and add only an endorsement of his findings to the development of roughness noise theory. The significant addition of this study is the analysis of a new normalization theory developed by Glegg & Devenport (2009) that relates the radiated noise to the wall pressure spectrum. Their theory is derived from Lighthill's Acoustic Analogy (1952) ignoring any contribution from quadrupole sources. This is a valid simplification since in low Mach number flows dipole sources dominate quadrupole source intensities and the roughness noise source model is typically dipole. They also assume the boundary layer thickness is small relative to the acoustic wavelength. The result of their theory is shown in Equation 3.4.

$$\Phi_{pp}(\boldsymbol{x},\omega) = \frac{4\pi^2(k_o h)^2 \Sigma \Phi_{PP}(\omega)}{|\boldsymbol{x}|^2} \int \Psi_{PP}(\kappa_1, \kappa_3, \omega) \Gamma(\kappa_1, \kappa_3, k_o) d\kappa_1 d\kappa_3 \qquad \text{Eq. 3.4}$$

$\Phi_{pp}(\boldsymbol{x},\omega)$ is the radiated far field pressure, $\boldsymbol{x}$ is the observer position, Σ is the planar area of the rough fetch, $\Phi_{PP}(\omega)$ is the single point wall pressure spectrum, $\Psi_{PP}(\kappa_1, \kappa_3, \omega)$ is the wavenumber-frequency spectrum normalized on the single point wall pressure spectrum, and $\Gamma(\kappa_1, \kappa_3, k_o)$ is a wavenumber filter defined by the surface wavenumber and gradient.

They proceed to solve their new "Unified Theory" for a random distribution of roughness elements with vertical sides assuming the wall pressure is homogeneous over the rough surface. This is exactly the case encountered with the stochastic roughness used in this study. Equation 3.5 shows the result of their simplification.

$$\Phi_{pp}(\boldsymbol{x},\omega) \approx C \left(\frac{x_1}{|\boldsymbol{x}|}\right)^2 \frac{(k_o h)^2 \Sigma \Phi_{PP}(\omega)}{|\boldsymbol{x}|^2} \qquad \text{Eq. 3.5}$$

Here $\boldsymbol{x}$ is the observer position, C is a constant for all geometrically similar surfaces, k_o is the acoustic wavenumber, h is the roughness height , and $\Phi_{PP}(\omega)$ is the single point wall pressure spectrum. For a fixed roughness and observer position, the far field noise is only a function of the surface pressure spectrum and the acoustic wavenumber. According to Equation 3.5, the far field noise is directly proportional to the wall pressure spectrum.

Figure 3.15 (a-b) is a plot of the far field noise and wall pressure spectra of the 40 grit roughness comparing the relative increases in spectra at the same frequencies. The difference between any two

points at a fixed frequency on the subtracted far field spectra exactly match the difference in the near field pressures. Highlighted in Figure 3.15 (a-b), the U_o= 20.01m/s and 59.99m/s spectra have a difference of 34dB at 3kHz and the U_o= 40.00m/s and 55.01m/s spectra have a difference of 14dB at 10kHz. This agrees with the result of Equation 3.5 that the far field is directly proportional to the near field wall pressure spectra.
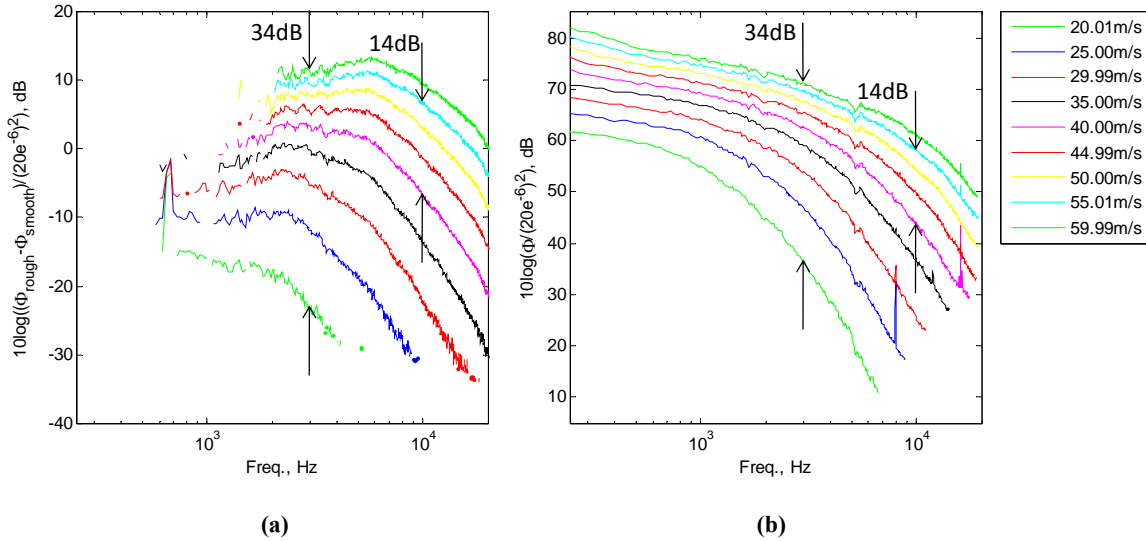

Figure 3.15 (a) Far field and (b) near field comparison for 40 grit rough fetch at varying nozzle velocities

According to Equation 3.5 for a fixed observer location and roughness type, if the subtracted far field noise is divided by the wall pressure spectra, the resultant noise should only be a function of the acoustic wavenumber squared. Figure 3.16 shows this normalization for the 40 grit surface using the surface pressure microphone located at x=1403mm. The spectra collapse well up to 5.2kHz and then the spectra begin to fan out in order of velocity. The slowest velocities rise above the rest and unfold down to the fastest. For frequencies up until this deviation, the spectra collapse within 2dB, a significant improvement from the previously proposed dipole scalings. The point of deviation at 5.2kHz coincides with the peak frequency of the wall pressure microphone calibration. Above 5.2kHz, the microphone experiences a steep loss of sensitivity with frequency. The normalized spectra of Figure 3.16, although separating at 5.2kHz, still all seem to follow an ω^2 trajectory. Therefore, this fanning occurrence may be due to the wall pressure microphone's loss of sensitivity at high frequency or error in the calibration technique and not due to any physical process. The modified 1/4mm pinhole microphones may be capturing relatively less of the pressure intensity at low velocities. The low velocity curves would then rise above the others when normalized. Of course, this explanation is only speculation with no data confirming it. Further research needs to be conducted on the wall pressure measurement and calibration techniques for these pinhole modifications to determine any adverse effects on the results.
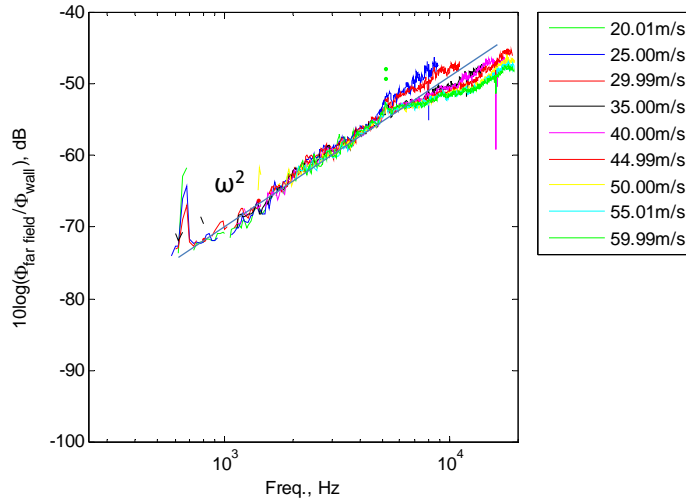
Figure 3.16 Normalized 40 grit spectra using Microphone Configuration (B)

The far field results from the other 7 rough surfaces were normalized the same way, dividing by the single point wall pressure recorded at x=1403mm. The results are shown in Figure 3.17(a-g). The far field noise produced by the surfaces collapse well, but all of the figures show the same fanning in high frequency that corresponds to velocity. For each curve the velocity fanning begins at the same frequency suggesting that the wall pressure measurement is indeed the source of the trend. Also, curve fitting the entire observable frequency range for each rough surface reveals that the slopes may deviate from the theoretical ω^2 curve as the roughness size is increased or decreased to its extremes. The slope seems to behave inversely to the roughness height. The normalization for the largest grit size, 20Belt, has a slope of approximately $\omega^{1.6}$. The normalization for the smallest grit size, 180 grit, has a slope of approximately $\omega^{3.5}$. This could be a misleading result, though. Ignoring data above 5.2kHz, where the suspect fanning occurrence begins, the data follows the ω^2 curve well.

Figure 3.17 Glegg & Devenport (2009) normalization for (a)20Belt, (b)36Belt, (c)60 grit, (d)80 grit, (e)100 grit, (f)150 grit, and (g)180 grit.

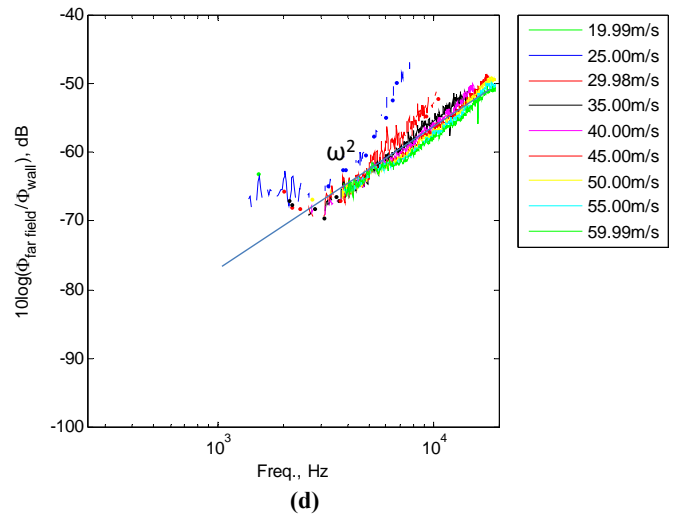**(e)**   **(f)**
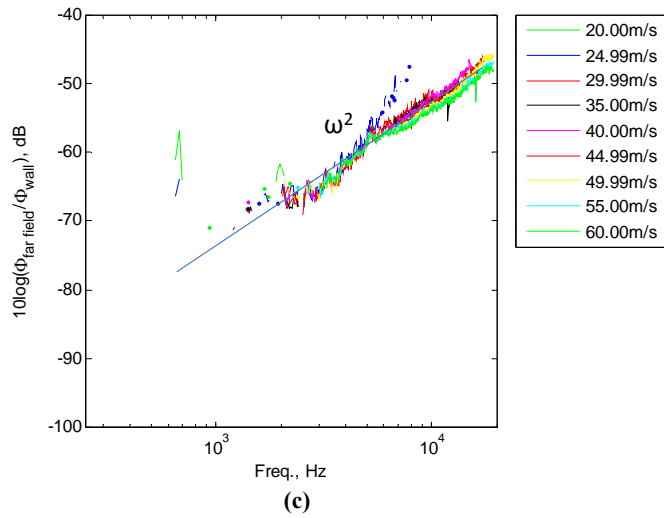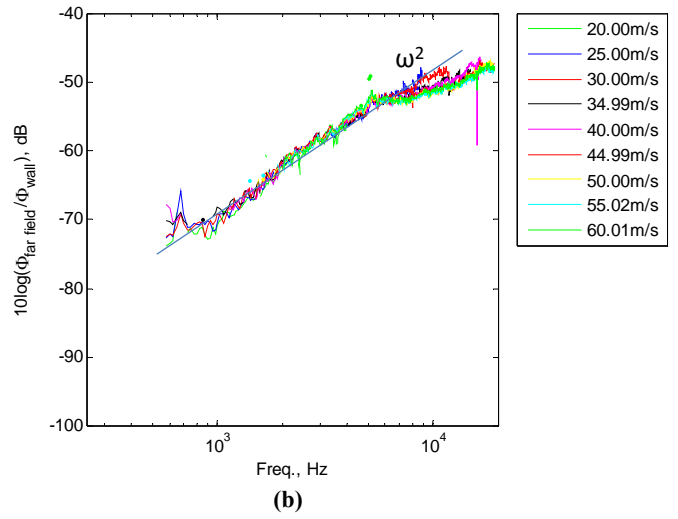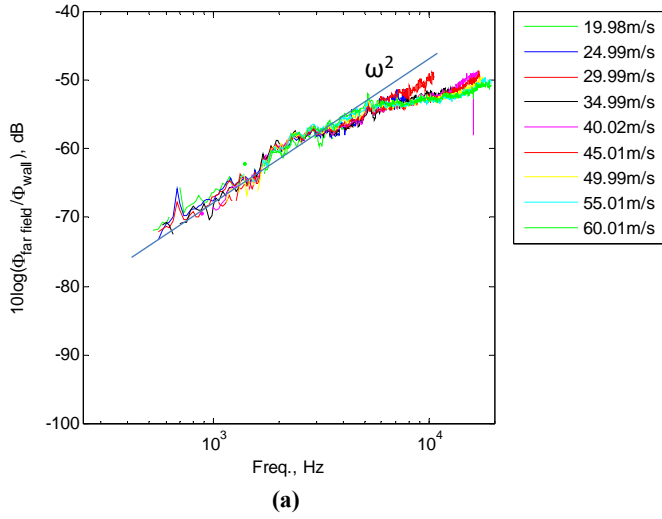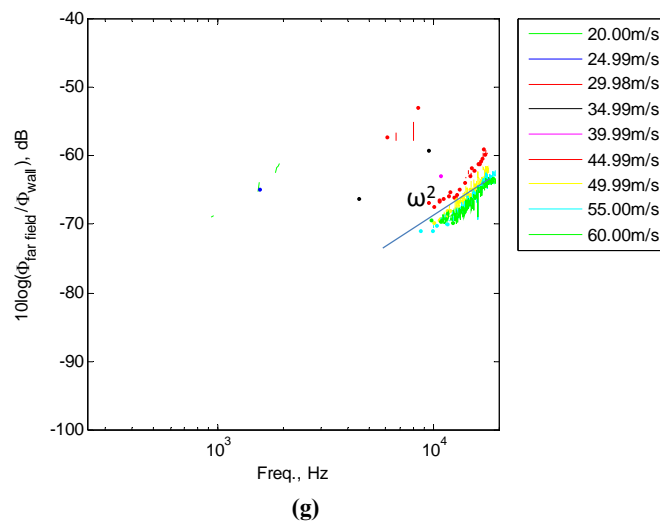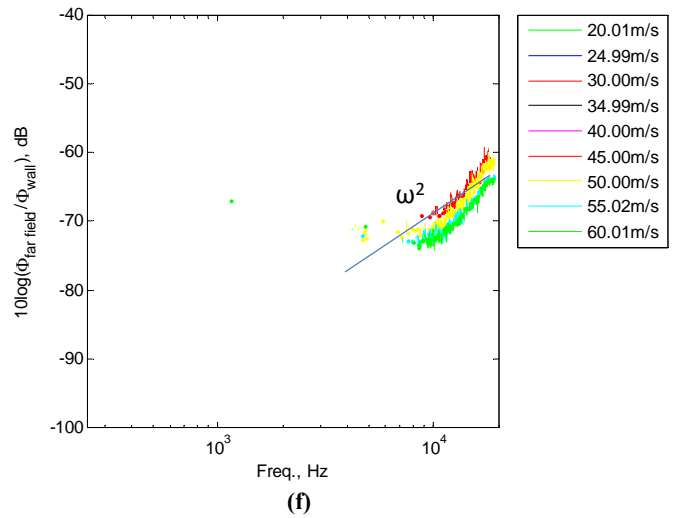

(g)
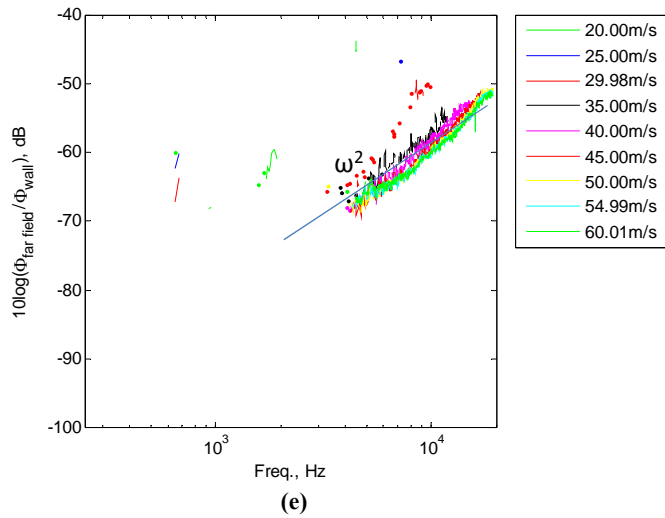
Figure 3.17 Glegg & Devenport (2009) normalization for (a)20Belt, (b)36Belt, (c)60 grit, (d)80 grit, (e)100 grit, (f)150 grit, and (g)180 grit. (Cont'd)

3.4 Roughness Size Normalization of Far Field Sound from Stochastic Surfaces

3.4.1 Inner and Outer Variable Normalizations

To analyze the effect of roughness size and the associated scaling parameter for the radiated roughness noise, the nozzle velocity was held constant while noise from eight different 305x610mm fetches of the stochastic rough surfaces with h^+ varying from 5.5 to 85 were compared. Figure 3.18 shows the far field sound from the eight studied stochastic rough surfaces at a nozzle exit velocity of 60m/s. The sound increases by 24dB at 10kHz from the 180 grit to 20Belt spectra. As the roughness size increases the spectral peak decreases in frequency. The noise radiated from the 60 grit surface peaks at approximately 6kHz while the 20Belt peaks around 3kHz. These trends are consistent with that of Hersh (1983).
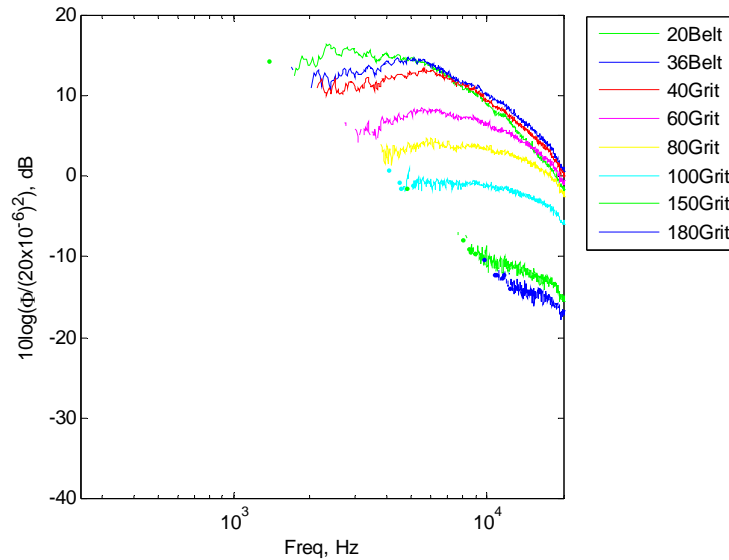
Figure 3.18 Far field noise from 8 stochastic surfaces at a nozzle exit velocity of 60m/s

Applying the same proposed scalings as in Section 3.3.1 and as studied by Grissom (2007), the results show the inability of current inner and outer variable scalings to capture the effect of roughness size. Smooth plate estimations were not needed for these calculations. Measured values for the displacement thickness and friction velocities were used from Grissom *et al.* (2007) and are tabulated in Table 3.1. The 180 grit surface was not studied in Grissom *et al.* (2007) so the value of h^+ was estimated at 5.5 and the displacement thickness was assumed equal to that of the 150 grit surface. The values of u_τ were determined from a momentum balance approach. Uncertainties are estimated at ±8% and ±0.25mm for both u_τ and δ^*, respectively.

Roughness	u_τ,m/s	δ^* ,mm
20Belt	1.4	3.67
36Belt	1.39	3.31
40 Grit	1.4	2.89
60 Grit	1.24	2.41
80 Grit	1.16	2.23
100 Grit	1.12	1.69
150 Grit	1.02	1.65
180 Grit	1.05	1.65

Table 3.2 Profile characteristics for rough surfaces from Grissom *et al.* (2007)

Figure 3.19 (a-b) show the Cole (1980) dipole and quadrupole theories, respectively. The data fail to collapse and have a spread of 25dB for both normalizations. The shortcomings of Cole's (1980) theory are apparent here. The displacement thickness is not a sufficient scaling length. It fails to capture the effect of the roughness size.

Figure 3.19(c) shows Howe's (1988) normalization using the measured RMS roughness heights and friction velocities for each surface. The data does not collapse and produces a range of 15dB between the spectral peaks of the 20Belt and 180 grit surfaces. The frequency collapse also fails to align the spectral peaks. Instead, they shift to lower non-dimensional frequencies as the roughness size decreases.

Glegg *et al.*'s (2007) normalization, shown in Figure 3.18(d) shows a similar result to that of Howe (1988). The data still have a range of 27dB from the 20Belt peak to the 180 grit spectra and the frequency is not collapsed shifting the spectral peak to lower frequencies as the roughness size decreases. Farabee & Geib's (1991) normalization has greater success at scaling the frequency, same as the earlier discussed Cole (1980) scalings, but the results span almost 20dB as shown in Figure 3.18 (e).
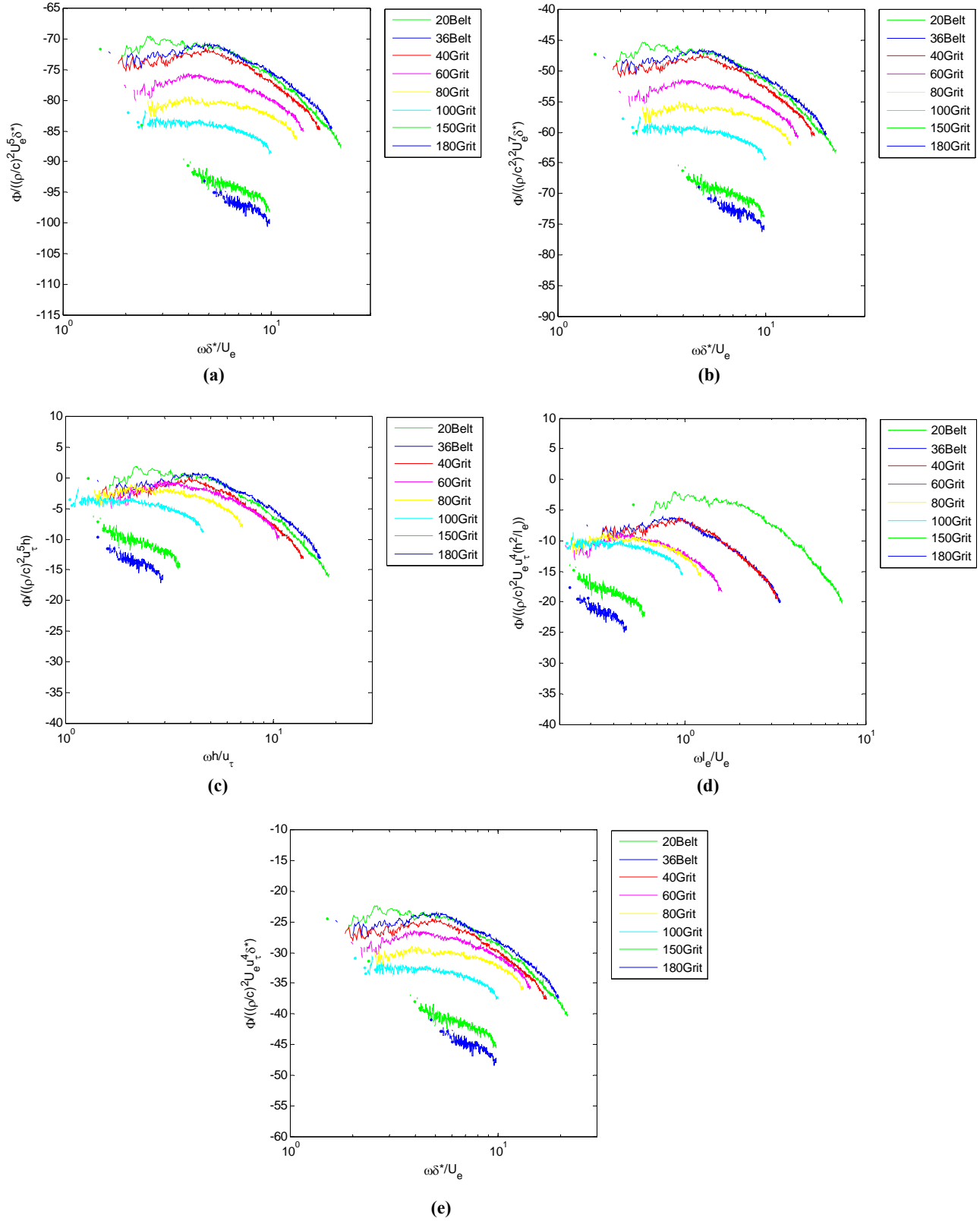
Figure 3.19 Normalized far field noise from varying rough surfaces using (a) Cole (1980) dipole (b) Cole (1980) quadrupole (c) Howe (1988) (d) Glegg *et al*. (2007) and (e) Farabee & Geib (1991) normalizations at a nozzle velocity of 60m/s

The results shown in Figure 3.18 (a-e) are consistent with those of Grissom (2007). The uncertainties in u_τ and δ^* effect the magnitude of the spectral peak collapse by approximately ±0.2dB for the Cole (1980), Howe (1988) and Glegg et al. (2007) scalings and ±0.7dB for the Farabee & Geib (1991) scaling. This uncertainty is insignificant compared to the displayed peak range and does not affect the conclusions.

After comparison of multiple rough wall spectra, it is apparent the spectral shapes produced by the rough surfaces will be unable to collapse completely using the inner and outer variable scalings. These scalings are single valued normalizations applied individually to each spectrum and cannot account for differences in spectral shape. Grissom (2007) concluded similar results and showed that the noise produced by the stochastic roughness, when overlayed on each other, could not fall on a single line. He attributes some change in the spectral shape to Reynolds number effects on the turbulent character of the wall jet flow.

3.4.2 Normalized on Wall Pressure

Continuing from the success displayed in Section 3.3.2 applying the Glegg & Devenport (2009) normalization, Figure 3.20(a) displays the results of normalizing the measured far field from the 8 stochastic surfaces on their respective wall pressure measurements at U_o=60m/s. This normalization ignores the effect of roughness height, essentially assuming h^2=1 for all rough surfaces in Equation 3.5. The rise in far field noise intensity is clearly not just a function of the wall pressure fluctuations. Glegg & Devenport (2009) suggest that the noise is proportional to h^2 for a random discontinuous surface. Figure 3.20(b) applies the full version of Equation 3.5 and collapses the data using the measured mean square height for each surface. The data in low frequencies collapses within 2dB until approximately 5.2kHz. Above this, the data generally fans out in order of grain size except for two of the surfaces, 150 grit and 180 grit which only produce noise at the highest frequencies. Again, the frequency where the deviation begins corresponds with the peak calibration response of the wall pressure microphone suggesting that the pinhole modification could be affecting the measured wall pressure spectra. The spectral fanning in higher frequencies is similar to that shown in Figure 3.17. The low frequency region follows the dipole efficiency factor, ω^2, as expected.

The collapse shown in Figure 3.20 (b) indicates again that the radiated far field noise is a function of the wall pressure spectrum and that the wavenumber spectrum of the surface roughness slope, Γ from Equation 3.4, is a constant proportional to the roughness height squared for these stochastic surfaces. Glegg & Devenport's (2009) normalization works to collapse the sound radiated by these rough surfaces up to 5.2kHz even though, as shown in Section 3.4.1, the surfaces produce spectra with significantly varying shape. This method works because it is not just a single value scaling applied across the entire frequency range for each spectrum. In Glegg & Devenport's (2009) normalization, the wall pressure spectrum changes with velocity and roughness height and the wavenumber filter applies a bias to the wall pressure spectrum to produce the scattered far field sound. These are two independent functions defining the radiated far field sound from a rough surface.
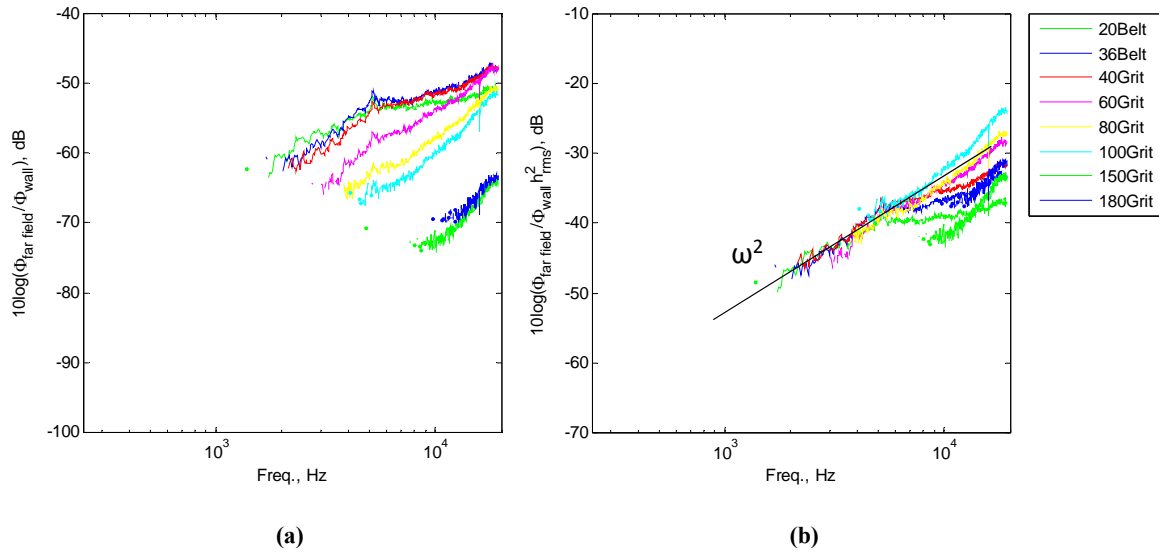
Figure 3.20 Near field normalization of 8 stochastic rough surfaces at U_o=60m/s (a) $h^2 = 1$ (b) $h^2 = h_{rms}^2$

3.5 Deterministic Roughness

3.5.1 Comparison of Spectral Shapes

In addition to the stochastic rough surfaces tested, noise from several deterministic surfaces was studied. Experiments were performed on two hemispherical rough surfaces with 3mm and 1mm elements spaced 16.5mm and 5.5mm apart, respectively, and a 2D rib roughness (LPI-20) 0.28mm tall. The ribs were aligned perpendicular to the flow to generate the most far field sound according to the results of Grissom (2007) which detailed experiments on a similar surface. All deterministic roughness measurements were completed using Microphone Configuration (A). Figure 3.21 shows the subtracted far field noise for the three deterministic rough surfaces and stochastic surfaces of comparable roughness heights at U_o=60m/s.

The effect of the roughness shape on the radiated sound is apparent when comparing the 2D roughness to the 80 grit surface. The 80 grit roughness produces noise at similar levels compared to the LPI-20 lenticular lens, but the two surfaces generate very different spectral shapes. The 2D roughness shows a much more peaked spectrum. This adds further evidence that indicates the previously suggested inner and outer variable scalings would not be able to collapse boundary layer noise from multiple surfaces that have significantly varying wavenumber spectra.

Proposed scattering theories would indicate that a sinusoidal surface would produce a peaked radiated far field because of its narrow wavenumber content. These scattered pressure fluctuations would be dominated by the stronger fluctuations at the convective ridge of the wavenumber-frequency surface pressure spectrum with values associated with the spatial wavenumber of the surface. Glegg & Devenport (2009) indicate that this could be used as an indirect method of measuring the wall pressure spectrum at smaller wavenumbers than previously possible.
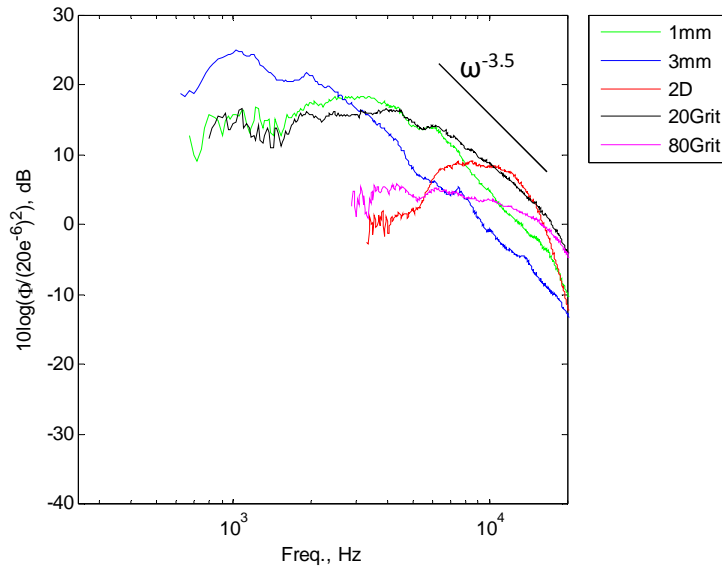
Figure 3.21 Deterministic rough surfaces compared to stochastic roughness of similar size at 60m/s

The 1mm hemispheres' spectral shape is most similar to the 20 grit spectra at low frequency but rolls off much faster as the frequency increases. This could be due to the uniformity of the 1mm roughness elements compared to the sandpaper. The sandpaper roughness does contain many elements roughly 1mm in size but is also composed of smaller elements distributed throughout that could be adding to the high frequency content of its spectra. There was no measured stochastic roughness similar in size to the 3mm hemispherical roughness for comparison, though the general relation of the far field sound with roughness size can still be observed. The spectral peak is roughly 10dB greater than the 1mm hemispherical roughness and the peak occurs at approximately 1kHz compared to 3kHz for the 1mm roughness. Although beginning at a lower frequency, the 3mm spectrum's roll-off is similar in shape to the result of the 1mm hemispherical roughness. The spectral slope at high frequencies for both spectra is approximately -3.5.

3.5.2 Hemispherical Roughness and Normalization

Figure 3.22 and 3.23 show the far field noise and wall pressure spectrum for the two hemispherical surfaces. These measurements were taken using Microphone Configuration (A) explaining the lumps in the wall pressure spectra and far field scalloping. The wall pressure spectrum presented for the deterministic surfaces was taken at x=1505mm. For a nozzle velocity of 60m/s, the 1mm surface had an h^+ of 75 and the 3mm surface had an h^+ of 226 using the Bradshaw & Gee (1960) smooth plate estimation for u_τ. Actual values of h^+ would be slightly larger because of the increased shear from the elements. Due to the larger element size and spacing, the microphone positioned in the 3mm surface had individual elements that dominated the physical surrounding of the microphone. The 1mm surface had a more homogeneous physical surrounding. Figure 2.24 from Section 2.6 shows the microphone locations and relative distances for both hemispherical surfaces. Also note, when using Microphone Configuration (A), the smooth plate far field noise was used as the background noise for the far field subtraction. The step created by the deterministic rough surfaces most likely created measurable far field sound due to the

59

backing thickness of the roughness, 1.2mm for the 1mm surface and 1.6mm for the 3mm surface. These steps were comparable to the 20Belt surface, 1.27mm, which was shown to produce noise as seen in Figure 3.4. Because of the background subtraction method, the step noise will be included with the roughness noise in the subtracted spectra. Focusing on Figure 3.22(a) and Figure 3.23(a), the 1mm roughness shows no obvious spectral irregularity, but the 3mm roughness has some suspect spikes at 7kHz-8kHz and 12kHz-13kHz. It is unknown if these features are due to edge noise. The frequency of their occurrence does not change with velocity and suggests a source unrelated to flow velocity. There was some concern during the measurement of the 3mm hemispherical roughness that the edges of the surface were fluttering.
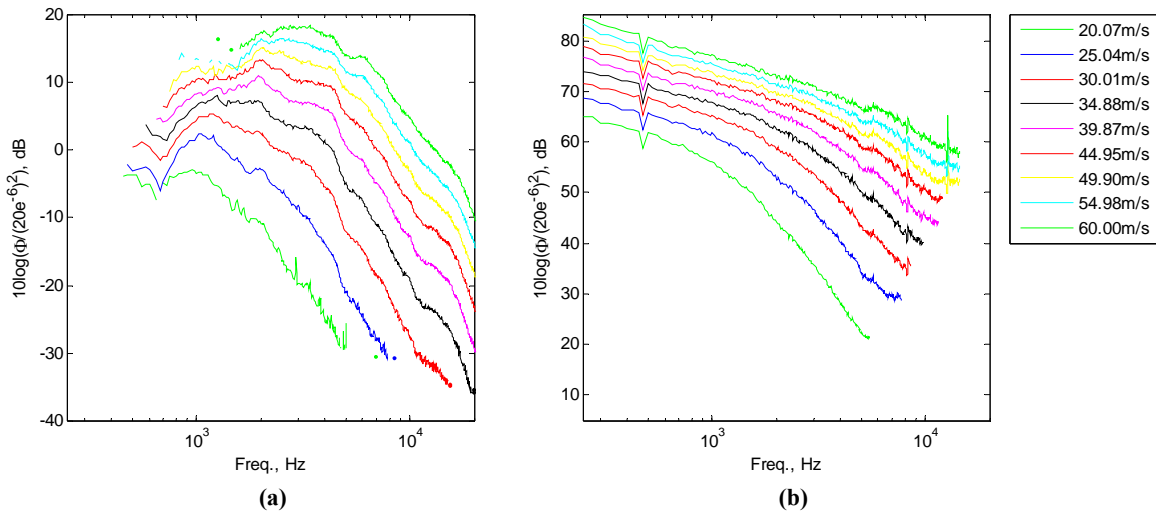

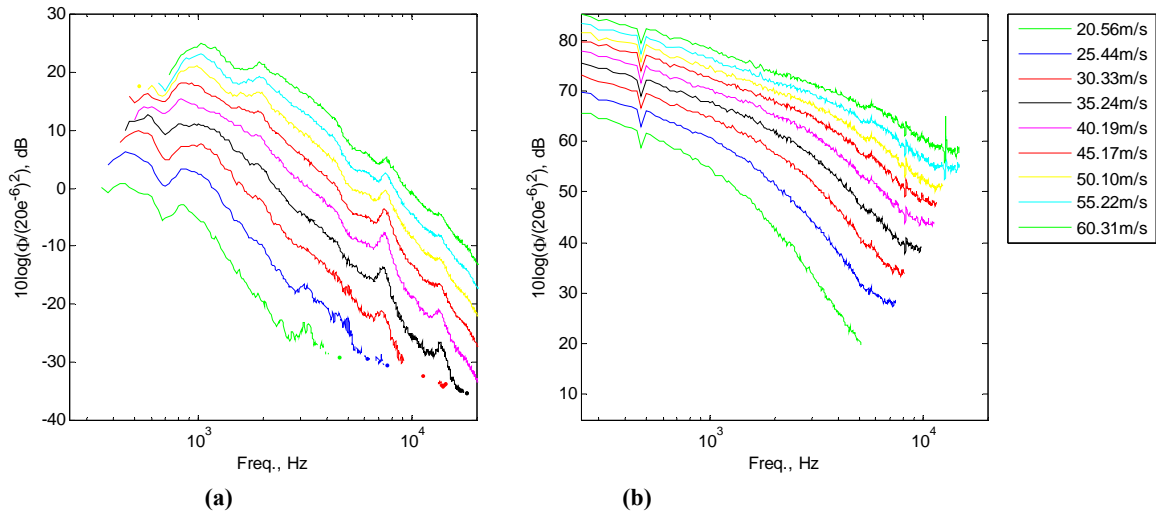**Figure 3.22 (a) Far field noise (b) and wall pressure spectra (x=1505mm) for 1mm hemispherical roughness**

Figure 3.23 (a) Far field noise (b) and wall pressure spectra (x=1505mm) for 3mm hemispherical roughness

Noting the difference in spectral shape as compared to the stochastic surfaces, there is no need to apply the inner and outer variable scalings to the deterministic surfaces. As shown in Grissom (2007), the differences in surfaces wavenumber are unaccounted for in these normalizations. Instead, Glegg & Devenport's (2009) calculated normalization for a randomly rough surface with vertical sides was applied to the results from these deterministic surfaces. Figure 3.24(a) and (b) show the collapse of the 1mm and 3mm hemispherical rough surfaces, respectively. The normalization produces a collapse for the 1mm roughness similar to the stochastic surface but does not collapse the 3mm roughness very well. The 1mm roughness follows the theoretical ω^2 slope but then deviates again with a frequency close to the calibration's spectral peak. The deviation for this surface is different from the previously observed normalizations. The spectra break from the ω^2 slope and fan out in order of velocity. This could be the result of a suspect calibration taken during the measurements of Microphone Configuration (A). Overall, the 1mm roughness is scaled well collapsing as tight as 1dB.

The 3mm roughness collapses well within the suspect region where the high frequency spikes occurred in the far field, but the central frequency range 800-5000Hz expands out to a range of 10dB with the spectra fanning in order of velocity. The spectra's failure to collapse could be due to an inaccurate representation of the integral wall pressure spectrum over the surface. The elements are significant in size and spaced far apart. The wall pressure recorded at one point on the surface may be influenced by its location relative to the nearest element. The derivation of Glegg & Devenport (2009) assumes a homogeneous wall pressure spectrum which is not valid when the elements increase in size relative to the boundary layer and a single point wall pressure spectrum is used to represent a summation of the entire wall pressure spectrum. A single element could be influencing the local measured wall pressure and skew the results.
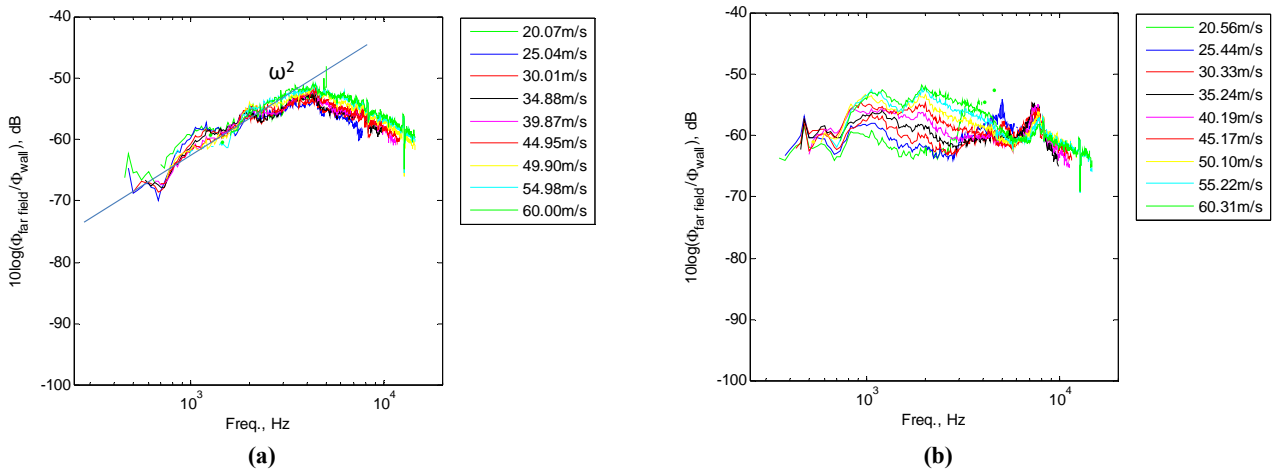

Figure 3.24 Glegg & Devenport (2009) collapse of (a) 1mm hemispherical roughness and (b) 3mm hemispherical roughness

3.5.3 2D Roughness and Normalization

Figure 3.25(a) and (b) show the results for the subtracted far field noise and wall pressure from the 2D lenticular lens surface at all measured velocities. The far field results show very peaked sound levels compared to the results for the stochastic or hemispherical rough surfaces due to the 2D surfaces narrow wavenumber content. The peak far field sound level frequency increases from 4.5kHz to approximately 9kHz and the magnitude increases by 28dB from 25.13 to 60.01m/s.
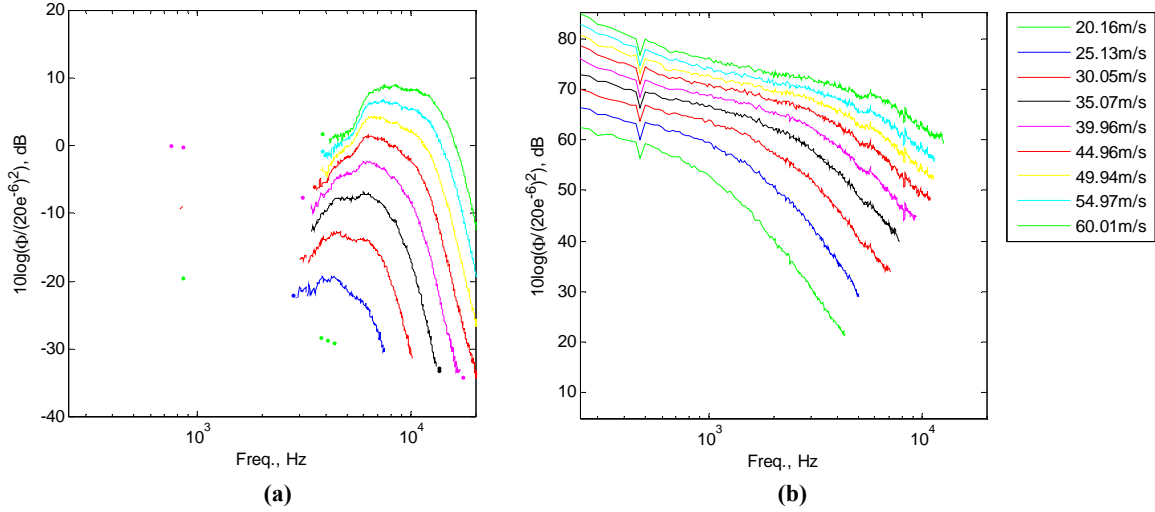

Figure 3.25 Far field noise and wall pressure spectra (x=1505mm) for 2D rib roughness

The wave number filter of a wavy wall is different than that of a stochastic roughness with vertical sides. Glegg & Devenport (2009) provide a solution for their "Unified Theory" computing the wavenumber filter produced by a wavy wall resulting in Equation 3.6.

$$\Phi_{pp}(\boldsymbol{x},\omega) \approx 2\left(\frac{\pi k_o k_w h}{|x|}\left(\frac{x_1}{|x|}\right)\right)^2 \left(\frac{\Sigma}{\pi^2}\right)\sum_{n=1}^{\infty}(na_n)^2\{\Phi_{PP}(nk_w,0,\omega) + \Phi_{PP}(-nk_w,0,\omega)\} \quad \text{Eq. 3.6}$$

where k_w is the wavenumber of the surface. Glegg & Devenport (2009) state that if the surface is sinusoidal or near-sinusoidal that the first term of the summation dominates the radiated far field spectra. Therefore, the radiated far field would be proportional to the wavenumber spectrum at the spatial wavenumber of the surface. That explains the peaked shape of the far field sound produced by the 2D surface. The radiated sound is a measure of the convective ridge which dominates the wavenumber-frequency spectrum. Using Equation 3.6, the magnitude of the far field sound is normalized by first dividing by the wall pressure spectrum as shown in Figure 3.26(a) and then by the acoustic wavenumber and squared roughness height as shown in Figure 3.26(b). This results in a measure of the wavenumber surface pressure spectrum.

This can be used to validate wall pressure spectrum models by backsolving from the measured far field sound for the wavenumber surface pressure spectrum. In Figure 3.26 (a), there is no frequency collapse of the spectra. This is because the frequencies of the wall pressure fluctuations around the convective ridge are increasing with velocity. According to the Corcos (1964) wavenumber spectrum model, the surface pressure spectra should collapse on a Strouhal number defined by $\omega/k_w U_c$ where U_c is

the convection velocity. The frequencies in Figure 3.26 (b) have been non-dimensionalized using U_c=60% as suggested by Blake (1970). The data collapses as predicted up to a nondimensional frequency of 0.7. This indicates that the radiated far field is indeed a measure of the convective ridge of the wall pressure spectrum. The spectra fan out in order of velocity above a Strouhal number of 0.7 with the slowest velocities on top. This is the same fanning result as seen for the spectra in Figure 3.17 (a-g) and again suggests that the spread is a result of the measured wall pressure spectra and measurement technique.
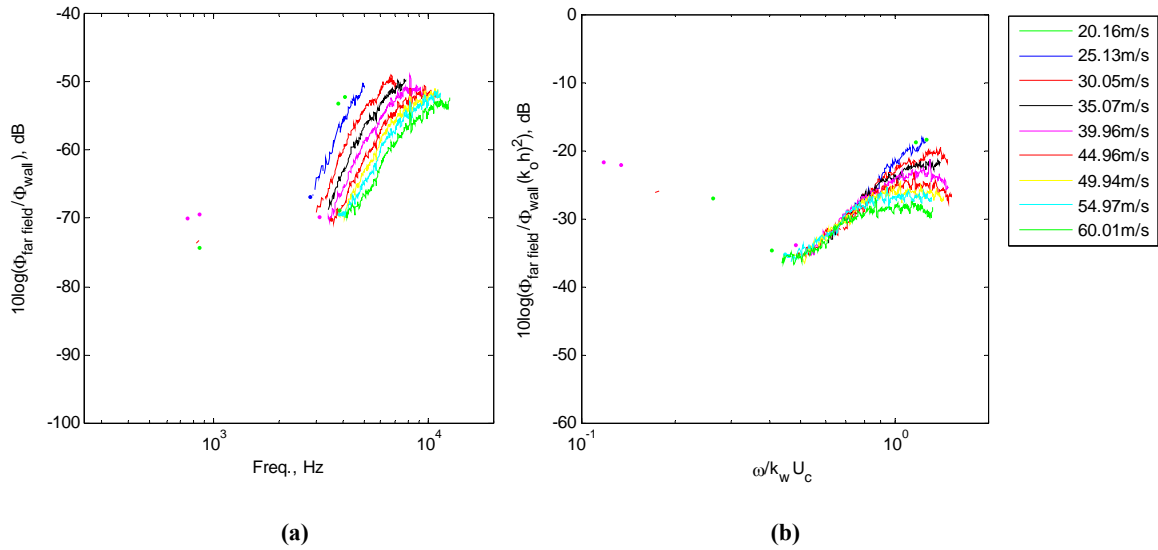

(a) (b)

Figure 3.26 Wavy wall results (a) normalizing the far field by the recorded wall pressure spectrum (b) and using Glegg & Devenport's (2009) full solution for a wavy wall

Chapter 4 Conclusions

       The Virginia Tech Anechoic Wall Jet Facility was used to record roughness noise measured from surfaces that ranged from hydrodynamically smooth to fully rough. Several forms of roughness were studied including stochastic roughness, hemispherical roughness, and a wavy wall surface. Simultaneous far field and surface pressure measurements were recorded to determine the influence of these surfaces on radiated and local pressure fluctuations. Improved methods were developed through experimentation for both far and near field measurement techniques which decreased scalloping and general uncertainty.

       Measured far field spectra reveal that the radiated noise is significantly impacted by the character of the rough surface and the boundary layer flow above it. This dependence was studied in depth by applying several scalings in an attempt to identify the important variables affecting the noise generation. Previously considered inner and outer variable scaling techniques were applied to the measured data as in Grissom (2007) with similar results. The contribution of this study was the analysis of a recent derivation proposed by Glegg & Devenport (2009) that attempts not only to scale the data, but explain the physics of the noise generation. The following are the conclusions of this report.

General Observations

- Roughness noise measurements are approximately 60-70dB below the intensity of the wall pressure fluctuations indicating only a small fraction of the wall pressure is scattered into sound.

- None of the proposed inner and outer variable scalings could collapse the entire considered frequency range independently varying edge velocity or roughness size. This is partially due to the varying spectral shape of the produced far field noise which is a function of both the velocity and surface shape characteristics. These results are consistent with that of Grissom (2007).

- The radiated far field noise is directly proportional to the wall pressure spectrum.

- The resultant normalizations produced by Glegg & Devenport (2009) (excluding the 3mm hemispherical surface) show the noise from all surfaces to obey the ω^2 dipole efficiency factor at frequencies below the spectral peak of the wall pressure microphone calibration. This is the clearest confirmation to date that the roughness noise source is of a dipole nature.

Stochastic Surfaces

- The filter function, Γ, from Glegg & Devenport (2009), which is the wavenumber spectrum of the surface slope, is proportional to the mean square roughness height for the measured stochastic surfaces.

Hemispherical Surfaces

- Noise from 1mm hemispherical roughness elements can be collapsed on measured single point wall pressure spectra using the discontinuous surface formulation of Glegg & Devenport (2009).

- Noise from 3mm hemispherical elements fails to collapse on the measured single point wall pressure spectra. This is most likely due to an inaccurate representation of the integral wall pressure spectrum by a single point measurement. The 3mm elements significantly influence the local wall pressure around them invalidating Glegg & Devenport's (2009) simplified formula that assumed a homogeneous wall pressure spectrum.

Wavy Wall Surface

- The studied wavy wall surface, LPI-20 lenticular lens, produces far field noise consistent with a cut through of the wavenumber-frequency spectrum at the wavenumber of the surface. The far field noise provides an indirect measurement of the intensity of the convective ridge of the wall pressure spectrum because of the surface's near-sinusoidal shape.

- Glegg & Devenport's (2009) simplified normalization for a sinusoidal wall successfully scales the recorded far field noise produced by the LPI-20 lenticular lens.

Appendix

This section contains results from stochastic surfaces recorded using Microphone Configuration (A) whose measurements were not repeated with Microphone Configuration (B). Therefore, these results will display the suspect features discussed in Section 3.1 for both the near and far field. Figure A.1 shows the background subtracted far field sound recorded from the 60Belt, 80Belt, and 220 grit surfaces.
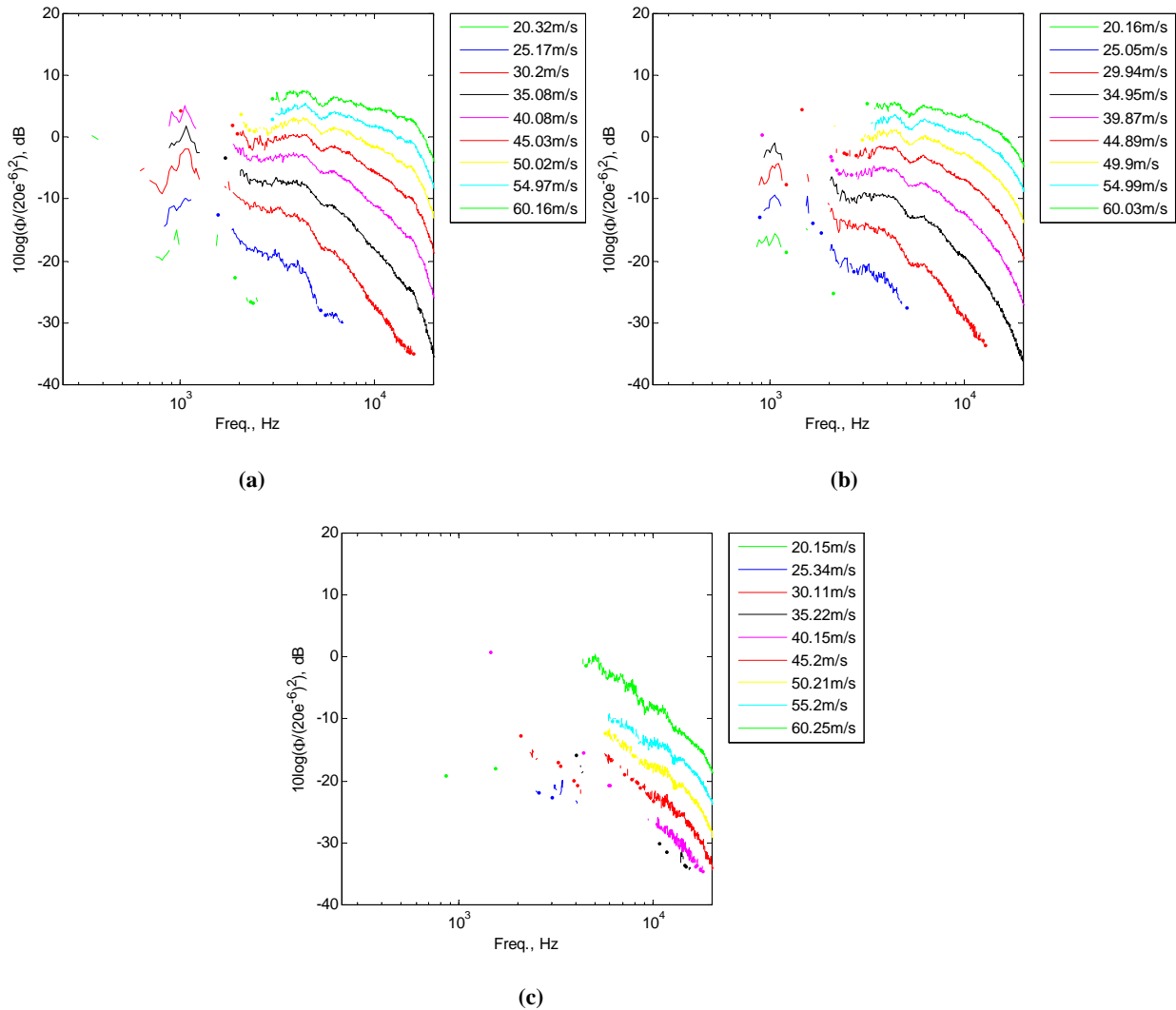

(a)

(b)

(c)

Figure A.1 Far field noise produced by 60Belt, 80Belt, and 220 grit rough surfaces at varying nozzle exit velocities

These spectra produce consistent results with data presented in Section 3.2. The magnitude and frequency of the spectral peaks increase with velocity and the magnitude of the sound reduces with roughness size. Figure A.1 (c) shows a clear increase in sound coming from the 220 grit roughness. This is a remarkable measurement because this surface falls within the hydrodynamically smooth region with $h^+ = 5$ at U_o=60m/s. This is further proof of a scattering mechanism.

Figure A.2 shows the wall pressure spectra recorded at x=1403mm, 146mm inside each fetch of roughness. These data have been filtered at the noise floor of the wall pressure microphone.
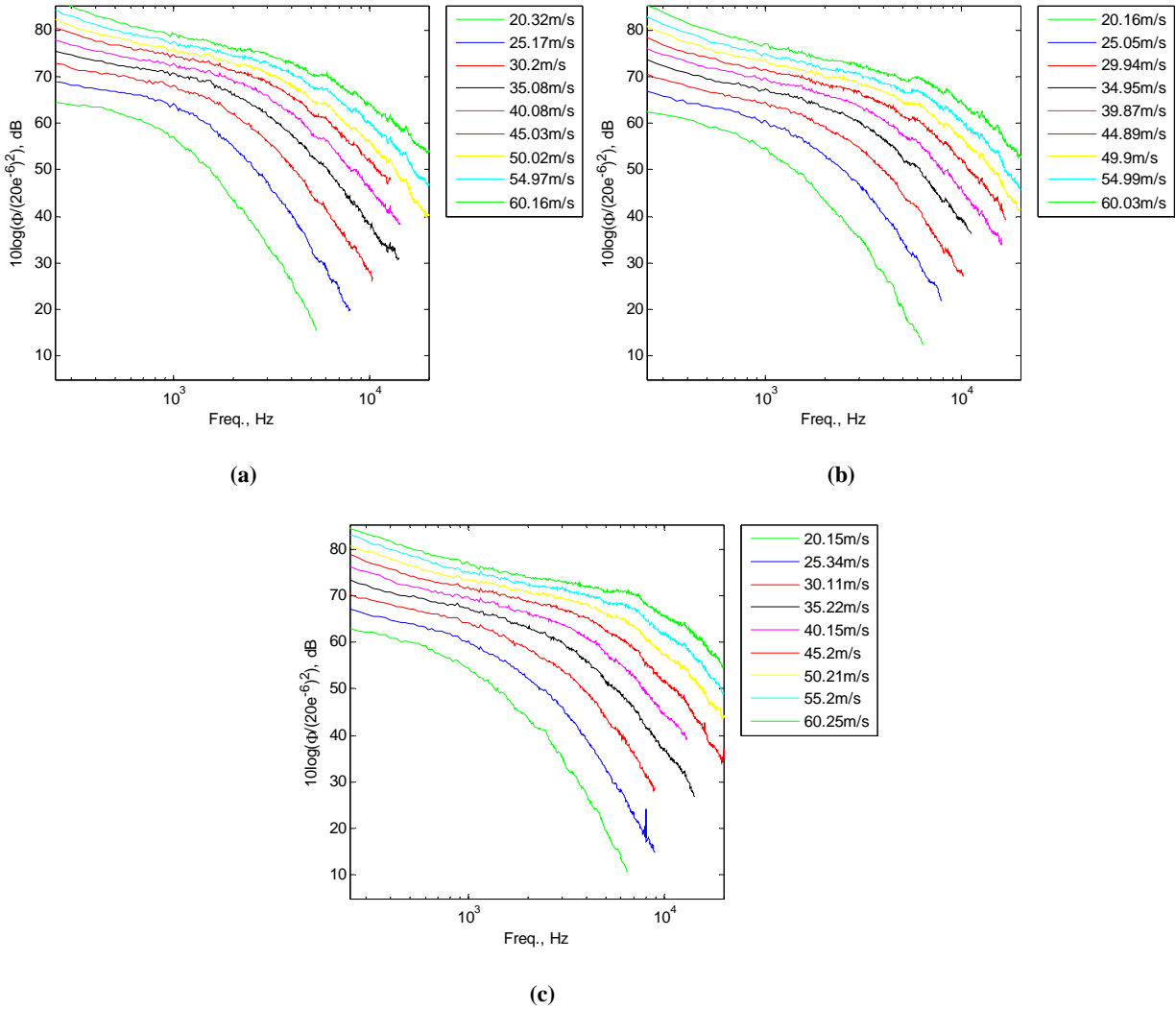

(a)

(b)

(c)

Figure A.2 Wall pressure measurements at x=1403mm for 60Belt, 80Belt, and 220 grit roughness

We can normalize this data using Glegg & Devenport's (2009) solution for a discontinuous surface of random roughness. These results are shown in Figure A.3. The data collapse within 5dB for all surfaces, not near the same level of collapse as shown previously in Section 3.3.2. This is most likely due to the increased uncertainty and questionable measurement techniques of Microphone Configuration (A). The data still seem to follow the ω^2 trajectory suggesting a dipole source.
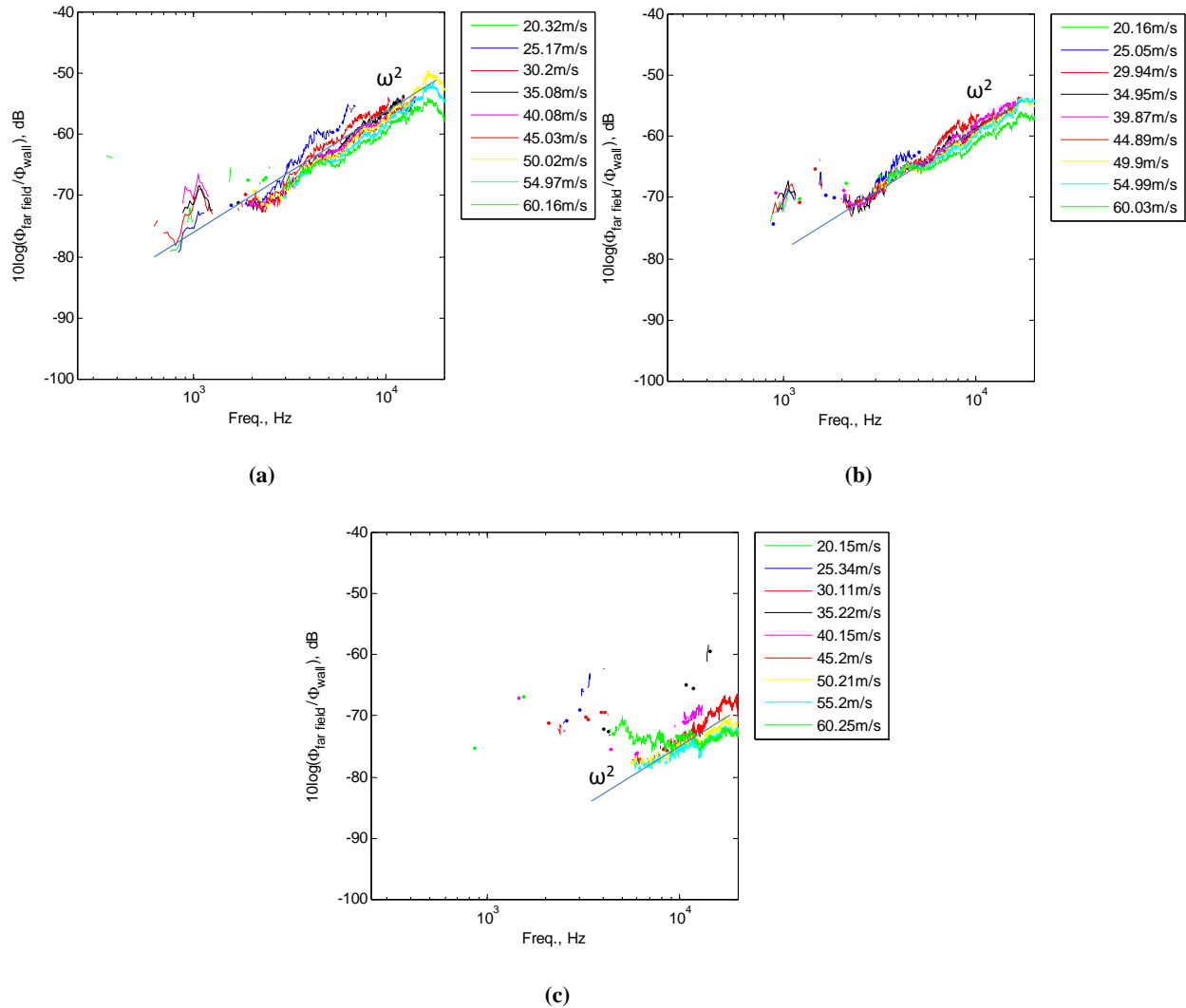

(a)

(b)

(c)

Figure A.3 Glegg & Devenport (2009) normalization for 60Belt, 80Belt, and 220 grit surfaces

References

Aupperle, F.A., and Lambert, R.F., 1970, "Effects of Roughness on Measured Wall Pressure Fluctuations Beneath a Turbulent Boundary Layer", Journal of the Acoustical Society of America, vol. 47, pp. 359 – 370.

Blake, W.K., 1970, "Turbulent Boundary-Layer Wall-Pressure Fluctuations on Smooth and Rough Walls", Journal of Fluid Mechanics, vol. 44, No. 4, pp. 637-660.

Blake, W.K., 1986, "Mechanics of Flow Induced Sound and Vibration", Academic Press, New York.

Chanaud, R.C., 1969, "Experimental Study of Aerodynamic Sound from a Rotating Disk", Journal of the Acoustical Society of America, vol. 45, pp. 392-397.

Chase, D.M., 1980, "Modeling the Wavevector-Frequency Spectrum of Turbulent Boundary Layer Wall Pressure", Journal of Sound and Vibration, vol. 70, No. 1, pp. 29–67.

Chase, D.M., 1987, "The Character of the Turbulent Wall Pressure Spectrum at Subconvective Wavenumbers and a Suggested Comprehensive Model", Journal of Sound and Vibration, vol.112, pp. 125-147.

Cole, L.D., 1980, "Measurements of Sound Generated by Boundary Layer Turbulence over Smooth and Rough Surfaces", DTNSRDC Report SAD-288E-1942.

Corcos, G.M., 1964, "The Structure of the Turbulent Pressure Field in Boundary-Layer Flows", Journal of Fluid Mechanics, vol. 18, No. 3, pp. 353–378.

Curle, N., 1955, "The Influence of Solid Boundaries Upon Aerodynamic Sound", Proc. R. Soc., London, vol. A231, pp. 505-514.

Efimtsov, B.M., 1982, "Characteristics of the Field of Turbulent Wall Pressure Fluctuations at Large Reynolds Numbers", Soviet Physics Acoustics, vol. 28, No. 4, pp. 289–292.

Fang, F.-M., Chen, J.C., and Hong, Y.T., 2001, "Experimental and Analytical Evaluation of Flow in a Square-to-Square Wind Tunnel Contraction", Journal of Wind Engineering and Industrial Aerodynamics, vol. 89, pp. 247-262.

Farabee, T.M. and Geib, F.E., 1991, "Measurements of Boundary Layer Pressure Fluctuations at Low Wavenumbers on Smooth and Rough Walls", Flow Noise Modeling Measurements and Control, ASME NCA-vol. 11, pp. 55-68.

Glegg, S., Devenport, W.J., Grissom, D.L., and Smith, B., 2007, "Rough Wall Boundary Layer Noise: Theoretical Predictions", 13th AIAA/CEAS Aeroacoustics Conference, Rome, Italy, May 21-23, 2007, AIAA-2007-3417.

Glegg, S., and Devenport, W., 2009, "Far-Field Sound from Rough-Wall Boundary Layers", Proc. R. Soc., London, vol. A465, pp. 1717-1734.

Grissom, D.L., 2007, "A Study of Sound Generated by a Turbulent Wall Jet Flow Over Rough Surfaces", Ph.D. dissertation, Aerospace and Ocean Engineering Dept., Virginia Tech, Blacksburg, VA.

Grissom, D., Smith, B., Devenport, W., and Glegg, S., 2006, "Rough-Wall Boundary Layer Noise", 12th AIAA/CEAS Aeroacoustics Conference, Cambridge, Massachusetts, May 8-10, 2006, AIAA 2006-2409.

Grissom, D., Smith, B., Devenport, W. and Glegg, S., 2007, "Rough Wall Boundary Layer Noise: An Experimental Investigation", 13th AIAA/CEAS Aeroacoustics Conference, Rome, Italy, May 21-23, 2007, AIAA-2007-3418.

Hersh, A.S., 1983, "Surface Roughness Generated Flow Noise", 8th AIAA Aeroacoustics Conference, Atlanta, GA, April 11-13, 1983, AIAA-83-0786.

Howe, M., 1984, "On the Generation of Sound by Turbulent Boundary Layer Flow Over a Rough Wall", Proc. R. Soc., vol. A395, pp. 247-263.

Howe, M., 1986, "The Influence of Viscous Surface Stress on the Production of Sound by Turbulent Boundary Layer Flow over a Rough Wall", Journal of Sound and Vibration, vol. 104, pp. 29-39.

Howe, M., 1988, "The Turbulent Boundary Layer Rough Wall Pressure Spectrum at Acoustic and Subconvective Wavenumbers", Proc. R. Soc., vol. A415, pp. 141-161.

Howe, M., 1998, "Acoustics of Fluid-Structure Interactions", Cambridge Univ. Press, Cambridge, England.

Lighthill, M.J., 1952, "On Sound Generated Aerodynamically. Part 1. General Theory", Proc. R. Soc., London, vol. A211, pp. 564-587.

Liu, Y., and Dowling, A., 2007, "Assessment of the Contribution of Surface Roughness to Airframe Noise", AIAA Journal, vol. 45, No. 4, pp. 855-869.

Liu, Y., Dowling, A., and Shin, H.-C., 2008, "Measurement and Simulation of Surface Roughness Noise using Phased Microphone Arrays", Journal of Sound and Vibration, vol. 314, pp. 95-112.

Mish, P.F., 2003, "An Experimental Investigation of Unsteady Surface Pressure on Single and Multiple Airfoils", Ph.D. dissertation, Aerospace and Ocean Engineering Dept., Virginia Tech, Blacksburg, VA.

Narasimha, R., Yegna Narayan, K. and Parthasarathy, S., 1973, "Parametric Analysis of Turbulent Wall Jets in Still Air", Aero. J, pp. 355-359.

Powell, A., 1960, "Aerodynamic Noise and the Plane Boundary", Journal of the Acoustical Society of America, vol. 32, No. 8, pp. 982-990.

Skudrzyk, E., and Haddle, G., 1960, "Noise Production in a Turbulent Boundary Layer by Smooth and Rough Surfaces", Journal of the Acoustical Society of America, vol. 32, pp. 19-34.

Smith, B.S., 2008, "Wall Jet Boundary Layer Flows Over Smooth and Rough Surfaces", Ph.D. dissertation, Aerospace and Ocean Engineering Dept., Virginia Tech, Blacksburg, VA.

Smith, B.S., Alexander, W.N., Devenport, W., Glegg, S., Grissom, D.L., "The Relationship Between Roughness Noise and the Near-Field Pressure Spectrum", 14th AIAA/CEAS Aeroacoustics Conference, Vancouver, B.C., May 5-7, 2008, AIAA-2008-2904.

Smol'yakov, A.V., and Tkachenko, V.M., 1991, "Model of a Field of Pseudosonic Turbulent Wall Pressures and Experimental Data", Soviet Physics Acoustics, vol. 37, No. 6, pp. 627-631.

Wygnanski, I., Katz, Y., and Horev, E., 1992, "On the Applicability of Various Scaling Laws to the Turbulent Wall Jet", J. Fluid Mech., vol. 234, pp. 669-690.

Yang, Q., and Wang, M., 2008, "Computation Study of Boundary-Layer Noise Due to Surface Roughness", 14th AIAA/CEAS Aeroacoustics Conference, Vancouver, B.C., May 5-7, 2008, AIAA-2008-2905.